TU Delft

Delft University of Technology

Document Version
Final published version

Citation (APA)
Cisotto, L. (2018). *Optimisation of Coherent Fourier Scatterometry for Side Wall Angle Estimation of Printed Structures*. [Dissertation (TU Delft), Delft University of Technology]. https://doi.org/10.4233/uuid:acc326db-752b-4dcd-9672-5e208cd6285e

Important note
To cite this publication, please use the final published version (if applicable).
Please check the document version above.

Copyright
In case the licence states “Dutch Copyright Act (Article 25fa)”, this publication was made available Green Open Access via the TU Delft Institutional Repository pursuant to Dutch Copyright Act (Article 25fa, the Taverne amendment). This provision does not affect copyright ownership.
Unless copyright is transferred by contract or statute, it remains with the copyright holder.

Sharing and reuse
Other than for strictly personal use, it is not permitted to download, forward or distribute the text or part of it, without the consent of the author(s) and/or copyright holder(s), unless the work is under an open content license such as Creative Commons.

Takedown policy
Please contact us and provide details if you believe this document breaches copyrights.
We will remove access to the work immediately and investigate your claim.

This work is downloaded from Delft University of Technology.

Optimisation of Coherent Fourier Scatterometry for Side Wall Angle Estimation of Printed Structures

Optimisation of Coherent Fourier Scatterometry for Side Wall Angle Estimation of Printed Structures

Dissertation

for the purpose of obtaining the degree of doctor
at Delft University of Technology,
by the authority of the Rector Magnificus, prof. dr. ir. T.H.J.J. van der Hagen,
Chair of the Board for Doctorates
to be defended publicly on
Monday 29 October 2018 at 12:30 o'clock

by

Luca CISOTTO

Master of Science in Physics,
University of Padova, Padova, Italy,
born in Rovigo, Italy.

This dissertation has been approved by the promotors.

Composition of the doctoral committee:

Rector Magnificus,	chairperson
Prof.dr. H.P. Urbach,	Delft University of Technology, promotor
Dr.ir. S. F. Pereira,	Delft University of Technology, copromotor

Independent members:

Prof.dr.rer.nat. R. Bergmann,	Bremer Institut für angewandte Strahltechnik (BIAS), Germany
Prof.dr. A. P. Mosk,	Utrecht University
Dr. O. El Gawhary,	VSL - Dutch Metrology Institute
Prof.dr. W. M. J. M. Coene,	Delft University of Technology
Prof.dr.ir. P. Kruit,	Delft University of Technology, reserve member

This thesis is part of NanoNextNL, a micro and nanotechnology innovation consortium of the Government of the Netherlands and 130 partners from academia and industry. More information on www.nanonextnl.nl.

Keywords: Scatterometry, Side-wall angle metrology

Printed by: Ipskamp Printing

Front & Back: Beautiful cover art that captures the entire content of this thesis in a single illustration.

Copyright © 2018 by L. Cisotto

ISBN 000-00-0000-000-0

An electronic version of this dissertation is available at
http://repository.tudelft.nl/.

Alla mia ragazza, a mio fratello, a mia mamma, a mio papà
e a tutti i miei amici
perché il loro constante sostegno e aiuto
è stato ciò che mi ha spinto
a tagliare questo traguardo.

Luca Cisotto

Contents

Summary

The electronic industry strives continuously to increase the performance of electronic components by adding new functionality, by making them more energy efficient or by increasing their absolute performance. This last possibility is mainly achieved by a higher density of electrical components. In a photo-lithographic process, this is associated with the ability of printing finer and finer details on a wafer, without impacting the speed and the accuracy of the overall process. In industry, this concept is expressed with a single word: *yield*. The higher the yield, the more profits for the chip producer. One of the often chosen procedures to improve the yield is through a tight control of key quantities related to the chip making process such as dose, focus, overlay and other relevant parameters in order to ensure the creation of a defect free device. In other words, through *metrology*. The root of this word is derived from the ancient Greek and it stands for *the science of measuring*. In the description of a target, it is often convenient to parametrize it with few geometrical quantities that are chosen as representative of dimensions or specific features. In the field of metrology applied to the semiconductor industry, one of the most used test targets are periodic gratings. These objects are usually described in terms of four quantities: height h, middle critical dimension *MidCD*, period (often named pitch) p and the side wall angle *SWA*; this last quantity represents the angle between the edge of a trench and the bottom of a line. Particularly, we focus our efforts on improving the estimation of the side-wall angle. Improving the quality of printed target relying on metrology techniques is the underlying motivation of this dissertation and the ultimate goal behind it.

The accuracy with which the SWA can be measured is much lower compared with what can be achieved for the other three parameters. This issue poses several metrology problems because it delivers false information on the specific machine that is to be tested. More specifically, an uncertainty of a couple of degrees in the estimation of the SWA will lead to wrong edge estimations and might result in choosing a different setting for the lithographic machine, even though it might not be needed. This change will impact other quantities and will change the whole behavior of the device. Hence, it is necessary to estimate this angle as precisely as possible to continue having more reliable electrical components. In this thesis we make an important step towards this direction.

It is important to emphasize that the complexity of the problem is enormous. In fact, both physical and chemical processes are taking place during the target creation, which makes it nearly impossible to have a correct model to predict its shape. It is sometimes possible to monitor the shape of the grating profile after its creation, which would allow us to verify the results obtained by our predictions, but performing such a step is not realistic in a high volume manufacturing environment. Thus, few assumptions had to be considered to make the problem treatable from

an analytical and numerical point of view. The main supposition consists in dealing with a non-periodic structure; more specifically we studied, throughout this thesis, a cliff-like object. Furthermore, we mostly modeled the side wall as a linear slope without considering non-linear effects. The results published in this thesis show that, even under these very basic hypothesis, we can reach a good estimation of the SWA of our test structure.

The findings presented in this thesis have been obtained in the framework of scatterometry, the branch of science in which a-priori knowledge is combined with measurements of the scattered radiation by an object, to estimate specific properties of the object itself. This physical process is the basis of a technique developed in the Optics Group at Delft University of Technology, called Coherent Fourier Scatterometry (CFS): an object is illuminated with a focused laser beam, the scattered far field is collected and detected with a camera. This signal is subsequently compared with numerical simulations in order to reconstruct certain geometrical parameters of the object. The two major novelties of this approach consist in the use of coherent light - in place of the more established and well known Incoherent Fourier Scatterometry (IFS) - along with focused illumination. In this way, one can obtain an increased amount of a-priori knowledge by relying on the phase information as well, which is naturally lost in the case of incoherent systems, and gather more simultaneous information by letting the object interact with a focused beam, thereby probing all the incoming angles, within the numerical aperture of the objective, at once. The basic concept of this technique is presented throughout this dissertation, either by building a concrete CFS optical setup, or simply by considering analytically the interaction of a target and a focused beam, under the assumption of coherent illumination.

In this thesis we also show, in Chapter 2, how CFS can be extended to interferometric CFS (ICFS) and used to determine the scattering matrix of a grating. In this case, the standard CFS setup is integrated with an interferometer so that the entire information about the far field - amplitude, phase and polarisation - is obtained. This extension of CFS can be applied to smaller objects (like subwavelength gratings) where the reconstruction using only amplitude data is difficult. We subsequently focus our attention on the side wall angle estimation problem, and for this purpose we consider a cliff-like object instead of a grating. This choice is taken for a number of reasons. First of all our aim is to have a clear understanding of the side-wall contribution to the radiated far field: estimating this in the presence of a periodic grating is more complicated because each trench might have different SWAs compared to other trenches due to processing effects. Furthermore the left and right side-wall angles of each groove might be different. Secondly, the analytical derivation becomes a little easier when dealing with a cliff. In Chapter 3, we introduce an experimental technique which allows us to expand the input illumination - and therefore the scattered field - into different modes and monitor the ones that are more sensitive to a SWA change. In Chapter 4 we begin the transition from a purely experimental analysis to a completely theoretical framework. The major part of this chapter is dedicated to the theoretical explanation of the signal formation. After having looked into possible detection techniques to improve the side-wall

estimation, we optimize, in Chapter 5, the input illumination to reach the maximum sensitivity to a side-wall angle change. In this case the optimum illumination, both in phase and intensity, is calculated solving a Lagrange multiplier problem. The results show an increased sensitivity up to 150% for very steep angles.

The findings in this dissertation are surely encouraging and promising but it is important to stress that this is just the beginning of the journey. For example, it is interesting to extend the results presented in this dissertation to periodic structures; furthermore, polarisation pupil shape might further increase the sensitivity of the scattered field to the side-wall angle parameter. In this context, a larger numerical aperture than the one used in this thesis should be applied, implying that the problem should be treated with vectorial diffraction theory.

It is important to emphasize once more that boosting the performance of semiconductor metrology has direct impact on the quality of the chip manufacturing process and ultimately on our daily lives.

Samenvatting

In de elektronisch industrie probeert men voortdurend de prestatie van elektronische onderdelen te verbeteren. Componenten worden verbeterd door het toevoegen van functies, het verlagen van hun energieverbruik of het verbeteren van de absolute prestatie. Dit laatste wordt doorgaans bereikt door de dichtheid van de elektronische componenten te verhogen. Hiervoor zijn verbeterde lithografische processen nodig, die in staat zijn met dezelfde snelheid en nauwkeurigheid nog kleinere details op de wafers te printen. De mate waarin dit lukt wordt binnen de lithografische industrie yield (opbrengst) genoemd, en het speelt een grote rol in de winstgevendheid van een chip maker. Een regelmatig gebruikte methode om de yield te verhogen, en zodoende meer defect-vrije chips te kunnen produceren, is het nauwkeurig controleren van productieparameters, zoals bijvoorbeeld de dosis, focus en overlay. Met andere woorden: door het toepassen van metrologie. De etymologische herkomst van metrologie, is het oud-Griekse woord voor de wetenschap van het meten. Het verbeteren van metrologie-technieken om daarmee de kwaliteit van geprinte targets te verbeteren is het onderliggende motief en het uiteindelijke doel van dit proefschrit. We richten ons daarbij met name op het verbeteren van de meting van een bijzonder lastig meetbare grootheid: de zijwandshoek. Een meetobject wordt doorgaans geparametriseerd met een beperkt aantal geometrische grootheden die de dimensies of specifieke eigenschappen van het object omschrijven. Een van de meest gebruikte test objecten voor de metrologie in de halfgeleiderindustrie is de periodieke tralie. Dergelijke meetobjecten worden normaal gesproken beschreven aan de hand van vier parameters: de hoogte h, de middle critical dimension (midden kritische dimensie) MidCD, de periode p en de hoek tussen de rand van een plateau en het dal van een lijn, de zogenaamde side wall angle (zijwandshoek) SWA.

De SWA kan veel nauwkeuriger worden gemeten dan de andere drie parameters. Huidige meettechnieken hebben een onzekerheid van enkele graden, wat kan resulteren in een verkeerde afschatting van de locatie van een rand. Aangezien het testobject wordt gemeten om de werking van de machine te analyseren en bij te sturen, kan dit er toe leiden dat men de instellingen van de lithografische machine onterecht aanpast. Dit beïnvloedt niet alleen de SWA, maar ook de andere parameters van het testobject en algehele werking van de machine. Voor het produceren van steeds betrouwbaardere elektronische componenten, is het daarom van belang de SWA zo nauwkeurig mogelijk te meten. In dit proefschrift wordt een belangrijke stap in die richting gezet.

Het is van belang te benadrukken dat de complexiteit van het probleem enorm groot is. In feite vinden zowel fysische als chemische processen plaats gedurende de vorming van het te meten object, met als gevolg dat onmogelijk over een correct model kan worden beschikt, waarmee de vorm ervan kan worden voorspeld. Soms

is het mogelijk de vorm van het rasterprofiel te bemonsteren, nadat dit gevormd is, hetgeen het ons mogelijk zou maken de resultaten, die zijn verkregen met onze voorspellingen, te verifiëren, maar zo'n stap is niet realistisch in een omgeving waar grote hoeveelheden worden geproduceerd. Daarom moesten enkele aannames worden gedaan om het probleem hanteerbaar te maken vanuit een analytisch en numeriek standpunt. De belangrijkste veronderstelling bestaat hierin dat we te maken hebben met een niet-periodieke structuur; meer in het bijzonder hebben wij voor dit proefschrift klif-achtige objecten bestudeerd. Verder hebben wij de hoek van de zijkant gemodelleerd als een lineaire helling, zonder daarbij niet-lineaire effecten te beschouwen. De resultaten die in dit proefschrift worden gepubliceerd laten zien dat wij zelfs onder deze basishypothese tot een goede schatting kunnen komen van de SWA van onze teststructuur.

De bevindingen, die in dit proefschrift worden gepresenteerd, zijn verkregen binnen het raamwerk van scatterometry, de tak van wetenschap waarbij a-priori kennis wordt gecombineerd met metingen van de door een object verstrooide straling, om zo een schatting te kunnen maken van specifieke eigenschappen van het object zelf. Dit fysische proces vormt de basis van een techniek die is ontwikkeld in de Optische Onderzoeksgroep van de Technische Universiteit Delft, genaamd Coherent Fourier Scatterometry (CFS): een object wordt verlicht door een gefocusseerde laserbundel; het verstrooide verre veld wordt verzameld en gemeten door een camera. Vervolgens wordt dit signaal vergeleken met een numerieke simulatie, teneinde bepaalde geometrische parameters van het object te reconstrueren. De twee belangrijkste noviteiten van deze aanpak bestaan in het gebruik van coherent licht – in plaats van de meer gevestigde en bekende techniek Incoherent Fourier Scatterometry (IFS) – en in de toepassing van gefocusseerde verlichting. Op deze wijze kan meer a-priori kennis worden verkregen, door ook gebruik te maken van fase-informatie, die voor incoherente systemen uiteraard verloren gaat, en door meer simultane informatie te verzamelen via interactie van het object met een gefocusseerde bundel, waardoor alle binnenkomende hoeken, binnen de numerieke apertuur van het objectief, worden onderzocht. Het basisconcept van deze techniek wordt in dit proefschrift gepresenteerd, zowel door de bouw van een concrete optische CFS opstelling, als door simpelweg analytisch de interactie tussen een object en een gefocusseerde bundel te beschouwen, onder de aanname dat de verlichting coherent is.

In dit proefschrift hebben we ook, in Hoofdstuk 2, de experimentele resultaten laten zien waarin we CFS uitbreiden naar Interferometrische CFS (ICFS) en de verstrooiingsmatrix van een rooster bepalen. In dit geval wordt de standaard CFS-opstelling geïntegreerd met een interferometer zodat de volledige informatie van het verre veld wordt verkregen: amplitude, fase en polarisatie. Deze uitbreiding van CFS kan worden toegepast op kleinere objecten (zoals sub-golflengte roosters) waarvoor de reconstructie moeilijk is als alleen amplitudedata gebruikt wordt. In de volgende hoofdstukken besteden aandacht aan het probleem van de zijwandshoek, en hiervoor beschouwen we een klif-achtig object in plaats van een rooster. Deze keuze was gemaakt voor een aantal redenen. Ten eerste was ons doel een goed begrip te krijgen van de bijdrage van de zijwandshoek in het gestraalde verre

veld: dit zou moeilijker zijn als er een periodiek rooster is omdat elk dal een andere zijwandshoek kan hebben wegens effecten die optreden tijdens de fabricage. Bovendien kunnen de linker- en rechterzijwandshoeken van elk dal anders zijn. Ten tweede wordt de analytische afleiding een beetje makkelijker wanneer we een klif beschouwen. In Hoofdstuk 3 introduceren we een experimentele methode die ons toestaat de inputbelichting -en dus het verstrooide veld- te expanderen in verschillende modes, en de modes te monitoren die gevoeliger zijn voor de zijwandshoek. In Hoofdstuk 4 beginnen we de overgang van een zuiver experimentele analyse naar een compleet theoretisch kader. Dit hoofdstuk is grotendeels toegewijd aan een geheel theoretische beschrijving van de signaalvorming met, tegen het eind van het hoofdstuk, een vergelijking met experimentele data. In dit geval laten onze bevindingen zien dat het model nog niet compleet is, en dat meer details in beschouwing genomen moeten worden om een betere match te krijgen met de experimentele data. Nadat we naar de verschillende mogelijke detectiemethodes hebben gekeken om de schatting van de zijwandshoek te verbeteren, optimaliseren we in Hoofdstuk 5 de inputbelichting om de maximale gevoeligheid voor verandering in de zijwandshoek te krijgen. In dit geval voeren we een geheel theoretisch onderzoek uit, waarin we de geoptimaliseerde belichting, zowel in de fase als in de intensiteit, berekenen door een Lagrange-multiplicator probleem op te lossen. De resultaten laten zien dat de gevoeligheid tot 150% verhoogd kan worden voor zeer grote hoeken.

De bevindingen in dit proefschrift zijn zeker bemoedigend en veelbelovend, maar het belangrijk te benadrukken dat dit slechts het begin van de reis is. De resultaten kunnen bijvoorbeeld uitgebreid worden van het zijwandshoekprobleem naar periodieke structuren en polarisatie-pupilvorming. Voor de laatstgenoemde kan een grotere numerieke apertuur gebruikt worden, wat betekent dat het probleem met vectoriële diffractietheorie behandeld moet worden. Dit zal een belangrijke stap zijn om het begrip van het probleem te vergroten en het zal het probleem hopelijk meer toegankelijk maken voor onderzoekers om nieuwe ideeën te genereren over hoe de nauwkeurigheid van de meting van de zijwandshoek verbeterd kan worden. Het verbeteren van de precisie en de nauwkeurigheid van deze meting kan leiden tot het fabriceren van computer-chips met hogere kwaliteit dat ons alledaagse leven kan verbeteren.

1

Introduction

People are capable, at any time in their lives, of doing what they dream of.

Paulo Coelho, The Alchemist

1

The continuous technological process driven by the needs of our society has made photonics - the science and technology of light - and optics more in general, a crucial area of scientific and industrial development. The complexity of the technological challenges we are facing requires a strong interaction between academia, industrial and state partners in order to be competitive in different fields.

These necessities have direct impact on the scientific programs at both an European and national level. As an example, photonics is included in Europe's Key Enabling Technologies (KETs) of the 21st Century [1]. Furthermore, roughly 8% of the Horizon 2020 total funding - € 6.2 billion on a total of nearly € 80 billion - have been allocated to photonics-related projects. At national level, several initiatives and joint research programs have been promoted to boost R&D activities in the field of optics. As an example, the Dutch Optics Center (DOC), a TNO and TU Delft initiative, and NanoNextNL, a large program in nanosciences involving several universities and industrial partners, play an important part in promoting this field of science.

In particular, this PhD project is part of one of the NanoNextNL programs, with main subject *"Nano-inspection for next-generation lithography"*. The goal of this project was to improve current metrology tools based on optical far field light detection to characterize small features on wafers with applications in, for example, the semiconductor industry. In particular, over these four years of research, much attention has been directed to study the interaction of light with periodic and aperiodic structures with, as main goal, the characterization of these structures using the scatterometry principle under coherent light illumination.

In this dissertation we elucidate different experimental and theoretical techniques, with the common goal of achieving the most distinctive signal in the far field, caused by slight changes in the parameters of the structure to be studied. Having sensitive inspection methods is a critical and important point given the continuing size decrease of the features on modern electrical chips.

Despite the undeniable proven success of lithography in the last 50 years, which has allowed the semiconductor industry to follow the pace paved by Moore's law, the continuous miniaturization of electrical components is imposing very complicated challenges to the chip manufacturing companies. Therefore, defects-free devices can only be obtained through an optimized printing process, which entails tuning the lithographic machines using test targets, namely optical gratings with certain known nominal parameters that are retrieved afterwards using metrology tools. These parameters are the grating period, height, middle critical dimension (CD) and side wall angles (SWA). More specifically, we identified the so called side-wall angle as the parameter that is least predicable and controllable by chip manufacturing companies. If we consider a periodic grating as the main test structure over which the lithographic machines are calibrated, the side-wall angle is simply defined as the angle between the substrate and the slope of a groove's edge. A different convention is to define this angle as the angle between the normal to the substrate and a groove's edge, but this definition has not been adopted in this dissertation. Moreover, it follows from either of these definitions that the unit cell of a grating might have two different side-wall angles. The - in principle - straightfor-

ward definition of this quantity hides quite several complications. To begin with, the top and bottom parts of a single groove of a grating usually posses round edges, possibly with different curvatures from one another. The net contributions of these structures to the scattering process is all but simple to quantify. Secondly, the edge itself is unlikely to be a straight line, but is instead characterized by a sort of "wavy" profile which is also impacting the scattered field in a very peculiar form. In this dissertation, we purposefully decided to not consider all these effects. The main reason behind this decision lies on the fact that we believe a more specific project is needed to quantify the contribution of each of them.

In this work we consider - except for Chapter 2 - the paraxial optics approximation, which allows us to solve many problems analytically while being able to describe the main physical effects of the systems we considered.

As we have mentioned, many diverse effects can contribute to the scattered field produced by a periodic grating. These effects surely play a role in the results obtained in Chapter 2 where, as we will see, we solve the full vectorial problem to reconstruct the scattering matrix of an object that can be described geometrically by only few parameters. In this circumstance, the more a priori information is added to the system, the easier it is to solve the inverse problem and find the parameter combination that generates the closest far field distribution to the experimental results. One of the first available option is to employ coherent illumination and exploit the information content carried by the phase of the illuminating beam. Inspired by this simple idea researchers at TU Delft have developed a technique called Coherent Fourier Scatterometry.

1.1. Coherent Fourier Scatterometry

Coherent Fourier Scatterometry, CFS for short, is a technique recently developed at TU Delft by El Gawhary et al. [2] in which a coherent focused field interacts with a periodic object and where the scattered field is analyzed in the Fraunhofer regime. The use of coherent illumination has made this technique quite competitive and even superior to its incoherent counterpart - where incoherent light is used to illuminate the grating - particularly in the case where the period of the grating is such that not only its zeroth order but also the first or higher orders overlap simultaneously in the far field. The strength of CFS lies on the possibility to use the phase difference between the zeroth and other orders of the grating as additional a priori information, which makes the naturally ill-posed reconstruction problem easier to solve, given that more information is present. In this context, the problem is defined to be *ill-posed* because the successful reconstruction of the grating parameters from the far field measurements may, or may not, be unique and stable [3, 4]. Other important advantages associated with this methodology are that it is non-destructive, it does not suffer from the Rayleigh diffraction limit and it is easily integrable in lithographic machines. One drawback of CFS as compared to incoherent Fourier scatterometry (IFS) is that it requires a mechanical scan of the sample, thus making it slower than IFS. Nonetheless, it has been successfully demonstrated in grating reconstruction [5].

The core of this technique is the diffraction phenomenon between a periodic

grating - although extensions to aperiodic structures have been made - and an input field. We usually speak of planar diffraction when the incoming light and the diffracted order lie in one plane; conical diffraction refers instead to the situation in which the diffracted orders lie on the surface of a cone. Let us consider, in the case of planar incidence, a one-dimensional grating, periodic along the x-axis and infinite along the y-axis, of period Λ illuminated by a plane wave of initial amplitude A_i:

$$E(x,z) = A_i \exp\left[i(k_x^i x + k_z^i z)\right] \tag{1.1}$$

where the z-axis corresponds to the optical propagation axis, pointing downwards for positive direction of propagation. Because the grating is periodic in the x direction, we can write its reflection function as:

$$r(x) = \sum_{m=-\infty}^{+\infty} \hat{r}_m \exp i\frac{2\pi m}{\Lambda}x, \tag{1.2}$$

where $\hat{r}_m$'s are the Fourier coefficients of $r(x,y)$. The field above the grating can then be expressed as:

$$U(x,z) = A_o \sum_{m=-\infty}^{+\infty} \exp\left[i\left(k_x^i x + \frac{2\pi m}{\Lambda}\right)x + k_z^m z\right], \tag{1.3}$$

where A_o represents the amplitude of the outgoing waves. We can then conclude that the diffracted waves, defined by the k-vector $k^m = (k_x^m, 0, k_z^m)$, obey the following relationships:

$$k_x^m = k_x^i + \frac{2\pi m}{\Lambda}, \tag{1.4}$$

$$k_z^m = \sqrt{k^2 - (k_x^m)^2} = \sqrt{k^2 - \left(k_x^i + \frac{2\pi m}{\Lambda}\right)^2}. \tag{1.5}$$

From these two relations we can infer that not all the diffracted orders are propagating but some of them are evanescent. Furthermore, the number of propagating orders depends on the incoming wavelength and the period of the grating.

This technique, along with the physical model upon which it is built, is the key element to solve what is usually called the *forward problem*. The term emphasizes the fact that we are computing the interaction of an input beam and an object illuminated by it, to obtain the scattered field; therefore, we have to numerically solve the Maxwell equations. When the structure we are dealing with is periodic in one or two dimensions[1], the Rigorous Coupled Wave Analysis algorithm is certainly one of the most used and known.

[1] For completeness, the algorithm, with some modifications, can also be used for aperiodic objects. See for instance [6, 7].

1.2. The Rigorous Coupled Wave Analysis (RCWA) algorithm

The importance of having efficient and accurate numerical tools for the evaluation of Maxwell equations has grown exponentially over the last decades. Rigorous Coupled Wave Analysis, often abbreviated as RCWA or Fourier Modal Method [8, 9], has surely become a popular choice due to the simplicity of its implementation, as well as its accuracy and speed. The basic RCWA algorithm is built upon periodic boundary conditions and Flouquet's theorem for gratings. This theorem converts the infinite physical domain into repetition of infinite number of finite domains each spanning the size of the periodicity of the grating. Subsequently, the original grating profile is split into layers of rectangular stack. The duty cycle of each layer is different from the adjacent ones, but they are all characterized by the same period, such that the initial geometrical structure is properly mapped and represented. This step is important to simplify the treatment of the problem into an electromagnetic waves propagation through a finite number of flat layers, which can be solved utilizing the continuity of tangential fields, as it is shown in Fig. 1.1.

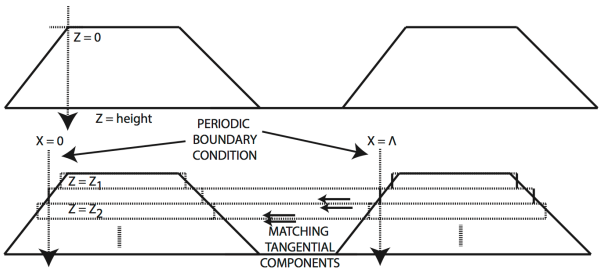

Figure 1.1: In the RCWA method, the original grating is sliced into layers containing a rectangular grating. The electromagnetic problem is solved into each layer. Figure from [10].

Maxwell equations are solved after the Fourier expansion of the periodic permittivity ϵ, or its inverse. The number of terms retained in this expansion affects directly the accuracy of the algorithm. Another important concept that greatly influences the final results is the accuracy with which the staircase approximation represents the structure to be modeled. The routine used for the numerical calculations presented in Chapter 3 is a modified version of the Fourier Modal Method described in [11]. The version of the algorithm we use has been modified to treat the interaction, in reflection, of a grating with a coherent focused field; this field is expanded into plane waves and we solve the diffraction problem for each of these waves, within the numerical aperture (NA) of the system in use. The algorithm allows us to distinguish between different polarization states for the input and output beam.

As mentioned before, the results obtained with the RCWA simulations can be used to verify the outcome of the experimental results obtained, for instance, through a Coherent Fourier Scatterometry setup. In short, we are trying to solve

the *inverse problem*. In this configuration, starting from an experimental far field distribution we try, by using numerical tools, to find the geometrical parameters of the object that generated that particular distribution. This can be done by including the RCWA kernel in a optimization algorithm. The sample under study is, in addition, characterized with standard metrology tools (AFM, SEM), and the results are compared to what has been obtained numerically. We have seen that the confidence interval of this comparison can be greatly improved if the experimental beam used to illuminate the object is used as input for the RCWA algorithm. Because CFS uses a coherent illumination, this implies that amplitude and phase need to be determined. Hence, the use of a Shack-Hartmann wavefront sensor, which measured phase and intensity of a light beam, is important to improve the accuracy of the reconstruction problem.

1.3. Shack-Hartmann wavefront sensor

The previously described RCWA algorithm can greatly benefit from the accurate knowledge of the incident field on the grating. The idea is that, by using the experimentally measured field that is interacting with the sample as input field for the algorithm, the matching between experiment and numerical simulation will improve. The amplitude and phase distribution of the input field can be measured with a Shack-Hartmann wavefront sensor. In this sensor, the incident wavefront is divided into many sub-domains through a 2D array of micro-lenses and focus on a CCD detector. In case of a perfectly collimated beam, each lens element will focus part of the incoming wavefront in a well defined position of the sensor, corresponding to the center of its specific sub-domain. A partially aberrated wavefront will instead results in misplaced foci. The software evaluates the local slope by computing the local derivative obtained from the x and y displacement. This allows to quantify the aberration carried by the input wavefront, which are usually expressed in Zernike polynomials. The resolution of the reconstructed wavefront depends on the size and the focal length of the micro-lenses. We use a Shack-Hartmann sensor provided by Optocraft GmbH with micro-lenses of $150\,\mu m$ diameter and $4.62\,\mu m$ focal length. The CCD sensor on which the micro-lenses focus is made of 1600×1200 square pixels, each of them characterized by a $7.5\,\mu m$ width. An example of a Shack-Hartmann sensor is given in Fig. 1.2

1.4. Goal and outline of the thesis

The main goal of this work, as briefly explained earlier in this chapter, is to provide tools to improve the side-wall angle estimation of aperiodic structures. It is worth mentioning that this does not necessarily imply that the methods we discuss in this dissertation should provide more accurate results. In fact, during these four years of research we always considered the industrial aspects of the problem we aimed at solving. This means that a method which delivers similar results compared to an existing tool, in a faster and/or cheaper way represents a good alternative. Hence different approaches, theoretical and experimental, have been explored to address the problem of finding a better side-wall angle determination. In Chapter 2 we

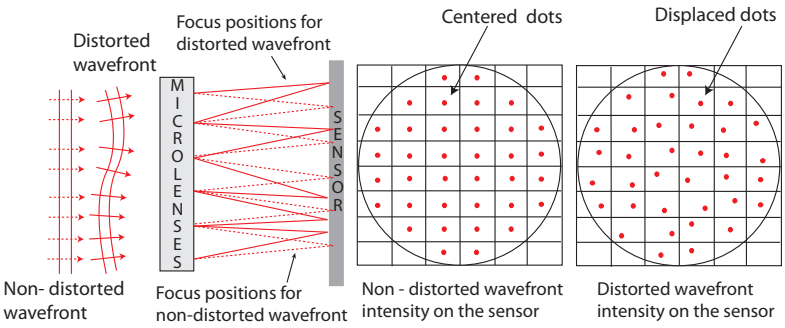

Figure 1.2: Sketch of the measurement principle of a Shack-Hartmann wavefront sensor. Both the case of a non-aberrated and aberrated wavefront are depicted. Figure from [12]

show that, by using interferometric Coherent Fourier scatterometry, it is possible to fully reconstruct the scattering matrix of an object under investigation. In this case we used a periodic grating as test structure, but we would like to emphasize that our findings are generally valid for any target. The knowledge of the phase of the far field, together with its amplitude, improves the object reconstruction, in particular when the grating period is so small that no diffraction orders reach the far field [13]. Chapter 3 is dedicated to the introduction of a detection technique called *Spiral mode projection*; this method is quite advantageous and promising because it can separate the contribution of different geometrical shape parameters (for instance height and side-wall angle) through which we describe the structure under investigation. After a theoretical description of this technique, we prove its validity with experimental results. In Chapter 4 we describe analytically the interaction of a focused field generated by a cylindrical lens with a cliff- and ridge-like object. The scattered far field is measured with a CCD camera, and the difference of the intensity measured in the left and right halves is computed; this type of detection is called split detector configuration. Chapter 5 aims at improving the side-wall angle detection from another perspective: instead of trying to improve the detection branch of our system, we engineer the input field interacting with the target such that the sensitivity to a small side-angle change is maximum. Finally, Chapter 6 summarizes the main findings presented in this dissertation and envisions possible future research developments and projects.

References

[1] *Horizon 2020, the EU framework programme for research and innovation,* https://ec.europa.eu/programmes/horizon2020/en/h2020-section/photonics.

[2] O. el Gawhary et al., *Performance analysis of coherent fourier scatterometry,* Appl. Phys. B **105**, 775 (2011).

[3] H. P. Baltes, *Inverse source problems in optics, Volume 9 of Topics in Current*

Physics, (Springer-Verlag, Berlin; New York, 1978).

[4] J. Lindberg, *Mathematical concepts of optical superresolution,* Journal of Optics **14**, 083001 (2012).

[5] N. Kumar, P. Petrik, G. K. P. Ramanandan, O. E. Gawhary, S. Roy, S. F. Pereira, W. M. J. Coene, and H. P. Urbach, *Reconstruction of sub-wavelength features and nano-positioning of gratings using coherent fourier scatterometry,* Opt. Express **22**, 24678 (2014).

[6] P. Lalanne and E. Silberstein, *Fourier-modal methods applied to waveguide computational problems,* Opt. Lett. **25**, 1092 (2000).

[7] M. Pisarenco, J. Maubach, I. Setija, and R. Mattheij, *Aperiodic fourier modal method in contrast-field formulation for simulation of scattering from finite structures,* J. Opt. Soc. Am. A **27**, 2423 (2010).

[8] M. G. Moharam, T. K. Gaylord, D. A. Pommet, and E. B. Grann, *Stable implementation of the rigorous coupled-wave analysis for surface-relief gratings: enhanced transmittance matrix approach,* J. Opt. Soc. Am. A **12**, 1077 (1995).

[9] L. Li, *Use of fourier series in the analysis of discontinuous periodic structures,* J. Opt. Soc. Am. A **13**, 1870 (1996).

[10] S. Roy, *Sub-wavelength metrology using Coherent Fourier Scatterometry*, Ph.D. thesis, Delft University of Technology (2016).

[11] M. van Kraaij and J. Maubauch, *A more efficient rigorous coupled-wave analysis algorithm,* Prog. in Industrial Mathematics at ECMI 2004 .

[12] N. Kumar, *Coherent Fourier Scatterometry*, Ph.D. thesis, Delft University of Technology (2014).

[13] S. Roy, N. Kumar, S. F. Pereira, and H. P. Urbach, *Interferometric coherent fourier scatterometry: a method for obtaining high sensitivity in the optical inverse-grating problem,* Journal of Optics **15**, 075707 (2013).

2

Interferometric coherent Fourier scatterometry

Study without desire spoils the memory,
and it retains nothing that it takes in.

Leonardo da Vinci

This chapter focuses on the determination of the full scattering matrix of a scatterer. Particularly, given an arbitrary numerical aperture, we use focused beam coherent Fourier scatterometry to study its scattering processes. This technique allows us to obtain the far field intensities of all scattered angles, within the numerical aperture of the optical system, in one shot. The corresponding phases of the field have been obtained with an interferometric configuration. With this method it is possible to retrieve the maximum available information about the scatterer from scattered far field data contained in the given numerical aperture of the system.

Parts of this chapter have been published in Applied Optics **55**, 4408 (2016) [1].

2.1. Introduction

In angular resolved scatterometry, given a certain illumination (for example: incident amplitude, phase, polarization) and optical system (for example: incident wavelength, numerical aperture), the set of all elements of the scattering matrix at all angles that can be detected by the system contains the maximum information about the scatterer.

In this chapter we investigate and demonstrate the limit of optical scatterometry by determining the polarization-resolved amplitude and phase of the scattered field using coherent visible illumination. The maximum information content is relevant not only for the basic understanding of diffraction problems in optics, but is also crucial for several applications in the semiconductor industry. Important examples being chip fabrication metrology, surface inspection and defect detection.

Moreover, in optical lithography, along with the ability of printing sub-wavelength structures, a stringent quality control of the lithographic process is often required. Usually, periodic structures, namely gratings, are used as metrology targets. Slight variations in dose, exposure or environmental conditions such as temperature, humidity and pressure can lead to deviations of the ideal grating shape. Measurement of the grating profiles can be done in principle with scanning electron microscopes and/or atomic force microscopes, but optical scatterometry is the de-facto preferred method because it is noninvasive and fast.

In optical scatterometry, the retrieval of the shape parameters of the grating is done by matching the experimentally measured far-field scattered intensity distribution with the expected distribution that is calculated by rigorous computations, using for example the Rigorous Coupled-Wave Analysis (RCWA) method [2, 3]. To determine the ultimate resolution, one should gather the maximum amount of information about the scattering matrix. There are many variants of optical scatterometry techniques such as single incidence angle reflectometry, 2-Θ scatterometry, spectroscopic ellipsometry, Fourier scatterometry, interferometric Fourier scatterometry, and in recent years, coherent Fourier scatterometry (CFS) [4–14]. In particular, the latter can be made very fast since a focused coherent beam is used, and the scattering information at many angles is captured in one shot. Furthermore, when the period of the structure is such that diffracted orders overlap and the focused spot is scanned, the phase differences between these orders in CFS make this technique more sensitive towards profile changes than incoherent Fourier scatterometry [15]. Nonetheless diffracted orders only overlap when the period is large enough compared to the given numerical aperture (NA) of the focusing lens and the illumination wavelength used. This implies that the advantage of CFS over incoherent scatterometry methods is limited to gratings of a certain minimum period. To overcome this limitation, Sarathi et al. have recently proposed [16] an interferometric version of CFS, by which not only the amplitude but also the phase of the scattering matrix elements is determined and hence an higher sensitivity towards profile changes is achieved for arbitrary period. In interferometric CFS (ICFS), the polarization-resolved scattered field can be retrieved not only for scattering angles where orders overlap but for any scattering angle. ICFS utilizes a reference wave that interferes with the far field generated by CFS to capture the phase information

present in the zeroth order and, if they exist, in the overlapping orders. In the latter case the difference in phase between the overlapping orders is retrieved by scanning, as it is done for non interferometric CFS. Furthermore, by measuring all possible orthogonal incident and scattered polarizations, one can recover the entire complex scattering matrix, i.e., all information that can be obtained within the given numerical aperture of the system. It is also important to notice that we use the same lens to focus the incident wave into a spot and to project the scattered field onto the CCD.

In this chapter we present the determination of the full scattering matrix using ICFS. In particular, in Section 2.2 we summarize the most important aspects of the theory. In Section 2.3 we describe the experimental details, with emphasis on the optical set-up and the data acquisition. In Section 2.4 we discuss the comparison with simulations and Section 2.5 contains the conclusions.

2.2. Theory

Let us begin by considering the scattering problem of a one dimensional grating. We choose a coordinate system (x, y, z) as shown in Fig. 2.1 with the z-axis coinciding with the optical axis of the focusing system. The permittivity is a periodic function of x and invariant along y. It is conventional to set $z = 0$ at the top of the grating and to choose z positive in the direction of incidence (see Fig. 2.1). The incident field is denoted as $\mathbf{E}^i$, and the reflected field from the grating as $\mathbf{E}^r$. Considering a grating of thickness d, then we can express the electric fields as: $\mathbf{E}^i + \mathbf{E}^r$ when $z < 0$.

With Rayleigh's method [17–19], the total field in the grating region can, for example, be computed with the Rigorous Coupled Wave Analysis (RCWA) [2, 20, 21]. The reflected field is then obtained by subtracting the incident field from the total field. In the half space $z < 0$ the reflected field is expanded into a sum of plane waves as follows:

$$\mathbf{E}^r = \sum_m \left[E^r_{ms}\mathbf{s} + E^r_{mp}\mathbf{p}\right] \exp[i(k^r_{mx}x + k^r_{my}y - k^r_{mz}z)], z < 0 \tag{2.1}$$

where $\mathbf{k}^r_m = (k^r_{mx}, k^r_{my}, k^r_{mz})$ is the reflected wave vector. $\mathbf{s}$ and $\mathbf{p}$ respectively denote the s- and p-polarisation states, i.e. the states for which the electric field is perpendicular and parallel, respectively, to the plane of incidence. $\mathbf{k}^r_m$ is related to incident wave vector $\mathbf{k}^i$ by:

$$k^r_{mx} = k^i_x + j\frac{2\pi}{\Lambda}, \quad k^r_{my} = k^i_y, \quad k^r_{mz} = -\sqrt{(k^i)^2 - (k^r_{mx})^2 - (k^r_{my})^2} \tag{2.2}$$

Where Λ is the grating period. It is helpful to express the grating reflection in a matrix form $\mathbf{E}^r_m = \mathbf{R}_m(\mathbf{k}^i)\mathbf{E}^i_j$, with:

$$\mathbf{R}_m = \begin{pmatrix} r_{mss}e^{i\phi_{mss}} & r_{msp}e^{i\phi_{msp}} \\ r_{mps}e^{i\phi_{mps}} & r_{mpp}e^{i\phi_{mpp}} \end{pmatrix} \tag{2.3}$$

where, $\tilde{r}_{msp} = r_{msp}e^{i\phi_{msp}}$ denotes the complex amplitude of the s-polarized component of the m-th reflected order due to an incident wave with wave vector $\mathbf{k}^i$ and

polarized parallel to the p direction. Note that when $k_y^i = 0$, i.e. when the incident plane wave is in the plane perpendicular to the grating structure, the matrix R_m is diagonal because in that case s- and p-polarisations are uncoupled. The matrix $\mathbf{R}_m$ contains the complete set of reflection coefficients of the grating. In the inverse diffraction problem of grating shape reconstruction [5], it is of extreme importance to determine them as precisely as possible. Because of the ill-posedness of the inverse diffraction problem [22], a fast and stable solution depends heavily on the accurate measurement of these coefficients. Any intensity-based technique can at best reveal the phase difference between different elements.

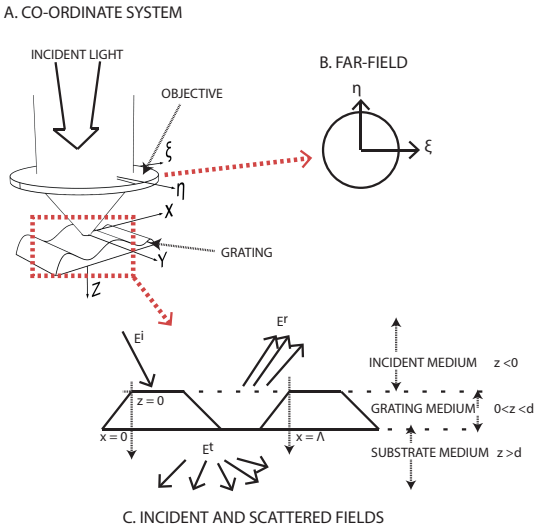

Figure 2.1: A schematic diagram of our approach to the problem of one shot scattering matrix determination for a large number of incident angles. **A.** The $x - y - z$ coordinate system is attached to the sample, with the $z = 0$ plane chosen at the interface between the grating and the incident medium, which is also the geometric focus plane of the objective. **B.** The far-field maps of the complex amplitude of the field is projected on the CCD in the exit pupil of the objective where the coordinate system $(\xi - \eta)$ is chosen such that ξ and η are parallel to the x- and y-direction, respectively. **C.** The interface between the half space $z < 0$ and the grating and the interface between the grating and the substrate $z > d$ are indicated by the dotted lines. Figure from [1].

By combining coherent Fourier scatterometry with temporal phase-shifting interferometry, we show that it is possible to determine the complex reflection coefficients for many angles of incidence, in one shot. The basic idea is to use a microscope objective to focus the incident beam onto the scattering sample, which, in our case, is a one dimensional grating similar to what is represented in part C of Fig. 2.1. In part B of the same figure, the far field co-ordinates $(\xi - \eta)$ are known. They are defined by:

$$\begin{aligned} \xi &= \frac{k_x^r}{k^i} \\ \eta &= \frac{k_y^r}{k^i}. \end{aligned} \tag{2.4}$$

The maximum angle which can be detected is limited by the numerical aperture (NA) of the objective ($\sqrt{\xi^2+\eta^2} \leq \text{NA}$). We remark that Eq. (2.4) implies that ξ and η are parallel to the x- and y-direction, respectively.

In practice, because of the presence of the objective, there are some additional geometric transformations to consider. If the objective is perfectly isotropic, it does not create any additional phase difference between the s- and p-polarized components. In that case, the incident and reflected field are related through $\mathcal{R}'_m$ instead of $\mathbf{R}_m$, where:

$$\mathcal{R}'_m = f\Omega\mathbf{R}_m\Omega^{-1}. \tag{2.5}$$

Where f is a factor for energy conservation [16, 23] and Ω is the rotation of the electric field introduced by the objective and is define as:

$$\Omega = \begin{pmatrix} -\sin\phi & \cos\phi \\ -\cos\phi & -\sin\phi \end{pmatrix} \qquad \text{with:} \quad \phi = \tan^{-1}(\eta/\xi).$$

However, except $\mathbf{R}_m$, all the other factors in Eq. (2.5) are merely geometric and do not contain any information about the object. $\mathcal{R}'_m$ maps the incident pupil (before the objective) to the outgoing pupil (after the objective) directly and therefor can be expressed in terms of the $(\xi-\eta)$ system. Thus, from now on, we express the incident and outgoing fields in the $(\xi-\eta)$ system as well, which respectively denotes the field right before being incident on the objective and the field right after passing through the objective.

In the experimental results that we are going to present, the incident state of polarization is known and the incident field is measured by a wavefront sensor, so that the complex amplitudes in every point of the entrance pupil are known. The incident field is split into its (ξ,η) components. The amplitudes of the matrix elements at a particular input/output polarization combination are directly measured by imaging the exit pupil onto a CCD camera while the phase is obtained interferometrically by combining the field at the exit pupil with a reference beam.

2.3. Experimental realization

2.3.1. Setup

We designed and built a coherent scatterometer, along with an interferometer functionality, based on temporal phase shifting interferometry. The design is basically the one of a coherent Fourier scatterometer (see Ref. [15]) where a reference mirror with a piezoelectric transducer is added to the open port of the beam-splitter. This setup allows us to determine the scattering matrix of any object of interest. The object under investigation is a periodic silicon on silicon square grating, described by the parameters listed in Table 2.1. Those parameters, which have been used as input values for the RCWA simulations, have been measured with atomic force microscopy (grating height) and scanning electron microscopy (grating period and MidCD). A schematic overview is shown in Fig. 2.2. The light from a He-Ne laser (S, $\lambda = 633\,nm$) is coupled to a single mode fiber (SMF); the light exiting the fiber is collimated ($L_1 = 20\,cm$) and the desired input polarization direction is set

Period (nm)	height (nm)	MidCD (nm)	SWA (Degrees)
500	130	216	85

Table 2.1: Physical dimensions of the grating under investigation.

with a Glan-Taylor polarizer (POL_{in} in the figure). To define the different states of polarization, we will use the notation provided by Section 2.2. A beam-splitter (BS) separates the beam for the sample and reference mirror arm. On the sample arm, the polarized light is focused on the grating with a microscope objective (MO) Leitz Wetzlar 20X infinity corrected, of numerical aperture NA $= 0.4$. In the reference arm, the beam is reflected by a $\lambda/20$ flat aluminum mirror controlled by a piezo translation stage (PZT). The reflected light from the grating in the exit pupil of the MO, as seen from the sample, is optically conjugated with the detector plane by two lenses ($L_2 = 40\,cm$ and $L_3 = 25\,cm$). Before the beam is recorded by the CCD camera, another polarizer (POL_{out}) allows to select the output polarization. In our scheme, output polarization (ξ, η) means that the polarizer is parallel to the input polarization (ξ, η), respectively.

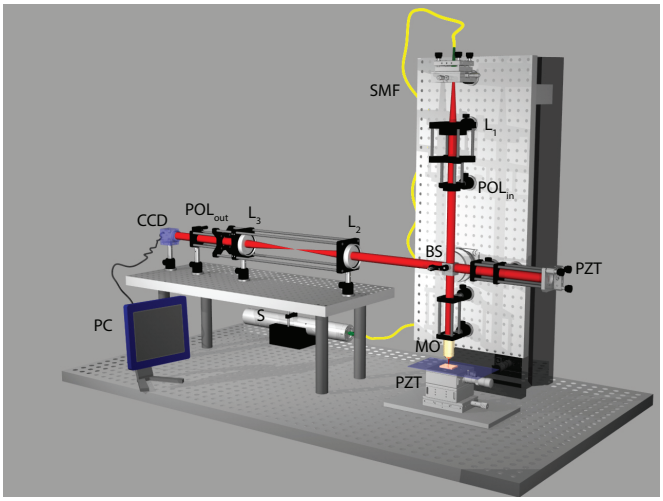

Figure 2.2: Schematic overview of the experimental setup. S: He-Ne laser; SMF: Single mode fiber; L1: Collimating lens; L2,L3: Telescopic lenses; BS: nonpolarizing beamsplitter; POL_{in}, POL_{out}: Polarizers; MO: Microscope objective; PZT: Piezo-electric translation stage; CCD: Data acquisition camera. Figure from [1].

2.3.2. Data acquisition

As previously mentioned, the setup (and therefore its working principle) can be employed to quantify the scattering properties of a variety of different structures. For the etched Silicon grating mentioned in the preceding section, input light of wavelength $\lambda = 633\,nm$ and a MO with numerical aperture NA $= 0.4$, only the zeroth order is captured by the CCD camera. Since there are no overlapping orders, the

spot does not have to be scanned to retrieve the phase difference between overlapping orders [15]. We obtain data for four input/output polarization combinations, namely: ξ-ξ, ξ-η, η-η and η-ξ. For each of them, intensity frames for several axial positions of the reference mirror are obtained by applying specific voltages to the piezo translation stage. The phase of the object is then reconstructed from the intensity data by means of the five-step phase shifting algorithm [24]. In fact, since only the zeroth order is present, only one complex amplitude is required to be calculated, thus the aforementioned algorithm is sufficient. When higher orders are also present, we will need more phase steps.
In the case of phase retrieval by temporal phase shifting algorithm, there is always an uncertainty in the piezo movement which results in an error in the intended phase change of the reference beam. This error can be minimized either by using phase retrieval algorithms that are less sensitive to the positioning errors and/or by choosing the correct frame corresponding to the intended phase shift (in our case it is $\pi/2$). We devised a correlation-based technique to minimize the error. The method is explained in Fig. 2.3. The phase retrieval algorithm is implemented with five intensity patterns recorded for the corresponding $\pi/2$ phase shifted reference arm of the interferometer. The correlation coefficient between the images is computed for displacement vs voltage, which indeed gives the information about the phase shift between the images. Five images are then chosen for the phase retrieval. A single image recorded by the detector is an interference pattern for a defined input and output polarization:

$$I_{\mu\nu} = I^{\text{ref}}_{\mu\nu} + I^{\text{obj}}_{\mu\nu} + 2\sqrt{I^{\text{ref}}_{\mu\nu} I^{\text{obj}}_{\mu\nu}}\cos(\phi_r), \tag{2.6}$$

where I^{ref} and I^{obj} indicate the beam intensities of the reference arm and the object arm, respectively and $\mu = \xi, \eta$ and $\nu = \xi, \eta$. If we shift the interference pattern by the five phase step values $\Phi_r = 0, \pi/2, \pi, 3\pi/2, 2\pi$, then we have a collection of five different measured intensities $\{I_r\}$ with $r = 1, \ldots, 5$. Acquiring five frames in identical input and output polarization conditions and then rearranging the intensities gives the phase in the pupil [25]:

$$\phi_{\mu,\nu} = \arctan\left[\frac{2(I_2 - I_4)}{2I_3 - I_5 - I_1}\right]. \tag{2.7}$$

To extract the five intensity maps from the experimental data, we analyze the correlation ρ_j of the captured experimental images j with respect to the first measured picture $j = 1$:

$$\rho_j = \frac{\sum_{\xi,\eta}[(I_j(\xi,\eta) - \langle I_j\rangle)\,(I_1(\xi,\eta) - \langle I_1\rangle)]}{\sqrt{[\sum_{\xi,\eta}(I_j(\xi,\eta) - \langle I_j\rangle)^2]\,[\sum_{\xi,\eta}(I_1(\xi,\eta) - \langle I_1\rangle)^2]}}, \tag{2.8}$$

where $I_j(\xi,\eta)$ indicates the j-th image at the pixel position (ξ,η), whilst $\langle I_j\rangle$ is the average over all the pixels of the j-th image.

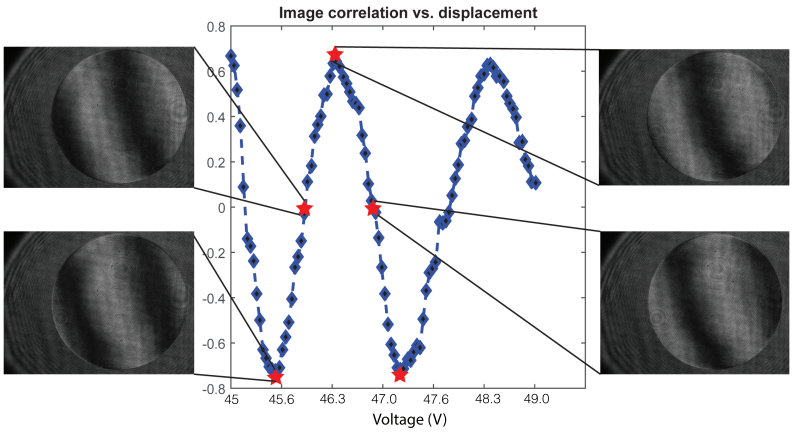

Figure 2.3: Correlation function ρ as a function of the voltage induced in the piezo transducer. We look at the maxima and minima of the correlation curve to monitor the movement of the piezo. Only four experimental images are shown for simplicity. Figure from [1].

Because we are recording images of an interference pattern, we expect the function ρ_j to have a cosine-like behavior (as confirmed by the data trend in Fig. 2.3). The five different phase steps Φ_r we need to consider correspond to the maxima and minima of ρ_j, along with points of $\rho_j = 0$ when $\Phi_r = \pi/2, 3\pi/2$, over one period. These points are highlighted with red marks in Fig. 2.3. In this way, by selecting the right images from the experimental data and substituting them into Eq. (2.7), we can retrieve the phase information we need. The obtained phase data is unwrapped using a quality guided path algorithm [26]. More details about this method are given in Appendix A; the interested reader should refer to [27–29] for a more exaustive discussion. Experimental data were treated with smoothing filter to minimize the noise influence using a gaussian kernel [28] in the windowed Fourier transform [29].

2.4. Comparison between measurement and simulation

To validate the measurements, rigorously simulated data have been obtained with the Rigorous Coupled Wave Analysis (RCWA) method [3, 30]. As input for the simulations we used the experimentally measured intensity and phase of the input field, as measured in the plane before the objective (MO in Fig. 2.2). In Fig. 2.4 and Fig. 2.5, the experimental and simulated intensities and phases of the scattered far field are shown for three different sets of input/output polarization, namely η-η, η-ξ, ξ-ξ. In case of a not-birefringent grating we assume η-ξ and ξ-η to be identical. Since in our example the scattered far field consists only of the zeroth order, we immediately obtain the complex elements of the scattering matrix.

The measured far field intensities and phases show a good match between experiments and simulations. The differences are attributed to extra insertion losses

and noise that have not been taken into account in the simulations. In Fig. 2.5, the deviation between experimental and simulated phase in the $\eta - \xi$ case for normal incidence can be attributed to the low intensity levels in the far fields used to reconstruct the phase map. Finally, we add that the ability to obtain the phase maps defines the value of the technique for phase sensitive scatterometry. With phase and amplitude knowledge of the scatterer, all field components (in our case, reflected) from the object within the numerical aperture of the optical system, except a constant phase, are obtained.

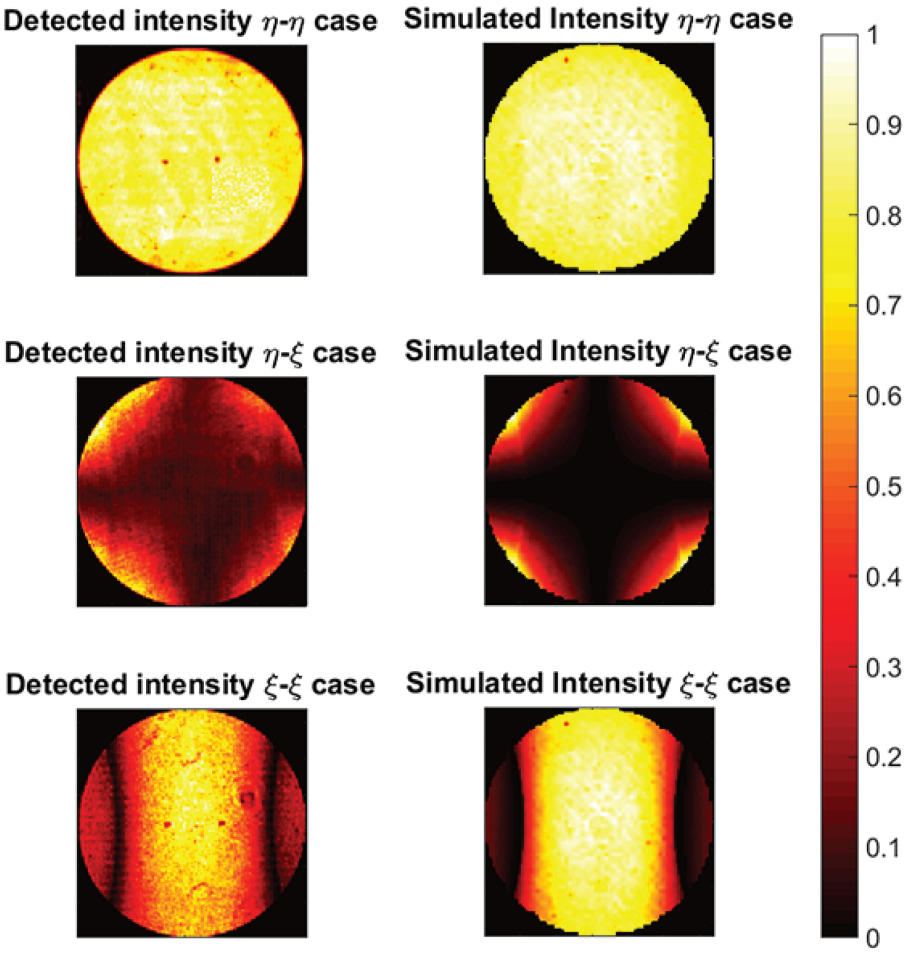

Figure 2.4: Measured (left) and simulated (right) intensities of the far field scattered by a grating illuminated by a focused field for different combinations of input and output polarizations. The incident wavelength is $633\,nm$, the numerical aperture is NA = 0.4. The grating parameters are given in Table 2.1. Figure from [1].

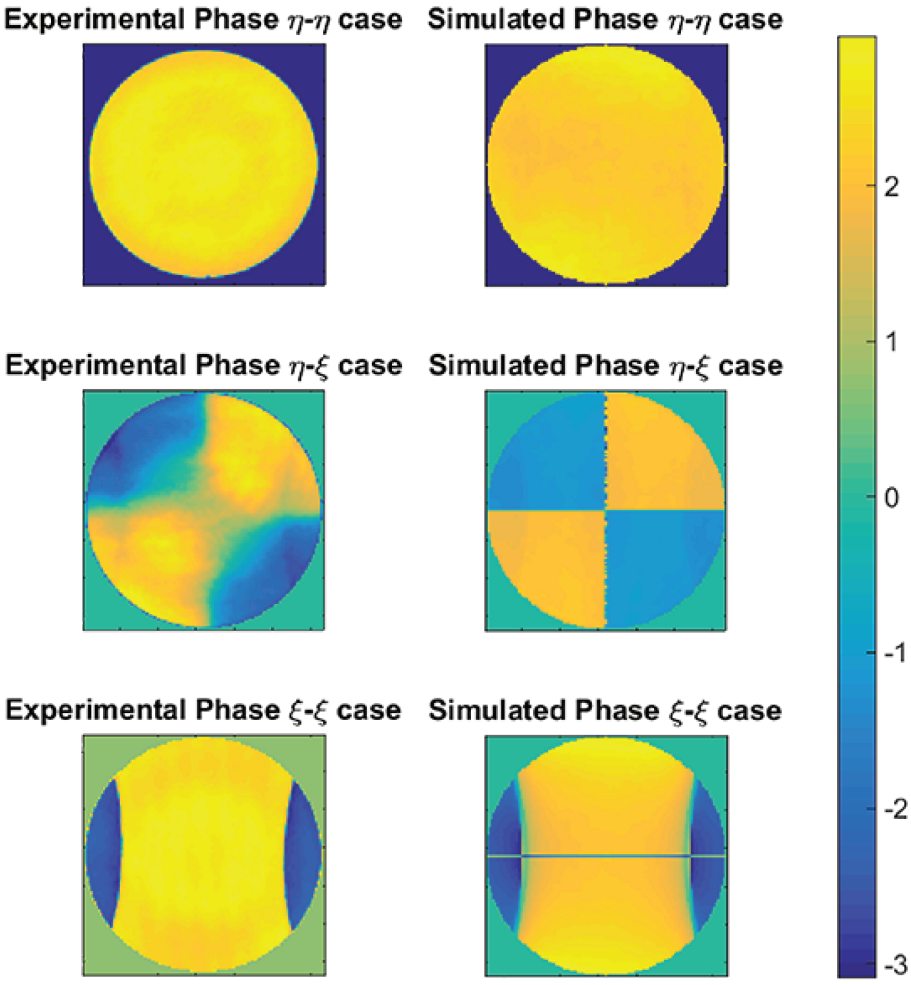

Figure 2.5: Phase of the scattered far field retrieved from measurements (left) and from simulations (right) for different combinations of input and output polarizations. The incident wavelength is $633\,nm$, the numerical aperture is NA = 0.4. The grating parameters are given in Table 2.1. Figure from [1].

2.5. Conclusions

In this chapter we have introduced a fast and reliable way to obtain the entire scattering matrix of a periodic object by measuring the phase of the scattered field from all angles within the numerical aperture of the system, using ICFS. With ICFS one is able to extend optical scatterometry to its maximum potential. The method presented here provides information on the scattering matrix resolved over polarization for all scattering angles, which can be extended to higher diffraction orders if they exist. Although the results presented above are for small NA (0.4) and long wavelength ($633\,nm$), it can be scaled to higher NA and shorter wavelengths. This approach is not only limited to periodic objects and thus can be applied when scattered light from an arbitrary scatterer is used to retrieve information about it. Because the complex scattering matrix provides all possible information, we believe that this method can also be used to set the limits of optical scatterometry in different applications such as object parameter retrieval, detection of (sub-wavelength) particle contamination, defect detection and surface characterisation. Furthermore, depending on the features that are to be retrieved, one can only select the measured data that contain the most sensitive part of the information for this feature and discard the other data. In this way, the speed of scatterometry can be increased.

References

[1] N. Kumar, L. Cisotto, S. Roy, G. K. P. Ramanandan, S. F. Pereira, and H. P. Urbach, *Determination of the full scattering matrix using coherent fourier scatterometry,* Appl. Opt. **55**, 4408 (2016).

[2] M. G. Moharam and T. K. Gaylord, *Rigorous coupled-wave analysis of planar-grating diffraction,* J. Opt. Soc. Am. **71**, 811 (1981).

[3] L. Li, *Use of fourier series in the analysis of discontinuous periodic structures,* J. Opt. Soc. Am. A **13**, 1870 (1996).

[4] S. Roy, A. C. Assafrão, S. F. Pereira, and H. P. Urbach, *Coherent fourier scatterometry for detection of nanometer-sized particles on a planar substrate surface,* Opt. Express **22**, 13250 (2014).

[5] V. F. Paz, S. Peterhansel, K. Frenner, and W. Osten, *Solving the inverse grating problem by white light interference fourier scatterometry,* Light Sci Appl **1** (2012), 10.1088/0150-536X/11/4/005.

[6] H.-T. Huang, W. Kong, and F. L. T. Jr., *Normal-incidence spectroscopic ellipsometry for critical dimension monitoring,* Applied Physics Letters **78**, 3983 (2001), http://dx.doi.org/10.1063/1.1378807 .

[7] Q. Zhan and J. R. Leger, *High-resolution imaging ellipsometer,* Appl. Opt. **41**, 4443 (2002).

[8] P. Boher, J. Petit, T. Leroux, J. Foucher, Y. Desieres, J. Hazart, and P. Chaton, *Optical fourier transform scatterometry for ler and lwr metrology,* Proc. SPIE **5752**, 192 (2005).

[9] M. Wurm, F. Pilarski, and B. Bodermann, *A new flexible scatterometer for critical dimension metrology,* Review of Scientific Instruments **81**, 023701 (2010), http://dx.doi.org/10.1063/1.3280160 .

[10] O. el Gawhary et al., *Performance analysis of coherent fourier scatterometry,* Appl. Phys. B **105**, 775 (2011).

[11] D. Kim, M. Jin, H. Lee, S. Kim, and R. Magnusson, *Snapshot conical diffraction phase image measurement in angle-resolved microellipsometry,* in *Imaging and Applied Optics* (Optical Society of America, 2013) p. CTu3C.5.

[12] A. Faridian, V. F. Paz, K. Frenner, G. Pedrini, A. D. Boef, and W. Osten, *Phase-sensitive structured illumination to detect nanosized asymmetries in silicon trenches,* Journal of Micro/Nanolithography, MEMS, and MOEMS **14**, 021104 (2015).

[13] M. H. Madsen and P.-E. Hansen, *Imaging scatterometry for flexible measurements of patterned areas,* Opt. Express **24**, 1109 (2016).

[14] R. M. Silver, B. M. Barnes, R. Attota, J. Jun, M. Stocker, E. Marx, and H. J. Patrick, *Scatterfield microscopy for extending the limits of image-based optical metrology,* Appl. Opt. **46**, 4248 (2007).

[15] N. Kumar, O. el Gawhary, S. Roy, S. F. Pereira, and H. P. Urbach, *Phase retrieval between overlapping orders in coherent fourier scatterometry using scanning,* Journal of the European Optical Society - Rapid publications **8** (2013).

[16] S. Roy, N. Kumar, S. F. Pereira, and H. P. Urbach, *Interferometric coherent fourier scatterometry: a method for obtaining high sensitivity in the optical inverse-grating problem,* Journal of Optics **15**, 075707 (2013).

[17] L. Rayleigh, *On the dynamical theory of gratings,* Proceedings of the Royal Society of London A: Mathematical, Physical and Engineering Sciences **79**, 399 (1907).

[18] P. M. van den Berg, *Reflection by a grating: Rayleigh methods,* J. Opt. Soc. Am. **71**, 1224 (1981).

[19] A. V. Tishchenko, *Numerical demonstration of the validity of the rayleigh hypothesis,* Opt. Express **17**, 17102 (2009).

[20] K. Knop, *Rigorous diffraction theory for transmission phase gratings with deep rectangular grooves,* J. Opt. Soc. Am. **68**, 1206 (1978).

[21] J. Chandezon, G. Raoult, and D. Maystre, *A new theoretical method for diffraction gratings and its numerical application,* Journal of Optics **11** (1980), 10.1088/0150-536X/11/4/005.

[22] M. N. Vesperinas, *Scattering and diffraction in physical optics,* (World Scientific Publishing Co., 2005) Chap. 9.9, pp. 316–319, 2nd ed.

[23] P. Török and T. Wilson, *Rigorous theory for axial resolution in confocal microscopes,* Optics Communications **137**, 127 (1997).

[24] D. Malacara, M. Servin, and Z. Malacara, *Interferogram analysis for optical testing,* (Boca Raton, FL: CRC Press, 2005) Chap. 7, 2nd ed.

[25] N. Kumar, *Coherent fourier scatterometry,* (Thesis, TU Delft, 2014).

[26] M. A. Herraez, D. R. Burton, M. J. Lalor, and M. A. Gdeisat, *Fast two-dimensional phase-unwrapping algorithm based on sorting by reliability following a noncontinuous path,* Applied Optics **41** (2002).

[27] M. Gdeisat and F. Lilley, *Two-dimensional phase unwrapping problem,* Available online at www.ljmu.ac.uk/geri/phase-unwrapping.htm.

[28] S. Qian, *Introduction to time-frequency and wavelet transform,* (Englewood Cliffs, NJ: Prentice-Hall, 2002) 2nd ed.

[29] Q. Kemao, *Two-dimensional windowed fourier transform for fringe pattern analysis: Principles, applications and implementation,* Optics and Lasers in Engineering **45**, 304 (2007).

[30] M. van Kraaij and J. Maubauch, *A more efficient rigorous coupled-wave analysis algorithm,* Prog. in Industrial Mathematics at ECMI 2004 .

3

Side-wall angle detection enhancement through spiral mode projection method

I have not failed. I've just found 10,000 ways that won't work.

Thomas A. Edison

This is the first of a series of three chapters in which we focus our efforts in studying alternative ways to estimate the side-wall angle of a scatterer, more precisely a cliff-like object. In fact, as it has been been already pointed out in this dissertation, having a fast and precise method to measure the side-wall angle of periodic (or non-periodic) structures is still a very challenging problem in lithographic applications. For this reason, over the years, many techniques have been proposed to circumvent this limitation, with the final goal to give the most precise geometrical description of a given target. In this chapter we aim at introducing the basis for a new method to detect the side-wall angle in a fast and reliable way. The novelty of this work is the use of the spiral spectrum of a light beam for side-wall angle measurements, i.e., the light transmitted by a particular structure is projected onto properly tailored spiral modes and only the most sensitive mode to the side wall angle is detected and processed.

Parts of this chapter have been published in Proc. SPIE **9526**, 2952607-952607-8 (2015) [1].

3.1. Introduction

Nowadays, the demand for faster, smaller and lighter electronic devices sets stringent requirements for nano-lithography [2]. As we have already discussed in the previous chapter, modern electronic chips can be modeled with optical gratings, which are often used as targets for fine-tuning of the lithographic machines. These targets are usually described by four different shape parameters that fully characterize their geometrical profile, namely MidCD (Middle Critical Dimension), side-wall angle (SWA), height and period. The knowledge of these parameters is a key factor to fabricate chips accordingly to the initial design; the better the error estimation of their values, the more devices will behave as predicted. Many clever methods have been developed in recent years to increase the precision with which the shape parameters are retrieved. An example is Coherent Fourier Scatterometry (CFS), partially described in Chapter 2, with which it has been demonstrated [3] that it is possible to retrieve, with very high sensitivity, the values of the aforementioned quantities. Nonetheless, regarding the side-wall angle measurement, the uncertainty is still quite large compared to the other parameters, thereby making conventional detection techniques not very appealing for its determination. As a consequence, over the years, several new methods have been designed to measure, as precisely as possible, the SWA value [4–6]. Available techniques try to exploit all the fundamental properties of light, e.g. the energy spectra and the energy density of light signals, but in the past few years much attention has been given to the study of the interaction between angular momentum and matter. It is indeed known that angular momentum can contain not only a spin contribution, associated to the polarization of the electromagnetic fields, but also an orbital contribution associated to the spatial profile of the light beam amplitude and phase-front [7, 8]. Furthermore, it is possible, within the paraxial regime, to decouple them [9–11]. An important difference between the spin angular momentum and the orbital angular momentum is that the former manifests itself in the vectorial nature of a light field and is thus sensitive to material anisotropies; conversely, the orbital angular momentum can be associated to the topological properties of a light field and hence it is sensitive to phase gradients and discontinuities. It is interesting to observe that in the past years, the orbital momentum has resulted in important applications in fields that range from optical tweezers in biosciences, to microfluidics and micromechanics [12–15].

In this chapter we describe a proof of concept of an experimental technique that could potentially increase the precision of the SWA detection, while keeping the experimental setup fast and non-invasive. The key point is to look at the spiral mode of a light beam, using a technique called *spiral mode projection*. The potential of this approach has already been demonstrated [16, 17] and it has also been used to determine, with incredible precision, the height of thin nanolayers [18]. In this technique, the target is illuminated with a beam presenting a convenient spatial shape (amplitude and phase), the reflected (or transmitted) signal is then expanded into spiral modes; information regarding the target can be acquired by analyzing the corresponding spiral spectrum.

The chapter is organized as follows. In Section 3.2 we describe two possible

ways of creating an optical beam carrying singularities, namely by an amplitude or a phase hologram; furthermore we look at the Fraunhofer propagation of a beam created with such an hologram. In Section 3.3 we explain the Spiral Mode decomposition of a field and we present three different cases of illumination: a Gaussian beam, a $LG_{0,1}$ and a $LG_{1,1}$. For each of them we study the interaction with a phase step characterized by a certain side-wall angle α. Section 3.4 describes, from a numerical point of view, the mode decomposition for the case of a Gaussian beam incident, which is chosen as the preferred type of illumination based on the results of Section 3.3. The outcome of the numerical simulation are then compared with experimental results in Section 3.5. Finally, Section 3.6 summarizes the most relevant findings.

3.2. Two ways to generate a light beam with singularities

3.2.1. Fork Hologram

Given that we have introduced the concept of a beam with a phase singularity [19, 20], it is also useful to remind the reader how such a light field can be generated experimentally. A flexible way to produce modes with singularities is through the use of computer generated holograms. The interference pattern of a simple reference beam (plane wave) and a second one containing an optical vortex is known in literature as *fork hologram*. Let us consider a plane wave of the form:

$$E_{\text{ref}} = E_{\text{pw}}\, e^{i(k_x x + k_z z)}, \tag{3.1}$$

with an incident angle $\psi = \arcsin \dfrac{k_x}{k}$ and intensity $|E_{\text{pw}}|^2$. In the $z = 0$ plane, the interference pattern with a beam containing an optical vortex, $E_{\text{vor}} = E_{\text{v,0}}(r)\, e^{il\phi}$, is given by:

$$I = |E_{\text{ref}} + E_{\text{vor}}|^2 = |E_{pw}|^2 + |E_{\text{v,0}}(r)|^2 + 2\,\Re\left[E_{\text{pw}}\, E_{\text{v,0}}(r)\right]\cos\left(k_x x - l\phi\right). \tag{3.2}$$

If we ignore the amplitude variation of the doughnut beam and retain only the important phase information in the form of a spatially varying transmissivity [19]:

$$T = \frac{1}{2}\left[1 + \cos(k_x x - l\phi)\right]. \tag{3.3}$$

It is instructive to distinguish between two types of holograms: amplitude and phase holograms. The former absorbs light in the dark fringes and transmits light in the bright ones, hence the diffracted beam acquires a specific phase-front defined by the fringe pattern. The latter type of hologram does not absorb light (in theory) but changes the optical retardation in space, according to the printed phase pattern. In Figs. 3.1 and 3.2 we can see two examples of phase holograms for $l = +1$ and $l = +2$. We discuss here the main characteristics of these two types of hologram:

- **Amplitude holograms**: If the intensity pattern from equation Eq. (3.2) is directly printed on a photographic film (or display onto a spatial light modulator) and illuminated by a Gaussian beam propagating along the $z-$axis, just

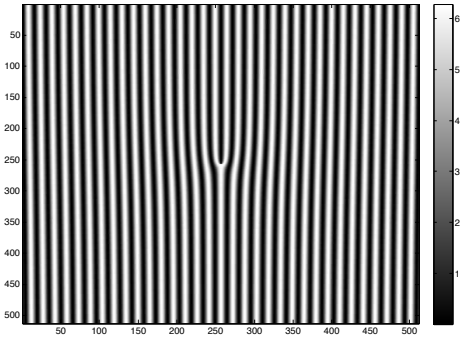

Figure 3.1: Phase holograms obtained for $l = +1$. The retardation is given in the $[0, 2\pi]$ range.

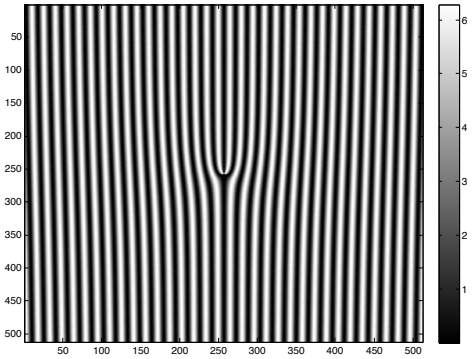

Figure 3.2: Phase holograms obtained for $l = +2$. The retardation is given in the $[0, 2\pi]$ range.

after the hologram the field will be:

$$E_t = T\,A_G\,e^{-r^2/w_0^2}, \tag{3.4}$$

where A_G is the central amplitude, w_0 the spot size of the beam and T is the transmission function of the hologram. Substituting for T in Eq. (3.3), we find:

$$E_t = \frac{A_G}{2}\,e^{-r^2/w_0^2} + \frac{A_G}{4}\,e^{-r^2/w_0^2}e^{i(k_x x - l\phi)} + \frac{A_G}{4}\,e^{-r^2/w_0^2}\,e^{-i(k_x x - l\phi)}. \tag{3.5}$$

We can therefore recognize that the outgoing beam is consisting of a zero order beam propagating along the axis and two (conjugate) first order diffracted beams, each of them containing a singularity of opposite charge $+l$ and $-l$. In practice, binary holograms are most frequently used, in this case the transmission function of the hologram is:

$$T = \frac{1}{2}\left[1 + \text{sign}(\cos(k_x x - l\phi)\right], \tag{3.6}$$

which can be written using the formalism of Fourier series:

$$T = \frac{1}{2} + \frac{1}{2}\sum_{s=-\infty}^{+\infty} g(s)\,e^{i(2s+1)(k_x x - l\phi)}, \tag{3.7}$$

with $g(s) = \frac{2\,(-1)^{2s}}{\pi k_x (2s+1)}$.
Therefore the output field is composed by an infinite number of orders, each of them carrying a vortex with topological charge $l(2s+1)$ and propagating at the angle:

$$\phi_s = \sin^{-1}\left(\frac{(2s+1)k_x}{k}\right). \tag{3.8}$$

- **Phase hologram**: In the case of a phase hologram, the transmission function becomes:

$$t(x,y) = e^{i\,\frac{a}{2}[1+\cos(k_x x - l\phi)]}, \tag{3.9}$$

where a is the phase depth of the hologram. If we rewrite this equation as follows:

$$t(x,y) = e^{i\frac{a}{2}}\,e^{i\frac{a}{2}\sin\left(\frac{\pi}{2}+k_x x - l\phi\right)}, \tag{3.10}$$

we can use the expansion:

$$e^{ih\sin(\gamma)} = \sum_{m=-\infty}^{+\infty} J_m(h)\,e^{im\gamma}, \tag{3.11}$$

to represent the complex exponential function; the term $J_m(h)$ represents the Bessel function of order m. Inserting Eq. (3.11) into Eq. (3.10) we obtain:

$$\begin{aligned} t(x,y) &= e^{i\frac{a}{2}} \sum_{m=-\infty}^{+\infty} J_m\left(\frac{a}{2}\right) e^{im\left(\frac{\pi}{2}+k_x x-l\phi\right)} \\ &= e^{i\frac{a}{2}} \sum_{m=-\infty}^{+\infty} i^m J_m\left(\frac{a}{2}\right) e^{im(k_x x-l\phi)}. \end{aligned} \tag{3.12}$$

Eq. (3.12) shows that, for a sinusoidal phase hologram, all orders of beam diffraction are present. Each of them has a topological charge $l' = m\,l$ (where l was the initial value of the vortex beam used to create the hologram) and travels at an angle:

$$\alpha_m = \sin^{-1}\left(m\,\frac{k_x}{k}\right). \tag{3.13}$$

3.2.2. Kummer beams

In the literature it is widely claimed that pure azimuthal Laguerre-Gaussian beams $LG_{0,l}$ can be created with amplitude (or phase) modulating devices like fork holograms and spiral phase plates; nevertheless, this is not entirely true [21]. In this section we therefore deal with the mathematical problem of deriving the exact solution for the far-field diffraction pattern produced by a fork hologram, when it is illuminated by a Gaussian beam.

Let us consider a reference frame with cylindrical coordinates (ρ, φ, z) such that the $z = 0$ plane coincides with the fork hologram plane. We also make the assumption that the Gaussian beam illuminates the fork hologram in such a way that its waist lies in the grating plane. In this conditions, the complex amplitude of the Gaussian beam at $z = 0$ assumes the form:

$$U_G(\rho, \phi, z = 0) = e^{-\frac{\rho^2}{w_0^2}}. \tag{3.14}$$

As we already know from the previous sections, the net contribution of the fork hologram is just a phase modulation $e^{il\phi}$, where l depends on the diffracted order observed. Nevertheless, to be consistent with Maxwell equations, the outgoing field will have the form:

$$U_L(\rho, \phi) = A_0(\rho)\, e^{-\frac{\rho^2}{w_0^2}}\, e^{il\phi}. \tag{3.15}$$

The far field observed at a distance z_1 from the fork hologram is given by:

$$U_{FF}(r, \theta, z_1) = \frac{e^{i\left(kz_1+\frac{k}{2z_1}r^2\right)}}{i\,\lambda\,z_1} \iint U_L(\rho, \phi)\, e^{-\frac{2\pi i}{\lambda z_1} r\cdot\rho}\, \rho\, d\rho\, d\phi, \tag{3.16}$$

inserting Eq. (3.15) we get:

$$U_{FF}(r,\theta,z_1) = \frac{e^{i\left(kz_1+\frac{k}{2z_1}r^2\right)}}{i\,\lambda\,z_1}\int_0^{+\infty} A_0(\rho)\,e^{-\frac{\rho^2}{w_0^2}}\,\rho\,d\rho\int_0^{2\pi} e^{i\left[l\phi-\frac{k}{z_1}\rho\,r\,\cos(\phi-\theta)\right]}d\phi. \tag{3.17}$$

Using one of the integral representations of the Bessel functions of the first kind:

$$J_m(t) = \frac{1}{2\pi}\int_0^{2\pi} e^{\pm i(m\gamma - t\,\sin\gamma)}d\gamma, \tag{3.18}$$

and the substitution $\phi-\theta = \psi - \pi/2$, it follows that:

$$\int_{-\theta+\frac{\pi}{2}}^{2\pi-\theta+\frac{\pi}{2}} e^{i\left(l(\theta+\psi-\frac{\pi}{2})-\frac{k}{z_1}\rho\,r\,\sin\psi\right)}d\psi = 2\pi\,(-i)^l\,e^{il\theta}\,J_l\left(\frac{k\,\rho\,r}{z_1}\right), \tag{3.19}$$

which brings us:

$$U_{FF}(r,\theta,z_1) = (-1)^l\,\frac{e^{i\left(kz_1+\frac{k}{2z_1}r^2\right)}}{i^{l+1}\,\lambda\,z_1}\,e^{il\theta}\int_0^{+\infty} A_0(\rho)J_l\left(\frac{k\,\rho\,r}{z_1}\right)e^{-\frac{\rho^2}{w_0^2}}\,\rho\,d\rho. \tag{3.20}$$

For simplicity, let us consider the following dependance for the amplitude of the outgoing beam: $A_0(\rho) = \rho$. The integral in the rightmost part of Eq. (3.20) can therefore be evaluated using the gamma function Γ and the *confluent hypergeometric Kummer function M*[1]:

$$\int_0^{+\infty} J_\nu(ct)\,e^{-p\,t^2}t^{\alpha-1}dt = c^\nu p^{-(\alpha+\nu)/2}2^{-\nu-1}\frac{\Gamma\left[(\alpha+\nu)/2\right]}{\Gamma(\nu+1)}M\left(\frac{\alpha+\nu}{2},\nu+1,-\frac{c^2}{4\,p}\right), \tag{3.21}$$

therefore, substituting $\nu = l$, $c = \frac{kr}{z_1}$, $p = \frac{1}{w_0^2}$ and $\alpha = 3$ we obtain:

$$U_{FF}(r,\theta,z_1) = w_0^3\,(-1)^l\frac{e^{i\left(kz_1+\frac{k}{2z_1}r^2\right)}}{i^{l+1}\,\lambda\,z_1}\,\frac{\Gamma\left[(3+l)/2\right]}{\Gamma(l+1)}\left(\frac{krw_0}{2z_1}\right)^l\times e^{il\theta}M\left(\frac{3+l}{2},l+1,-\frac{k^2r^2w_0^2}{4z_1^2}\right). \tag{3.22}$$

With the substitution:

$$w_{z_1} = \frac{\lambda\,z_1}{\pi\,w_0}, \tag{3.23}$$

this last equation can be rearranged and the form:

$$U_{FF}(r,\theta,z_1) = A_l(r,z_1)\left(\frac{r}{w_{z_1}}\right)^l e^{il\theta}\,M\left(\frac{3+l}{2},l+1,-\frac{r^2}{w_{z_1}^2}\right). \tag{3.24}$$

[1] A.P. Prudnikov, Yu.A. Brychkov, O.I. Marichev, *Integrals and Series: Special Functions*, Nauka, Moscow, 1983: equation 2.12.9.3

Another equivalent way to express the far field diffraction pattern of a Gaussian beam behind a fork hologram is to use a superposition of two Bessel function. In particular[2]:

$$\int_0^{+\infty} J_\nu(ct)\, e^{-p\,t^2}\, t^{\alpha-1}\, dt = \frac{c\sqrt{\pi}}{8\,p^{3/2}}\, e^{-\frac{c^2}{8p}} \left[I_{(\nu-1)/2}\left(\frac{c^2}{8p}\right) - I_{(\nu+1)/2}\left(\frac{c^2}{8p}\right)\right], \quad (3.25)$$

where I_m is the m^{th}-order modified Bessel function. This is valid when $\alpha = 2$. Therefore, the far field becomes:

$$U_{FF}(r,\theta,z_1) = A_l(r,z_1)\,\frac{1}{8\,\pi\sqrt{\pi}}\,\frac{z_1^2}{k^2 w_{z_1}^2}\,\frac{r}{w_{z_1}}\, e^{il\theta}\times$$
$$e^{-\frac{r^2}{2\,w_{z_1}^2}} \left[I_{\frac{l-1}{2}}\left(\frac{r^2}{2\,w_{z_1}^2}\right) - I_{\frac{l+1}{2}}\left(\frac{r^2}{2\,w_{z_1}^2}\right)\right], \quad (3.26)$$

where for w_{z_1} is still given by Eq. (3.23).

3.3. Laguerre-Gaussian mode expansion

After this brief introduction on beams carrying phase singularities and how it is possible to create them, we concentrate our attention on how a light field can be expanded in terms of Laguerre-Gaussian (LG) beams [22–24]. This type of beams are described, at their waist, by the following profile:

$$LG_{p,m}(r,\theta) = \sqrt{\frac{2\,p!}{\pi(p+|m|)!}}\,\frac{1}{w_0}\left(\frac{r\sqrt{2}}{w_0}\right)^{|m|} L_p^{|m|}\left(\frac{2\,r^2}{w_0^2}\right) e^{\left(-\frac{r^2}{w_0^2}\right)} e^{(im\theta)} \quad (3.27)$$

where the symbol $L_p^{|m|}$ stands for the Laguerre polynomials and w_0 is the waist size. The amplitude and phase profile of these beams is characterized by two integer numbers, usually labeled as p and m. The former can take any non-negative value and determines the radial shape (and therefore the node number) of the beam distribution; the latter, which can take any integer number, describes the azimuthal phase dependence of the mode. When $m \neq 0$, the LG modes contain optical vortices, with topological charge, or winding number, given by m itself. We notice that in the case $p = m = 0$ the light profile is nothing but the simple Gaussian beam. Figures 3.3 and 3.4 show an example of $LG_{0,1}$ and $LG_{1,2}$, respectively. The Laguerre-Gaussian functions are a complete orthonormal set of functions; in fact we can introduce the following inner product for the Laguerre polynomials:

$$\int_0^{+\infty} L_m^\alpha(x)\, L_n^\alpha(x)\, d\mu(x) = \frac{\Gamma(m+\alpha+1)}{m!}\,\delta_{n,m} \quad \text{with} \quad d\mu(x) = x^\alpha e^{-x} dx \quad (3.28)$$

by defining the functions $\psi_m(x) = x^{\alpha/2} e^{-x/2} L_m^\alpha(x)$ and $\psi_n(x) = x^{\alpha/2} e^{-x/2} L_n^\alpha(x)$ we get:

$$\int_0^{+\infty} \psi_n(x)\,\psi_m^*(x)\, dx \quad \in L^2(\mathbb{R}). \quad (3.29)$$

[2]See note 1 page 29

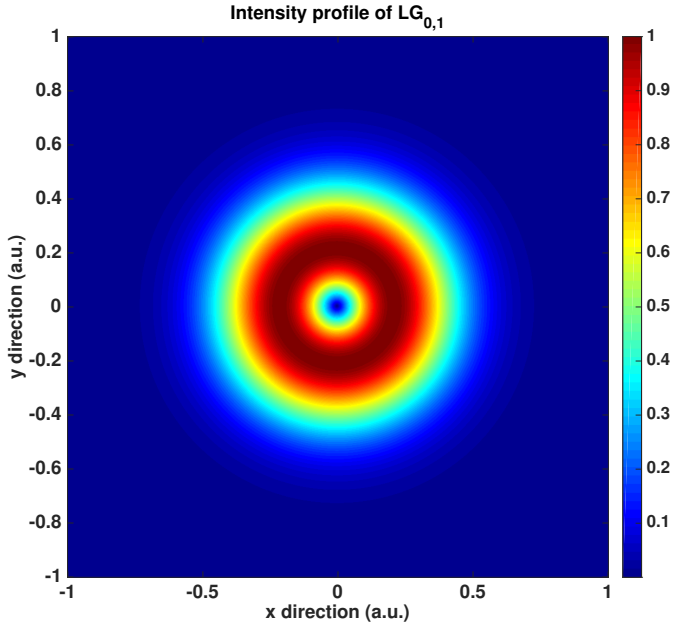

Figure 3.3: Intensity profile of a Laguerre-Gaussian beam with $p = 0$ and $m = 1$

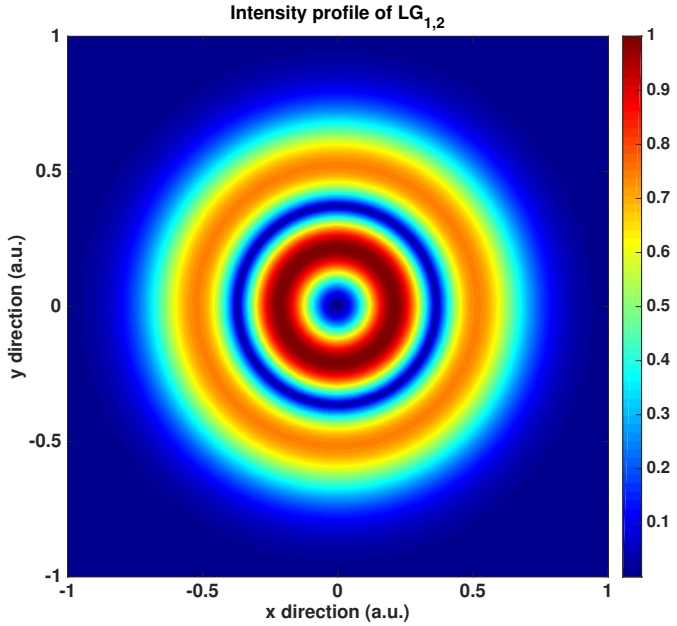

Figure 3.4: Intensity profile of a Laguerre-Gaussian beam with $p = 1$ and $m = 2$

It is easy to see that if $x = 2r^2/w_0^2$ and $\alpha = |m|$ the function $\psi_n(x)$ represents exactly the Laguerre-Gaussian modes. This property allows us to expand any field as a vector state in that basis:

$$f(r,\theta) = \sum_{p,m} c_{p,m}\, LG_{p,m}(r,\theta), \tag{3.30}$$

where:

$$c_{p,m} = \int_0^{2\pi}\int_0^{+\infty} f(r,\theta)\; LG^*_{p,m}(r,\theta)\, r\, dr\, d\theta. \tag{3.31}$$

In this way, we can look at the spiral decomposition of any given input field and, for instance, observe its change after the interaction with a sample. By looking at how each individual mode gets modified by the presence of an object, we can infer, and therefore quantify, important properties that define it.

More specifically it is possible to project a generic field $f(r,\theta)$ into spiral harmonics $\exp(im\theta)$ using a rather simple expression; this accounts for the weight of all the LG modes with identical azimuthal number m, independently of the radial number p:

$$f(r,\theta) = \frac{1}{\sqrt{2\pi}} \sum_{m=-\infty}^{m=+\infty} a_m(r)\, \exp(im\theta), \tag{3.32}$$

where:

$$a_m(r) = \frac{1}{\sqrt{2\pi}} \int_0^{2\pi} f(r,\theta)\, \exp(-im\theta)\, d\theta, \tag{3.33}$$

(r,θ) are coordinates in the transverse plane and $a_m(r)$ describes the radial dependence associated with every spiral mode.

In this chapter we focus on the analysis, in the limit of paraxial optics, of the interaction between a phase object and an input beam; this means that such a target will mainly act on the overall phase of the beam which is interacting with it, leaving its amplitude almost unchanged. The scatterer, in our model, is a step with a specific height and side-wall angle (SWA) that has been studied both theoretically and experimentally. The goal of our study is to prove that the we can infer the height and side-wall angle of the structure under study by exploiting the spiral mode change during the interaction between the light and the scatterer. The procedure we apply is similar to a previous work [17], although in our case the detection of the zeroth order mode is used to estimate a specific parameter, namely the side-wall angle.

In the next subsections we will analyze how different Laguerre-Gaussian modes interact with a cliff-like object, characterized by a side-wall angle α. This object is assumed to be a pure phase target, hence the amplitude profile of the incoming beam is left untouched. We will look at the energy content, after the interaction with the aforementioned object, of three different topological charges, namely $LG_{0,0}$, $LG_{0,1}$, $LG_{1,1}$. This analysis is necessary to find out which input mode is more sensitive to a small side-wall angle change. The height of the object under study was designed to give a phase change of π across the step in reflection, therefore its height must be $\lambda/4$.

3.3.1. Gaussian beam incidence

We begin by considering a Gaussian beam impinging on a phase step target which can be modeled by the following equation:

$$\phi_t(x) = \frac{h}{2}\left[1 + \mathrm{erf}\left(t\sqrt{\pi}\,\frac{x}{h}\right)\right], \tag{3.34}$$

where the symbol erf represents the Gaussian Error Function defined by:

$$\mathrm{erf}(x) = \frac{2}{\sqrt{\pi}}\int_0^x e^{-s^2}\,ds, \tag{3.35}$$

h and t represent the height of the step and a direct link to the slope of this function, respectively. In fact, the first derivative of this function is given by $t\,\exp(-x^2)$, hence its slope - in other words, the side-wall angle - varies with the parameter t in a neighboring region of zero. To visualize this function, a plot of $\phi_t(x)$ is given in Fig. 3.5 for several values of the parameter t, which can be translated into different slope angle values.

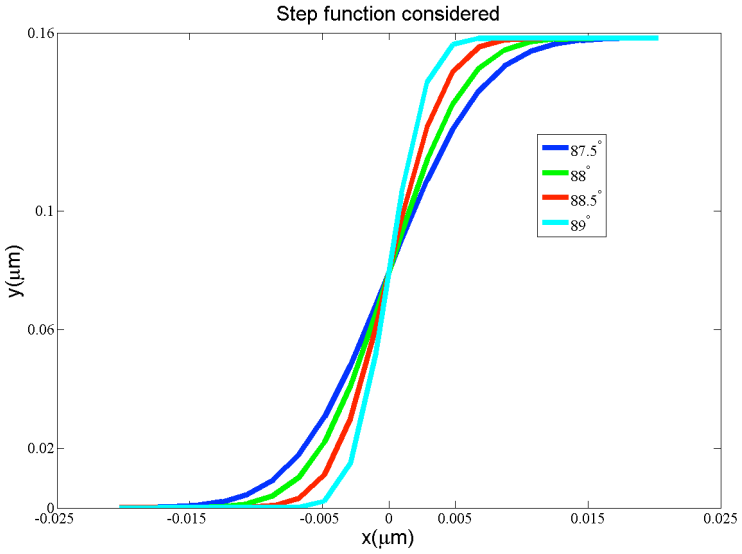

Figure 3.5: Plot of the function $\phi_t(x)$ given by Eq. 3.34 for different values of t, which can be translated into different slope angle values.

The expression of the energy content (weight) carried by a generic mode m is:

$$P_m = \frac{c_m}{\sum_q c_q}, \tag{3.36}$$

in which:

$$c_m = \left|\int_0^{+\infty} a_m(r)\,r\,dr\right|^2, \tag{3.37}$$

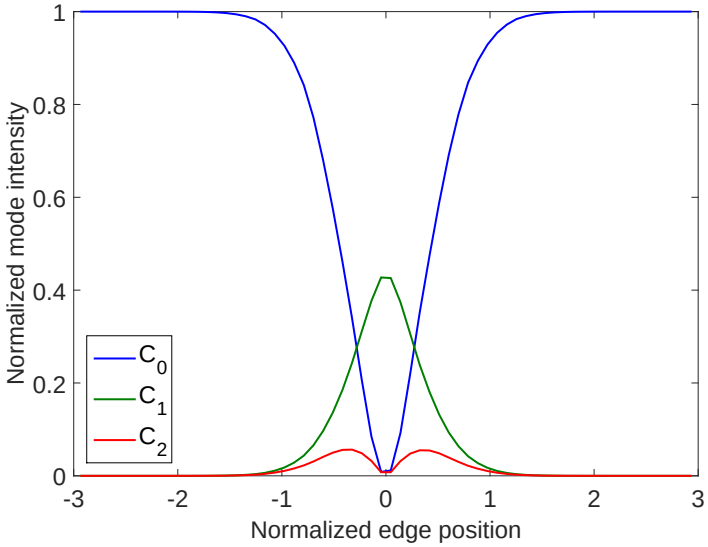

Figure 3.6: Mode power as function of the edge position normalized to the waist of the beam for a perfect $90°$ edge at the center of the beam, for a π phase shift.

and $a_m(r)$ is given by Eq. (3.33). The weight of the first three modes, corresponding to $m = 0, 1, -1$, are plotted in Fig. 3.6; it can be readily seen that the zeroth order mode presents the biggest change in intensity when we scan the sample in a direction perpendicular to the beam; we therefore believe it is more practical to monitor the signal corresponding to this mode. The net effect of the cliff is evident if we graphically compare the mode expansion before (Fig. 3.7) and after (Fig. 3.8) the interaction with the cliff; by doing so we also notice that only the low order modes are worth monitoring because the higher orders are too small to be detected.

When the side-wall angle we are interested in is not $90°$ but has a (smaller) value close to it, the signal - energy content - we need to be able to detect is quite small, on the order of 10^{-4} or less. Fig. 3.9 shows the difference between P_m values when $\alpha = 90°$ and when $\alpha = 87°$; this gives us an idea of the detection sensitivity that is needed in order to capture an angle difference of $3°$. Although many experimental techniques nowadays available are able to resolve an angle difference of $3°$, this could be easily detectable in our case as well, since the difference is only 10^{-4}. Nevertheless, when the side-wall angle differs only by a few tenth of a degree, the value of P_m decreases by orders of magnitude.

As stated previously, the main scope of the *spiral mode detection* is to obtain an increase in the sensitivity of the side-wall angle measurements for values close to $90°$. For this reason, an interesting case would be if one considers a side-wall angle of $89°$, due to the extreme difficulty in the determination of the slope value in this case. If the detection system is designed to detect the intensity differences of the $m = +1$ and/or $m = -1$ orders coming from the fork grating, it should be

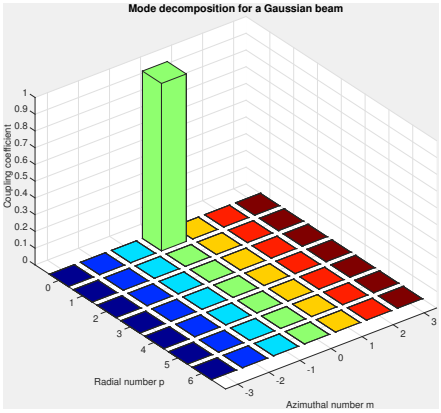

Figure 3.7: Spiral mode expansion of a purely Gaussian beam corresponding to $LG_{0,0}$.

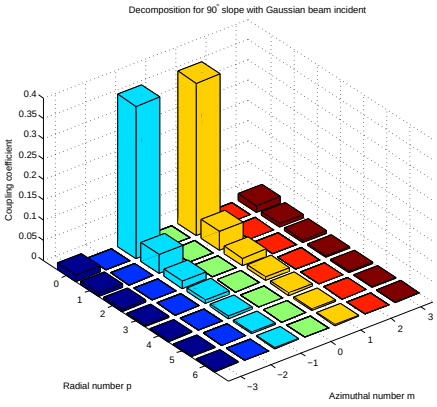

Figure 3.8: Spiral mode expansion for a Gaussian beam after the interaction with a perfect $90°$ cliff.

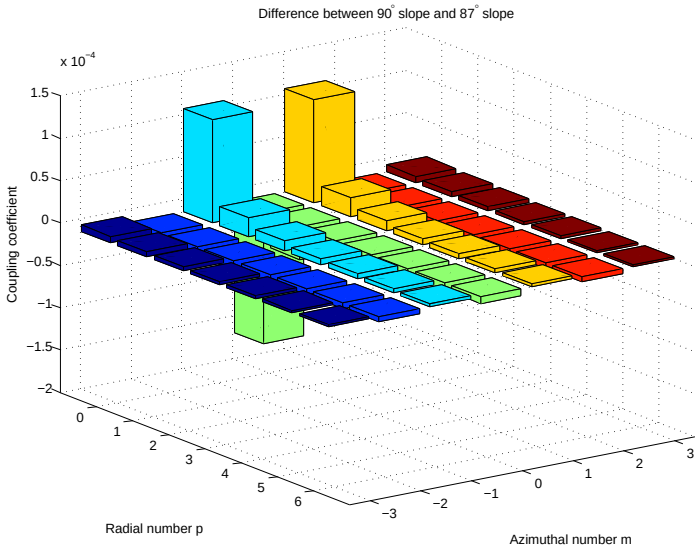

Figure 3.9: Energy content difference between the spiral mode expansion of a Gaussian beam scattered by a perfect $90°$ cliff and a $87°$ slope.

possible, according to Fig. 3.10, to distinguish an angle difference of $1°$.

3.3.2. $LG_{0,1}$ beam incidence

It is worth trying other types of illumination, to verify whether this could bring any benefit, or not, to the side-wall angle detection. Particularly, we studied two different beams, namely the $LG_{0,1}$ and $LG_{1,1}$ modes. As we expected, different modes are now excited, as can be seen in Fig. 3.11 when the SWA is $89°$. Nevertheless, even though other modes are now present in the decomposition, Figure 3.12 shows that the Gaussian beam is still a better candidate to detected small angle variations since in the present case the coupling coefficient is an order of magnitude smaller than in the case of $LG_{0,0}$ illumination.

3.3.3. $LG_{1,1}$ beam incidence

In this section we consider an input Laguerre-Gaussian beam with a radial number $p = 1$ and topological charge $m = 1$. A π phase shift across its center will excite the spiral modes with $m = -1$ and $m = +1$, but they are now centered on $p = +1$ instead of $p = 0$. The difference between the spiral expansion of a $LG_{1,1}$ which interacts with a perfect step, and the expansion of the same beam after interacting with a cliff with $89°$ slope, brings us the result depicted in Figure 3.13. Again, this is not as good as what is presented in figure 3.10, where the maximum of the coupling coefficient is approximately $1 \cdot 10^{-5}$.

We have demonstrated, throughout Section 3.3, that by means of the mode

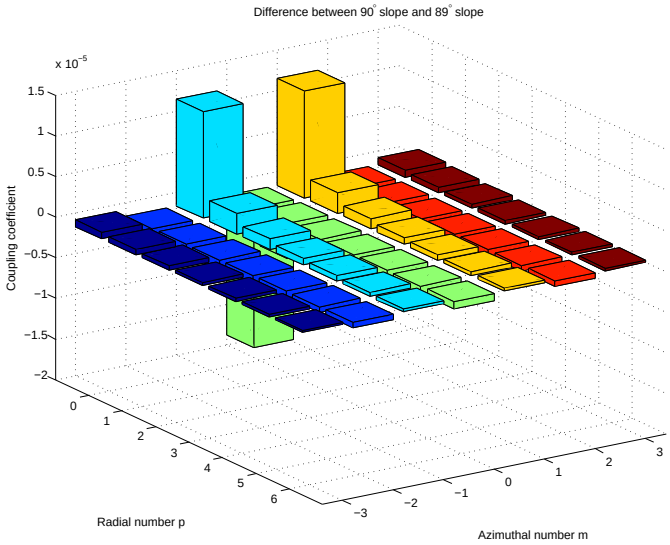

Figure 3.10: Energy content difference between the spiral mode expansion of a Gaussian beam scattered by a perfect $90°$ cliff and a $89°$ slope.

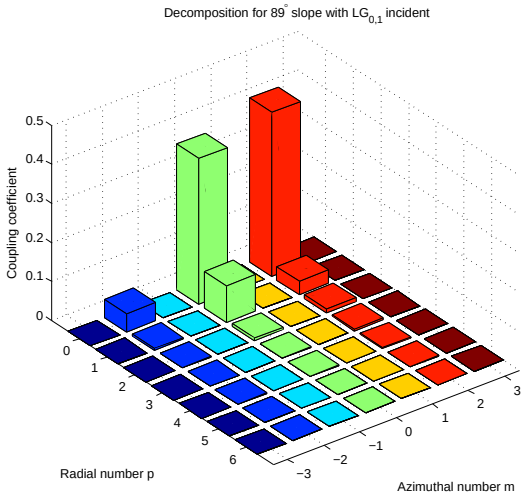

Figure 3.11: Spiral mode expansion of a $LG_{0,1}$ beam after the interaction with a cliff characterized by a SWA of $89°$.

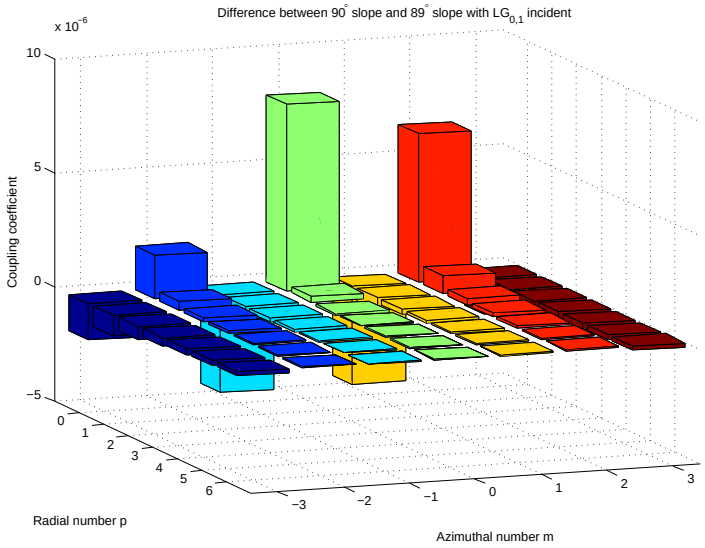

Figure 3.12: Energy content difference between the spiral mode expansion of a $LG_{0,1}$ beam scattered by a perfect $90°$ cliff and a $89°$ slope.

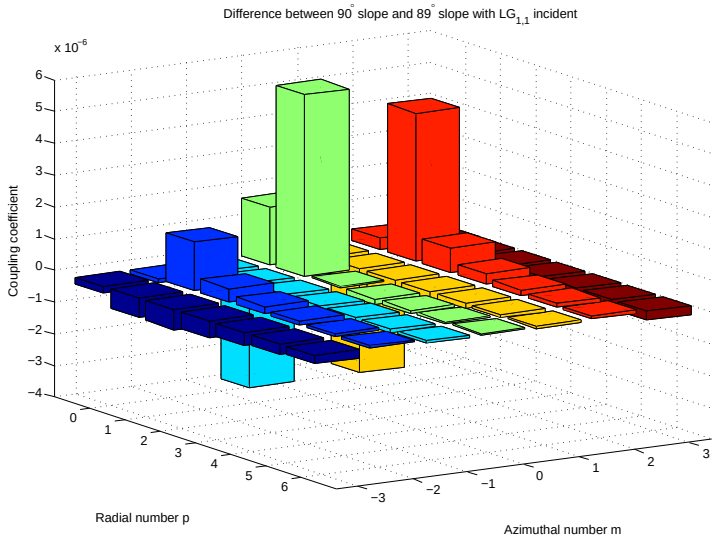

Figure 3.13: Spiral mode expansion of a $LG_{1,1}$ beam after the interaction with a cliff characterized by a SWA of $90°$.

expansion technique we can be sensitive to very small side-wall angle variations, up to one degree. We have seen that any beam can be expanded in terms of spiral modes and hence the energy content of each mode before and after the interaction with a scattering object can be estimated. Furthermore, we have seen that illuminating the object under study with different type of beams leads to different expansions. Among the different illumination modes that have been tested, the Gaussian beam is the best choice for high sensitivity to the side-wall angle change.

3.4. Simulation

In Section 3.3 we have seen how a field can be expanded into LG modes and how three different modes interact with a cliff-like object characterized by a certain side-wall angle α. We have determined that, in this specific case, an input beam with a Gaussian profile is the most suitable choice. Thus in this section we focus mainly on the interaction between a Gaussian field and a phase step object. In this circumstance, the height of the sample is designed to give a phase shift of π in transmission. We then detect the $m = 0$ mode of the beam scattered by the sample. Ideally, the target will be made of a substrate, on top of which we deposit a layer of a desired material that covers part of the sample; its height will be chosen accordingly to the phase change we want to imprint in the incoming beam. Nonetheless, fabrication processes always give a trade-off with the designed parameters we hope to achieve. As a result, the coated layer will not present a sharp and abrupt profile, but rather a smoother contour with round edges and an unknown side-wall angle. This behavior can be taken into account theoretically by modeling the target with Eq. (3.34). Based on this equation and the behavior we just described, the transmission function of the target can be defined with the following equation:

$$T(r,\theta,x_0) := \begin{cases} \beta \, \exp\left[ik\phi_t(x)\right], & \text{if} \quad r\,\cos(\theta) > x_0 \\ 1, & \text{if} \quad r\,\cos(\theta) \leqslant x_0, \end{cases} \tag{3.38}$$

where β is the modulus of the transmittance of the object and x_0 corresponds to the position of the edge of the sample. We immediately notice that, to get a phase shift of π in transmission, the optical path difference between the portion of the beam that goes through the step and its surroundings should be $\lambda/2$, with λ being the wavelength in air. In the case where the input Gaussian beam is represented by the function $LG_{0,0}(r,\theta)$, the beam that exits the target is given by $U(r,\theta,x_0) = LG_{0,0}(r,\theta)T(r,\theta,x_0)$. Subsequently, using Eqs. (3.32) and (3.33), we can compute the spiral mode expansion. In particular, the expression for the radial dependence is:

$$a_m(r) = \frac{1}{\sqrt{2\pi}} \int_0^{2\pi} LG_{0,0}(r,\theta)\,T(r,\theta,x_0)\,\exp\left(-im\theta\right) d\theta \,. \tag{3.39}$$

This coefficient is then substituted into Eq. (3.37) in order to obtain the energy content carried by the mode m. Fig. 3.15 shows a plot of c_0 (obtained by Eqs. (3.37)) as a function of the sample position with respect to the beam. The beam is scanned orthogonally to the sample and, for every position, the intensity is detected; a sketch

of this procedure is given in Fig. 3.14 for clarification. Fig. 3.15 shows a plot of $|a_0|^2$

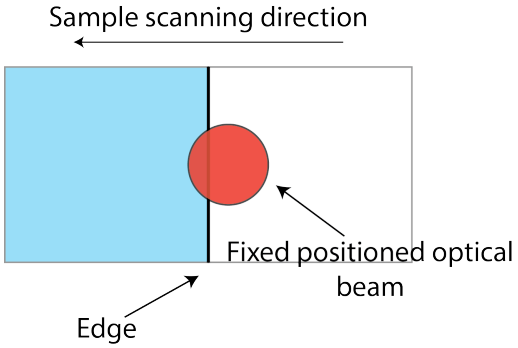

Figure 3.14: Sketch of the scanning procedure performed during data acquisition.

as a function of the sample position. The plotted intensity profile is obtained with the

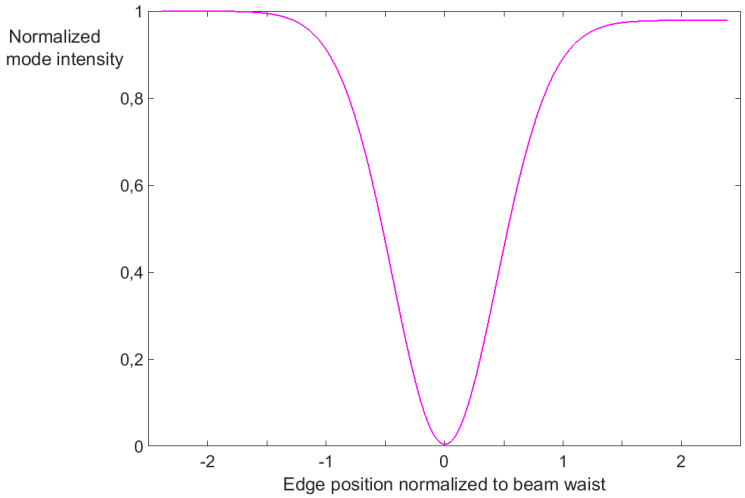

Figure 3.15: Plot of c_0 (given by Eqs. 3.37) as a function of the position of the target with respect to the beam.

following input parameters $\beta = 0.94$, $h = 304\,nm$ and $t = 0.0029 \rightarrow \text{SWA} = 0.16°$. Furthermore, the x-axis is to the waist value. The curve is not symmetric around the center because of the presence of the β coefficient in one of the two sides of the transmission function $T(r, \theta, x_0)$. The model developed in this section will be used as best fit for the experimental data.

3.5. Experiment and discussion

The following step consists in verifying experimentally the numerical results obtained with the simulations. We therefore have built an experimental setup to test

the predictions given by the numerical analysis for the case of a Gaussian input beam. A schematic representation of the optical setup is given in Fig. 3.16. A He-Ne laser illuminates a sample made of a glass substrate with a coated area which covers approximately one half of the total available surface; the material used in this process is silicon nitride (refractive index of 2.01 at $633\,nm$) and the layer thickness is $304\,nm$. The specimen is mounted on a translation stage that allows to scan the sample in a direction perpendicular to the cliff. The sample is optically conjugated to a fiber collimator by means of a $4f$ system (lenses L_1 and L_2), in which either lenses have a focal length of $10\,cm$. Subsequently, a single mode fiber sends the signal to a photodetector that is connected to a low noise current amplifier. The amplifier is needed because of the very low intensity value of the signal when half of the Gaussian input beam experiences a π phase shift. The amplifier is then connected to an oscilloscope (not represented in the figure) to monitor the voltage. The exact position of the conjugated plane between the sample and the fiber col-

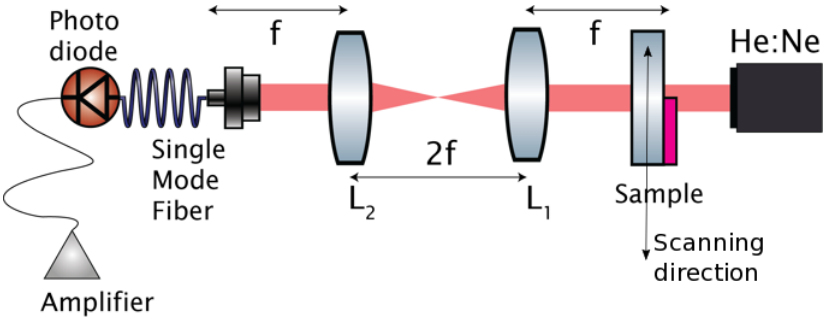

Figure 3.16: Sketch of the experimental setup. The source is a He:Ne laser, which directly illuminares the sample; L_1 and L_2 make a 4-f system with $f = 10\,cm$. A Thorlabs collimator couples the light into a single mode fiber. The fiber is then connected to a photodiode and subsequently to an amplifier that helps to enhance the signal. The sample used is made of a glass substrate with a silicon nitride coating.

limator is crucial; in fact, since the whole detection scheme is based on the phase change that the input beam experiences while interacting with the object, we need to be sure that no extra phase changes are introduced by propagation effects. The profile of the step sample has been also measured independently with a profilometer, and the obtained data has been fit with Eq. (3.34), as it is shown in Fig. 3.17, obtaining the following set of parameters $h = 290\,nm$, $t = 0.0029 \rightarrow \text{SWA} = 0.17°$.

As represented in the sketch of the experimental setup, the beam is coupled to a single mode fiber after the interaction with the sample, and hence we have to project it onto the Gaussian mode of the fiber. We used two identical fiber collimators to shine light onto the target and couple it into the SMF; this allows us to assume that the beam width does not change significantly over the propagation distance and gives us the normalization constant $N = 2/\pi\, w^2$. The detected power is therefore given by:

$$P_F = \left| \frac{2}{w^2 \pi} \int_0^{+\infty} a_0(r)\, r\, dr \right|^2 . \tag{3.40}$$

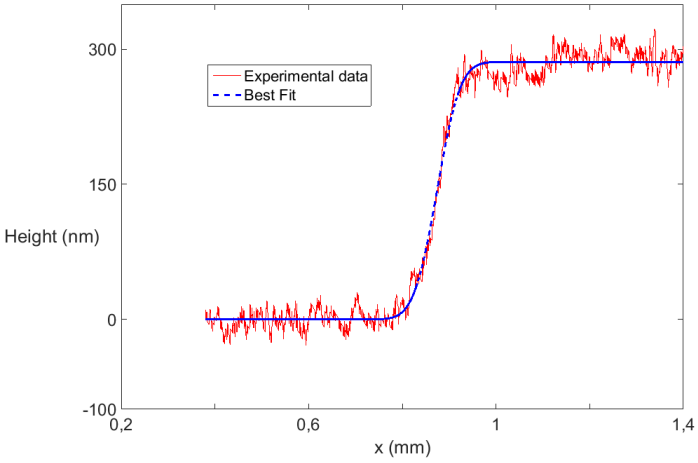

Figure 3.17: Profilometer data and best fit of the target under investigation.

The optimized parameters are obtained by fitting the acquired data with this equation, the parameters starting guess is derived by fitting the profilometer data with the sample model (Eq. 3.34). The accuracy of the best fit is influenced both by the

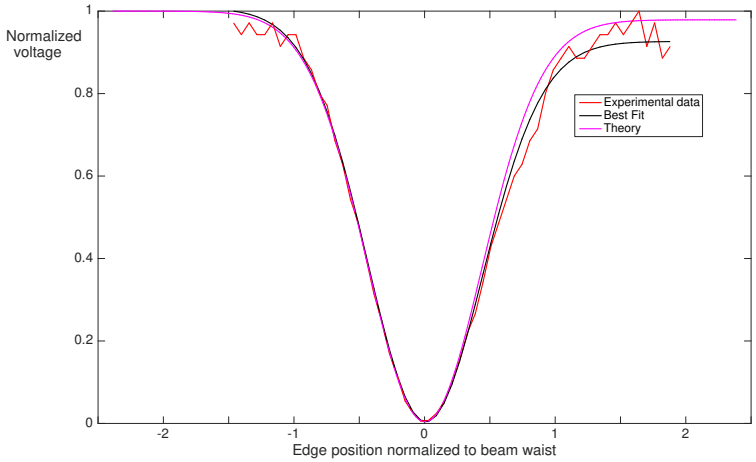

Figure 3.18: Plot of the obtained experimental data and best fit, along with theoretical prediction using the parameters given by the best fit.

experimental data and the profilometer data. The red line in Fig. 3.18 represents the profile obtained by moving the sample in a direction orthogonal to the beam propagation (y direction). As we can see, the edges are the most problematic part; they are characterized by intensity oscillations and, particularly for positive values of the edge position, the behavior does not resemble the best fit. Possible explanations for this discrepancy might be found in the fact that the laser has some intensity

fluctuations. Moreover, the alignment of the optical components is of great importance, especially the coupling of the beam into the single mode fiber. In addition, the sample coated surface was mainly designed to give an overall π phase shift in transition for a large beam illuminating it, not for side-wall angle measurements, therefore irregularities in the coating might be the cause of the different behavior between experiment and theory for positive values of the edge position. Table 3.1 summarizes all the measured and fitted values, i.e. height measurement made with an ellipsometer, height and side-wall angle made with a profilometer. Only the height value obtained from the profilometer fit is very different from the others, nevertheless, looking at Fig. 3.17, we notice that the asymptotic value seems to be close to $300\,nm$. Furthermore, the presence of noise affects the accuracy of the fit.

Table 3.1: Best fit parameters from the profilometer and measured data.

	Profilometer fit	Experimental fit	Ellipsometer
$h\,(nm)$	290 ± 2	308 ± 93	304
SWA (Degree)	0.170 ± 0.007	0.16 ± 0.13	N. A.

3.6. Conclusions

In this chapter we have presented a simple and intuitive experimental setup to measure the side-wall angle of a target, consisting of a phase jump designed to give a π phase shift in transmission. By means of the Spiral Mode expansion we could identify the field which has the greatest sensitivity to the side-wall angle change of a phase object. The Gaussian profile delivers the highest sensitivity to the SWA when $h = \lambda/2$. This is not a limiting factor to this work, as the use of a Spatial Light Modulator could easily restore the designed phase change value in transmission, even when the height of the sample under study is strictly not $h = \lambda/2$. We have theoretically modeled the sample to account for round edges, which are usually formed during fabrication processes, thus implementing a more realistic analysis. For the case of a shallow profile, we were able to determine with good accuracy the value of the side-wall angle by fitting the experimental data with the predictions given by the theoretical model. Successful implementation of this concept for the determination of extremely sharp side-wall angles, might have important and noticeable applications in the field of surface metrology. Furthermore, we would like to emphasize that a properly shaped complex amplitude distribution of the input field could be used in the presence of a different, and perhaps more complex, target. This can be done with the use of a programmable Spatial Light Modulator, which could for example be part of an optimization procedure where the most sensitive input field for a given target profile is employed.
In the next two chapters we will introduce two other ways to infer the side-wall an-

gle of a cliff-like structure; in both cases we follow a purely theoretical approach to compute the scattered far field. In Chapter 4 we aim at increasing the sensitivity towards small SWA changes by implementing a different detection technique, namely a split detection configuration. In Chapter 5 we implement a different strategy: we try to boost the side-wall angle sensitivity by relying on beam shaping techniques. More specifically, by using the Lagrange multipliers rule, we solve an optimization problem to compute the amplitude and phase of the beam interacting with a cliff-like sample to obtain the highest sensitivity to a small side-wall angle change.

References

[1] L. Cisotto, Y. Zhu, S. F. Pereira, and H. P. Urbach, *Spatial mode projection for side-wall angle measurements,* Proc. SPIE **9526**, 952607 (2015).

[2] *International technology roadmap for semiconductors,* (2012), available from http://www.itrs.net/Links/2012ITRS/2012Chapters/2012Overview.pdf.

[3] N. Kumar, P. Petrik, G. K. P. Ramanandan, O. E. Gawhary, S. Roy, S. F. Pereira, W. Coene, and H. P. Urbach, *Reconstruction of sub-wavelength features and nano-positioning of gratings using coherent fourier scatterometry,* Optics Express **22**, 24678 (2014).

[4] Y. Martin and H. K. Wickramasinghe, *Method for imaging sidewalls by atomic force microscopy,* Appl. Phys. Lett. **64**, 2498 (1994).

[5] T. Hu, R. L. Jones, W. li Wu, E. K. Lin, Q. Lin, D. Keane, S. Weigand, and J. Quintana, *Small angle x-ray scattering metrology for sidewall angle and cross section of nanometer scale line gratings,* Appl. Phys. Lett. **96**, 1983 (2004).

[6] B. Su, T. Pan, P. Li, J. Chinn, X. Shi, and M. Dusa, *Sidewall angle measurements using CD SEM,* in *Advanced Semiconductor Manufacturing Conference and Workshop* (IEEE, Boston (MA), 1998) pp. 259–261.

[7] L. Allen, M. J. Padgett, and M. Babiker, *The orbital angular momentum of light,* Progress in Optics **39**, 291 (1999).

[8] M. J. Padgett, J. Courtial, and L. Allen, *Light's orbital angular momentum,* Phys. Today **57**, 35 (2004).

[9] C. Cohen-Tannoudji, J. Dupont-Roc, and G. Grynberg, *Photons and atoms: Introduction to Quantum Electrodynamics* (Wiley, New York, 1989).

[10] S. M. Barnett, *Optical angular-momentum flux,* Journal of Optics B: Quantum and Semiclassical Optics **4**, S7 (2002).

[11] A. T. Neil, I. MacVicar, L. Allen, and M. J. Padgett, *Intrinsic and extrinsic nature of the orbital angular momentum of a light beam,* Phys. Rev. Lett. **88**, 053601 (2002).

[12] K. Dholakia, G. Spalding, and M. MacDonald, *Optical tweezers: the next generation,* Phys. World **15** (2002).

[13] P. Galajda and P.Ormos, *Complex micromachines produced and driven by light,* Appl. Phys. Lett. **78**, 249 (2001).

[14] K. Ladavac and D. G. Grier, *Microoptomechanical pumps assembled and driven by holographic optical vortex arrays,* Opt. Express **12**, 1144 (2004).

[15] R. J. Voogd, M. Singh, S. Pereira, A. van de Nes, and J. Braat, *The use of orbital angular momentum of light beams for super-high density optical data storage,* in *OSA annual meeting* (Rochester, NY, 2004).

[16] L. Torner, J. P. Torres, and S. Carrasco, *Digital spiral imaging,* Opt. Express **13**, 873 (2005).

[17] G. Molina-Terriza, L. Rebane, J. P. Torres, L. Torner, and S. Carrasco, *Probing canonical geometrical objects by digital spiral imaging,* J. Europ. Opt. Soc. Rap. Public. **2**, 07014 (2007).

[18] N. Hermosa, C. Rosales-Guzman, S. F. Pereira, and J. P. Torres, *Nanostep height measurements via spatial mode projection,* Opt. Lett. **39**, 299 (2014).

[19] N. R. Heckenberg, R. McDuff, C. P. Smith, H. Rubinsztein-Dunlop, and M. J. Wegener, *Laser beams with phase singularities,* Optical and Quantum Electronics **24**, S951 (1992).

[20] J. Arlt, K. Dholakia, L. Allen, and M. J. Padgett, *The production of multiringed laguerre-gaussian modes by computer-generated holograms,* Journal of Modern Optics **45**, 1231 (1998), http://dx.doi.org/10.1080/09500349808230913 .

[21] F. Ricci, *Experimental Study Of Phase Singularities in Optical Beams Carrying Orbital Angular Momentum*, Master's thesis, University of Padova, Italy (2012).

[22] S. M. Barnett and L. Allen, *Orbital angular momentum and nonparaxial light beams,* Optics Communications **110**, 670 (1994).

[23] M. Beijersbergen, L. Allen, H. van der Veen, and J. Woerdman, *Astigmatic laser mode converters and transfer of orbital angular momentum,* Optics Communications **96**, 123 (1993).

[24] G. Turnbull, D. Robertson, G. Smith, L. Allen, and M. Padgett, *The generation of free-space laguerre-gaussian modes at millimetre-wave frequencies by use of a spiral phaseplate,* Optics Communications **127**, 183 (1996).

4

Using far field data to determine steep side wall angles: analytical analysis

Nothing in life is to be feared, it is only to be understood.
Now is the time to understand more, so that we may fear less.

Marie Curie

In the previous chapter we have introduced the concept of spiral mode projection as a new possibility to measure the side-wall angle of cliff-like objects. In this chapter, we address the same problem differently. More precisely, we analytically describe the physical problem of the interaction between the structure under study and an incoming focused field. If we restrict ourselves to the scalar optics approximation and we consider an isolated structure described by a cliff or a ridge, the scattering problem description is entirely analytical. This is of great help in understanding how the side-wall angle influences the far field distribution and with what sensitivity we can retrieve the value of this angle.

Parts of this chapter have been published in Journal of Optics **20**, 065601 (2018) [1].

4.1. Introduction

One of the most challenging problems in optical lithography is the metrology of printed structures and features. In order to have electronic circuits that meet the design specification, it is necessary to fabricate appropritate test targets that are employed to tune the lithographic machines. Certain features contained in these targets are directly measured or indirectly retrieved and are used to tune dose, exposure time, alignment and other relevant parameters of the photo-lithographic process [2, 3]. Quantifying the value of the so called side-wall angle with high precision is currently one of the most difficult tasks of this methodology. In the past years, several different techniques such as atomic force microscopy (AFM) and scanning electron microscopy (SEM) have been used. In their standard configuration, these measuring tools have several drawbacks, namely difficulties to measure steep side-walls for AFM and sample damage for electron microscopy. Numerous developments [4–7] have been proposed to improve the performance of these systems, reaching measurements accuracies of the order of 1°. Nonetheless, optical techniques using light are still the preferred choice because of their ease of implementation and measurement speed, along with the important property of being non-destructive. A known technique for this purpose is optical scatterometry [8–12]. Within this technique, the test structure is described by a few shape parameters such as height (h), middle critical dimension (MidCD) and side-wall angle (SWA) that are retrieved by solving an inverse problem using the measured scattered light intensities as data and combining them with a priori knowledge of the system. In order to recover and use the phase information contained in the scattered light, which is lost when using incoherent illumination, Coherent Fourier Scatterometry (CFS) has been introduced, where a focused spot is used to scan the sample [13–15]. This technique uses the extra phase information contained in the overlapping diffracted orders in the far field that are not present in incoherent Fourier scatterometry. As a consequence, CFS has higher sensitivity than traditional incoherent scatterometry, but nevertheless, also for CFS, the SWA remains the most challenging parameter to retrieve. Recently, CFS combined with interferometry has been proposed to determine asymmetries in the side wall angles of a grating [16, 17].

The need for a more accurate (but perhaps also easier to implement) SWA estimation method has been the main driver towards the design of a new technique that could help bridge the gap with the current approaches. In this chapter we present an idea we believe could benefit the SWA estimation problem. More specifically, we conceptualize an experimental setup based on the Scatterometry principle and a split detection configuration. We do not provide neither a real setup nor experimental results, but we treat in depth the theoretical foundation and provide simulation results to prove its validity.

In this chapter we investigate two different structures, described by a cliff- and a ridge-like shape, and determine their side-wall angles. The interaction between the incoming light and the sample will cause phase and amplitude changes in the far field which can be detected using a split detection scheme. When the side-wall angle is very steep, it is quite challenging to estimate its value as the far field for

a side-wall angle of $88°$ and the one for an angle of $89°$, for instance, differ only slightly. With the implementation of a split detection scheme we aim at detecting more easily these differences.

Specifically, we theoretically calculate the electric field - under the approximation of scalar diffraction theory - that is reflected from a cliff or a ridge-like structure having steep side wall angles, when the structure is illuminated by a focused field. The choice of scalar diffraction theory is helpful in keeping the entire derivation analytical without impacting considerably the accuracy of the results. For instance, we are able to detect, in the case of a ridge-like sample, asymmetries between the left and right angles. The purely analytical derivation of the scattered field allows us to have a fast and reliable method to analyze the physical problem. Furthermore, we assume that the structure acts as a phase object. Similarly with what has been done by Hermosa and coworkers [18], we start our analysis in the quadrature configuration condition; this implies that the height of the sample should be such that the condition $h = \lambda/4$ is satisfied, which means that, in reflection, the light undergoes a π phase shift. Afterwards, the case for other heights is also treated.

The chapter is organized as follows. In Section 4.2 we state the definition of the problem and introduce the reflection functions describing the split- and ridge-like shape structure. Sections 4.3 and 4.4 are dedicated to the theoretical derivation of the far-field intensity pattern resulting from the interaction between a focused beam and the phase objects we are considering. Section 4.5 contains the conclusions.

4.2. Problem definition

We begin by considering a cliff shape structure, which is fully characterized by a SWA α and height h, centered in a (x, y, z) reference system as shown in Fig. 4.1. The structure is invariant with respect to the y-coordinate and the slope is given by the function $g_\alpha(x)$ defined as:

$$z = g_\alpha(x) := \begin{cases} 0, & \text{if} \quad x \leqslant -b \\ x \tan\alpha + \frac{h}{2}, & \text{if} \quad -b < x < +b \\ h, & \text{if} \quad x \geqslant +b \end{cases} . \tag{4.1}$$

It should be noted that the structure extends infinitely along the x axis as x goes to $\pm\infty$. This assumption was made to simplify the mathematical derivation, since considering a finite object would add an additional parameter to the derivation.

Throughout the mathematical derivation, we will use α and h as variables to describe the cliff. Its projection b on the horizontal axis can be directly obtained from the formula:

$$b = \frac{h}{2\tan\alpha} \qquad \text{where} \quad 0 < \alpha < \frac{\pi}{2}. \tag{4.2}$$

In varying the slope, the height h will be kept constant. This implies that b changes with α as shown in Eq. (4.2). The structure given by the function $g_\alpha(x)$ represents

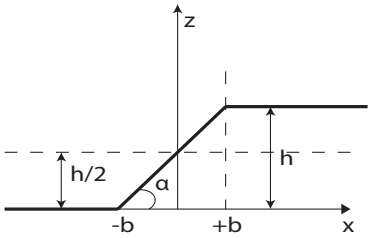

Figure 4.1: Sketch of a cliff-like object.

a pure phase object. Hence its reflection function becomes:

$$r_{\alpha}^{C}(x) = r\begin{cases}\exp(2ikh), & \text{if} \quad x \leqslant -b \\ \exp\left[2ik\left(\frac{h}{2} - x\tan\alpha\right)\right], & \text{if} \quad -b < x < +b \\ 1, & \text{if} \quad x \geqslant +b\end{cases}, \tag{4.3}$$

where $k = 2\pi/\lambda$ is the wave number and r is the reflection coefficient of the surface. This coefficient can be a complex number with $|r| \leq 1$ but we shall subsequently simply take $r = 1$. The superscript "C" indicates that the reflection function describes a cliff.

We also analyze a second structure, described by a ridge-like shape. In this case, besides the height h, we differentiate between two possible side-wall angles, describing the left and right walls of the ridge, which we label as α_L and α_R. As we did in the case of the cliff, we center the structure in a (x, y, z) reference system as shown in Fig. 4.2, and once gain the structure is invariant with respect to the y-coordinate.

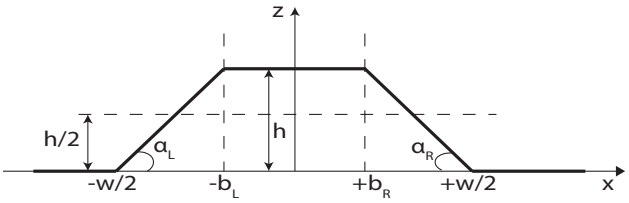

Figure 4.2: Sketch of a cliff-like object.

Within this system, the reflection function of the ridge becomes:

$$r_{\alpha_L,\alpha_R}^{R}(x) = r\begin{cases}\exp(2ikh), & \text{if} \quad x \leqslant -w/2 \\ \exp\{ik\,[2h - (2x + w)\tan\alpha_L]\}, & \text{if} \quad -w/2 < x < -b_L \\ 1, & \text{if} \quad -b_L \leqslant x \leqslant +b_R \\ \exp\{ik\,[2h + (2x - w)\tan\alpha_R]\}, & \text{if} \quad +b_R < x < +w/2 \\ \exp(2ikh), & \text{if} \quad x \geqslant +w/2\end{cases}, \tag{4.4}$$

where, as in the case of the cliff, $k = 2\pi/\lambda$ is the wave number and r is the reflection

coefficient of the surface. The superscript "R" indicates that the reflection function describes a ridge.

4.3. Analytical calculation

Our aim is to calculate analytically the scattered far field generated by the two structures examined in this work, whose reflection functions are given by Eqs. (4.3) and (4.4)[1]. We do this by considering a 4-f system configuration defined by two cylindrical lenses with radius a and focal length f. Mathematically both of them can be represented by the window function $1_{[-a,+a]}(x)$. In the scalar theory, the focal distribution of a plane wave focused by a diffraction limited cylindrical lens is:

$$U^i(x) = \sqrt{\frac{1}{\lambda f}}\, e^{ik2f}\, 2a\, \mathrm{sinc}\left(\frac{2ax}{\lambda f}\right), \tag{4.5}$$

where we define:

$$\mathrm{sinc}(\chi) := \begin{cases} \frac{\sin(\pi\chi)}{\pi\chi} & \text{if} \quad \chi \neq 0 \\ 1, & \text{if} \quad \chi = 0 \end{cases}. \tag{4.6}$$

Within the approximations of physical optics, the interaction between the focused field U^i and the cliff can be represented by multiplying the incoming field $U^i(x)$ by the reflection function r_α^C of the cliff :

$$U_\alpha^r(x) = U^i(x)\, r_\alpha^C(x) \tag{4.7}$$

The scattered field in the exit pupil of the lens is given by:

$$U_\alpha^{\mathrm{out}}(\xi) = \sqrt{\frac{1}{\lambda f}}\, e^{ik2f} \int_{-\infty}^{+\infty} U^i(x)\, r_\alpha^C(x)\, e^{-2\pi i \frac{\xi}{\lambda f} x}\, dx \tag{4.8}$$

where ξ is the coordinate in the exit pupil.

It is worth pointing out that in Eq. (4.8), the structure is considered to be at a fixed location. Nevertheless, from an experimental point of view, it is important to know how the far field signal changes as the sample is scanned parallel to the x-direction in Figs. 4.1 and 4.2. In the following subsection, we explicitly state the expression of $U_\alpha^{\mathrm{out}}(\xi)$ for a positive translation d, i.e. for $x > 0$. The case of negative translation and the calculation of $U_\alpha^{\mathrm{out}}(\xi)$ for the ridge case can be obtained with similar derivations to the ones listed in Appendix B.

4.3.1. Positive translation

Let us consider a positive translation d with the assumption that $-b+d = -(b-d) < 0$. If we substitute the expressions of the reflection function $r_\alpha^C(x-d)$ and the input focal field $U^i(x)$ into Eq. (4.8), we have to consider the following integrals:

$$U_1^{\mathrm{out}}(\xi) = \frac{2a}{\lambda f}\, e^{2ik(2f+h)} \int_{-\infty}^{-b+d} \frac{\sin(kax/f)}{kax/f}\, e^{-ik\frac{\xi}{f}x}\, dx, \tag{4.9}$$

[1] A comparison of our results with the rigorous vectorial theory is given in Appendix C.

$$U^{\text{out}}_{\alpha,2}(\xi) = \frac{2a}{\lambda f}\, e^{ik(4f+h+2d\tan\alpha)} \int_{-b+d}^{b+d} \frac{\sin(kax/f)}{kax/f}\, e^{-i\frac{k}{f}x(2f\tan\alpha+\xi)}\, dx, \tag{4.10}$$

$$U^{\text{out}}_{3}(\xi) = \frac{2a}{\lambda f}\, e^{ik4f} \int_{b+d}^{+\infty} \frac{\sin(kax/f)}{kax/f}\, e^{-ik\frac{\xi}{f}x}\, dx. \tag{4.11}$$

by using the results from Eqs. (B.9), (B.11), (B.14) and (B.15), we have:

$$U^{\text{out}}_{1}(\xi) = \frac{e^{2ik(2f+h)}}{\lambda k}\Bigg\{\pi + i\,\text{Ci}\left[c\frac{k}{f}(a+\xi)\right] - i\,\text{Ci}\left[c\frac{k}{f}(a-\xi)\right] - \text{Si}\left[c\frac{k}{f}(a+\xi)\right] - \text{Si}\left[c\frac{k}{f}(a-\xi)\right]\Bigg\}, \tag{4.12}$$

where we defined $c = b-d$ for a more compact notation. We remind the reader that d is an arbitrary translation in the positive x direction and that b can be obtained from Eq. (4.2).

The solution of Eq. (4.11) is given by:

$$U^{\text{out}}_{3}(\xi) = \frac{e^{4ikf}}{\lambda k}\Bigg\{\pi + i\,\text{Ci}\left[c'\frac{k}{f}(a-\xi)\right] - i\,\text{Ci}\left[c'\frac{k}{f}(a+\xi)\right] - \text{Si}\left[c'\frac{k}{f}(a+\xi)\right] - \text{Si}\left[c'\frac{k}{f}(a-\xi)\right]\Bigg\}, \tag{4.13}$$

where $c' = b+d$. To calculate $U^{\text{out}}_{\alpha,2}(\xi)$ we need to sum the integrals (B.5) and (B.10) reported in Appendix B, with integration intervals $\Omega = x : -b+d < x < 0$ and $\Omega' = \{x : 0 < x < b+d\}$. We remind that in this case we have chosen d such that $-b+d<0$. Finally, for $U^{\text{out}}_{\alpha,2}(\xi)$ we have:

$$\begin{aligned} U^{\text{out}}_{\alpha,2}(\xi) = \frac{e^{ik(4f+h+2d\tan\alpha)}}{\lambda k}\Bigg\{ & - i\,\text{Ci}\left[c'\frac{k}{f}(a-\xi')\right] + i\,\text{Ci}\left[c'\frac{k}{f}(a+\xi')\right] \\ & + \text{Si}\left[c'\frac{k}{f}(a+\xi')\right] + \text{Si}\left[c'\frac{k}{f}(a-\xi')\right] \\ & - i\,\text{Ci}\left[c\frac{k}{f}(a+\xi')\right] + i\,\text{Ci}\left[c\frac{k}{f}(a-\xi')\right] \\ & + \text{Si}\left[c\frac{k}{f}(a+\xi')\right] + \text{Si}\left[c\frac{k}{f}(a-\xi')\right]\Bigg\}. \end{aligned} \tag{4.14}$$

where $\xi' = 2f\tan\alpha + \xi$. The total scattered field in the exit pupil is the sum of these three contributions:

$$U^{\text{out}}_{\alpha}(\xi) = U^{\text{out}}_{1}(\xi) + U^{\text{out}}_{\alpha,2}(\xi) + U^{\text{out}}_{3}(\xi). \tag{4.15}$$

4.3.2. Ridge case

The calculation of the full scattered field for the ridge case is very similar to the one of the slope; we substitute the expressions of the reflection function $r^{R}_{\alpha_L,\alpha_R}(x-d)$

and the input focal field $U^i(x)$ into Eq. (4.8), where we assume that the translation d is such that $-b_L + d < 0$. The calculation can be split into five different integrals that can be computed analytically.

$$U_1^{\text{out},R}(\xi) = \frac{2a}{\lambda f}\, e^{2ik(2f+h)} \int_{-\infty}^{-w/2+d} \frac{\sin(kax/f)}{kax/f}\, e^{-ik\frac{\xi}{f}x}\, dx, \tag{4.16}$$

$$U_{\alpha_L,2}^{\text{out,R}}(\xi) = \frac{2a}{\lambda f}\, e^{ik[4f+2h-(w-2d)\tan\alpha_L]} \int_{-w/2+d}^{-b_L+d} \frac{\sin(kax/f)}{kax/f}\, e^{-i\frac{k}{f}x(\xi+2f\tan\alpha_L)}\, dx, \tag{4.17}$$

$$U_3^{\text{out},R}(\xi) = \frac{2a}{\lambda f}\, e^{ik4f} \int_{-b_L+d}^{+b_R+d} \frac{\sin(kax/f)}{kax/f}\, e^{-ik\frac{\xi}{f}x}\, dx, \tag{4.18}$$

$$U_{\alpha_R,4}^{\text{out,R}}(\xi) = \frac{2a}{\lambda f}\, e^{ik[4f+2h-(w+2d)\tan\alpha_R]} \int_{+b_R+d}^{+w/2+d} \frac{\sin(kax/f)}{kax/f}\, e^{-i\frac{k}{f}x(\xi-2f\tan\alpha_R)}\, dx, \tag{4.19}$$

$$U_5^{\text{out},R}(\xi) = \frac{2a}{\lambda f}\, e^{2ik(2f+h)} \int_{+w/2+d}^{+\infty} \frac{\sin(kax/f)}{kax/f}\, e^{-ik\frac{\xi}{f}x}\, dx, \tag{4.20}$$

where the superscript R indicates that the expressions are for a ridge-like shaped structure. By means of the calculations shown in Appendix B, we get:

$$U_1^{\text{out},R}(\xi) = \frac{e^{2ik(2f+h)}}{\lambda k}\left\{\pi + i\,\text{Ci}\left[c_1\frac{k}{f}(a+\xi)\right] - i\,\text{Ci}\left[c_1\frac{k}{f}(a-\xi)\right] - \text{Si}\left[c_1\frac{k}{f}(a+\xi)\right] - \text{Si}\left[c_1\frac{k}{f}(a-\xi)\right]\right\}, \tag{4.21}$$

with $c_1 = w/2 - d$.

$$\begin{aligned} U_{\alpha_L,2}^{\text{out,R}}(\xi) = \frac{e^{ik[4f+2h-(w-2d)\tan\alpha_L]}}{\lambda k}\Bigg\{ & - i\,\text{Ci}\left[c_2\frac{k}{f}(a-\xi_L)\right] + i\,\text{Ci}\left[c_2\frac{k}{f}(a+\xi_L)\right] \\ & - \text{Si}\left[c_2\frac{k}{f}(a+\xi_L)\right] - \text{Si}\left[c_2\frac{k}{f}(a-\xi_L)\right] \\ & - i\,\text{Ci}\left[c_1\frac{k}{f}(a+\xi_L)\right] + i\,\text{Ci}\left[c_1\frac{k}{f}(a-\xi_L)\right] \\ & + \text{Si}\left[c_1\frac{k}{f}(a+\xi_L)\right] + \text{Si}\left[c_1\frac{k}{f}(a-\xi_L)\right]\Bigg\}, \end{aligned} \tag{4.22}$$

where $\xi_L = 2f\tan\alpha_L + \xi$ and $c_2 = b_L - d$.

$$U_3^{\text{out},R}(\xi) = \frac{e^{4ikf}}{\lambda k}\Big\{ - i\,\text{Ci}\left[c_3\frac{k}{f}(a-\xi)\right] + i\,\text{Ci}\left[c_3\frac{k}{f}(a+\xi)\right] + \text{Si}\left[c_3\frac{k}{f}(a+\xi)\right] + \text{Si}\left[c_3\frac{k}{f}(a-\xi)\right] - i\,\text{Ci}\left[c_2\frac{k}{f}(a+\xi)\right] + i\,\text{Ci}\left[c_2\frac{k}{f}(a-\xi)\right] + \text{Si}\left[c_2\frac{k}{f}(a+\xi)\right] + \text{Si}\left[c_2\frac{k}{f}(a-\xi)\right]\Big\}, \tag{4.23}$$

where $c_3 = b_R + d$.

$$U_{\alpha_R,4}^{\text{out,R}}(\xi) = \frac{e^{ik[4f+2h-(w+2d)\tan\alpha_R]}}{\lambda k}\Big\{ - i\,\text{Ci}\left[c_4\frac{k}{f}(a-\xi_R)\right] + i\,\text{Ci}\left[c_4\frac{k}{f}(a+\xi_R)\right] + \text{Si}\left[c_4\frac{k}{f}(a+\xi_R)\right] + \text{Si}\left[c_4\frac{k}{f}(a-\xi_R)\right] - i\,\text{Ci}\left[c_3\frac{k}{f}(a+\xi_R)\right] + i\,\text{Ci}\left[c_3\frac{k}{f}(a-\xi_R)\right] - \text{Si}\left[c_3\frac{k}{f}(a+\xi_R)\right] - \text{Si}\left[c_3\frac{k}{f}(a-\xi_R)\right]\Big\}, \tag{4.24}$$

where $\xi_R = \xi - 2f\tan\alpha_R$ and $c_4 = w/2 + d$.

$$U_5^{\text{out},R}(\xi) = \frac{e^{2ik(2f+h)}}{\lambda k}\Big\{\pi + i\,\text{Ci}\left[c_4\frac{k}{f}(a-\xi)\right] - i\,\text{Ci}\left[c_4\frac{k}{f}(a+\xi)\right] - \text{Si}\left[c_4\frac{k}{f}(a+\xi)\right] - \text{Si}\left[c_4\frac{k}{f}(a-\xi)\right]\Big\}, \tag{4.25}$$

The total scattered field in the exit pupil is the sum of the five different contributions:

$$U_\alpha^{\text{out},R}(\xi) = U_1^{\text{out},R}(\xi) + U_{\alpha_L,2}^{\text{out,R}}(\xi) + U_3^{\text{out},R}(\xi) + U_{\alpha_R,4}^{\text{out,R}}(\xi) + U_5^{\text{out},R}(\xi). \tag{4.26}$$

4.3.3. Split detection calculation

When the side-wall angle becomes very steep, the sensitivity associated with it decreases because the spot size is much larger than the interval on the x-axis in which the coordinate z changes from 0 to h. Thus the structure appears as a sudden jump. We introduce a split detector configuration to monitor the far field of the sample under study. More specifically, we divide the far field intensity distribution $I_\alpha^{\text{out}}(\xi) = \left|U_\alpha^{\text{out}}(\xi)\right|^2$ in two parts, a left one for negative values of the coordinate of the exit pupil ξ and a right one for positive values of ξ. Subsequently, we integrate each part and subtract one from the other. We can express this detection scheme mathematically as:

$$G_\alpha = \int_{-a}^{0} I_\alpha^{\text{out}}(\xi)\,d\xi - \int_{0}^{+a} I_\alpha^{\text{out}}(\xi)\,d\xi \tag{4.27}$$

where $a = \mathrm{NA}f$. We expect that the behavior of G_α will be particularly influenced by the side-wall angles, the NA of the system and, in the case of the ridge, also by the width of the structure.

4.4. Simulation results

In this section we present the results obtained from the theoretical analysis described in Section 4.3[2]. All plots are normalized to the total detected power carried by the far field when there is no structure, i.e. the substrate is flat. Nevertheless, depending on whether we plot the scattered intensity given by the absolute square of Eq. (4.15) (Eq. (4.26) in case we are analyzing a ridge), or the split detector signal given by Eq. (4.27), the normalization constant changes. In the former case, the normalization constant $I_0(\xi)$ is given by:

$$I_0(\xi) = \left| \sqrt{\frac{1}{\lambda f}}\, e^{ik2f} \int_{-\infty}^{+\infty} U^i(x)\, e^{-2\pi i \frac{\xi}{\lambda f} x}\, dx \right|^2 = \left| e^{ik4f}\, \mathrm{rect}\left(\frac{\xi}{2a}\right) \right|^2, \tag{4.28}$$

where the rect function is defined as:

$$\mathrm{rect}(\chi) := \begin{cases} 0 & \text{if} \quad |\chi| > \frac{1}{2} \\ \frac{1}{2} & \text{if} \quad |\chi| = \frac{1}{2} \\ 1, & \text{if} \quad |\chi| < \frac{1}{2} \end{cases}. \tag{4.29}$$

In the latter case, i.e., when we deal with a split detector signal, the plotted quantity G_α^{norm} corresponds to the split-detector signal G_α divided by the sum of the intensities of the two halves, i.e. by the total scattered intensity in the pupil:

$$G_\alpha^{\mathrm{norm}} = \frac{G_\alpha}{\int_{-a}^{0} I_\alpha^{\mathrm{out}}(\xi)\, d\xi + \int_{0}^{+a} I_\alpha^{\mathrm{out}}(\xi)\, d\xi} = \frac{\int_{-a}^{0} I_\alpha^{\mathrm{out}}(\xi)\, d\xi - \int_{0}^{+a} I_\alpha^{\mathrm{out}}(\xi)\, d\xi}{\int_{-a}^{0} I_\alpha^{\mathrm{out}}(\xi)\, d\xi + \int_{0}^{+a} I_\alpha^{\mathrm{out}}(\xi)\, d\xi}, \tag{4.30}$$

where $a = \mathrm{NA}f$. Furthermore, all the calculations are performed for $\lambda = 633\, nm$ and we normalize the translation distance of the target by the wavelength λ.

First of all, we study how the on-axis intensity - note that since the lens is cylindrical, this corresponds to a row of pixels in $\xi = 0$ and parallel to the y-axis - changes when the angle of the slope of the cliff reaches values close to $90°$, for a numerical aperture of $\mathrm{NA} \leq 0.6$. For $\mathrm{NA} < 0.6$, the scalar model regime is valid. The height of the structure is kept fixed at $\lambda/4$. This condition is known as the *quadrature condition*, and allows us to have the highest signal contrast. It is important to emphasize that fixing this condition does not limit the generality and importance of our results, as the analytical results of the previous sections are valid for any height.

In Fig. 4.3 we plot the values of $I_\alpha^{\mathrm{out}}(\xi = 0)$ for different SWA in the range $87° \leq \alpha \leq 90°$, for $\mathrm{NA} = 0.4$ and $\mathrm{NA} = 0.6$. Here the normalization constant is $I_0(\xi = 0)$, given by Eq. (4.28). The phase object is a cliff with hright $h = \lambda/4$ which

[2]In Appendix C we compared the results derived in this chapter with rigorous vectorial simulations.

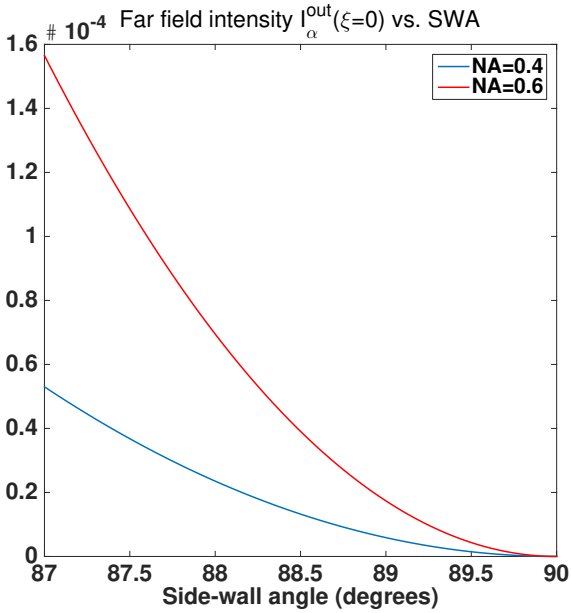

Figure 4.3: On-axis intensity, normalized by $I_0(\xi = 0)$, for a cliff-like object with $h = \lambda/4$ when $87° \leq \mathrm{SWA} \leq 90°$.

is kept fixed symmetrically to the beam propagation axis z, as shown in Fig. 4.1. We notice that the signal decreases quite rapidly when the side-wall angle increases, reaching normalised intensities values of the order of 10^{-5}-10^{-6}, which can still be measured [19, 20]. Note that a smaller focus spot (obtained by a higher NA) will result in higher sensitivity.

Figure 4.4 shows the signal of the on-axis intensity $I_\alpha^{\mathrm{out}}(\xi = 0)$, normalized by $I_0(\xi = 0)$ (Eq. 4.28), for $\mathrm{NA} = 0.6$ in the case of slope with height $h = \lambda/4$ and side-wall angle $\mathrm{SWA} = 80°$, when the sample is moved from negative to positive translation values with respect to the center of the reference system (x, z) shown in Fig. 4.1. The intensity oscillations are caused by the profile of the focus spot that is probing the structure, Eq. (4.5). When the structure is in the central position, the right and left halves of the beam have a phase difference close to π which results, in the far field, in a beam profile similar to that of an Hermite-Gaussian function. It is important to emphasize that the center of the far field intensity of such profile is zero only when the SWA is exactly $90°$ for the case of the quadrature condition. Moreover, for large translation values, both positive and negative, the intensity profile slowly approaches 1, as expected. In fact, given that the structure under study is simply a phase object, when the incident spot is very far off center it will not be influenced by the presence of the structure, thus the scattered field will resemble the one obtained by a flat layer. Hence, because we are normalizing the results by the power of the scattered field in the absence of the structure, we expect the ratio to approach one when the sample is shifted by several wavelengths

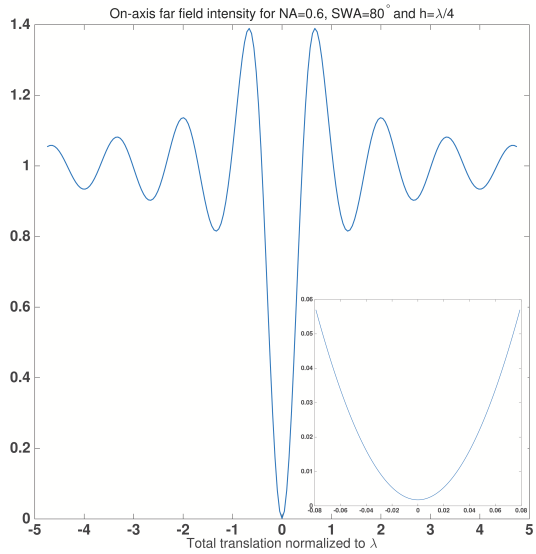

Figure 4.4: On-axis far-field intensity $I_\alpha^{\text{out}}(\xi = 0)$, normalized by $I_0(\xi = 0)$, for a cliff sample with $h = \lambda/4$ and $\text{SWA} = 80°$ translated with respect to the beam for the case of numerical aperture 0.6. Inset: zoomed plot for $d \simeq 0$. Note that because the SWA is not 90 degrees, the signal does not go to zero.

with respect to the focused beam.

In Fig. 4.5 we plot the split detector signal G_α^{norm} given by Eq. (4.30), when a cliff structure of height $h = \lambda/4$ and side-wall angle $\text{SWA} = 87°$ is translated. We remind that this signal has been obtained by calculating the full far field intensity (taking into account a finite numerical aperture of $\text{NA} = 0.6$), integrating the left and right halves of the profile and subtracting them, according to Eq. (4.27), and then dividing this difference by the sum of the intensities of the two halves, i.e. by the total scattered intensity in the pupil. The profile of the signal can be explained by considering the way the sample and the incoming light interact. Suppose the structure moves from negative to positive values of x. The reflected spot is first a sinc function but, when the sample is close enough to influence the reflected beam, part of the latter has a π phase shift, therefore its shape (in the far field region) starts to resemble an Hermite-Gaussian function with one half having bigger magnitude than the other. Subsequently, when the sample is centered, both halves have almost the same magnitude (they are identical only when $\text{SWA} = 90°$) therefore their difference is quite close to zero. When the sample moves away from the beam, the whole process is repeated with the exception that the magnitude of the two halves is inverted and their difference has now an opposite sign compared to the previous scenario. The x-coordinate of the extrema in the split-detector signal gets closer to zero for tighter spots, as intuitively expected. Moreover, when the structure is not close to the beam, the split detector signal tends to zero.

Figure 4.6 shows the difference between normalized split detector signals G_α^{norm}

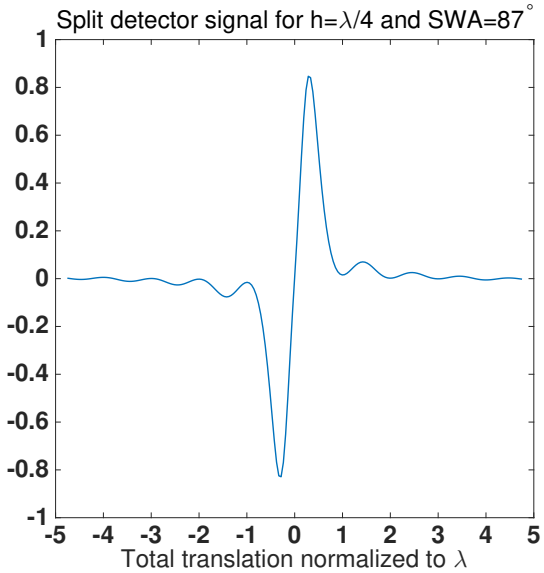

Figure 4.5: Split detector signal G_α^{norm} for a cliff-like object with $h = \lambda/4$ and $\mathrm{SWA} = 87°$ for a numerical aperture of 0.6.

for two cliff-like structures with height $h = \lambda/4$ but characterized by different angles, more precisely $\mathrm{SWA} = 87°$ and $\mathrm{SWA} = 89°$, when the $\mathrm{NA} = 0.6$. The biggest difference is close to $x = 0$, since for $\mathrm{SWA} = 87°$ the focused spot is still sensitive to the slope but when $\mathrm{SWA} = 89°$ it is perceived as a sudden jump from 0 to h.

Figure 4.7 shows the on-axis far-field intensity profile $I_\alpha^{\mathrm{out}}(\xi)$, normalized by $I_0(\xi)$ (Eq. 4.28), for a ridge sample with $\mathrm{SWA}_L = \mathrm{SWA}_R = 80°$, width $w = 2\,\mu m$ and height $h = \lambda/4$ when $\mathrm{NA} = 0.6$. The trend of the signal is changed as compared to Fig. 4.4, but some features are similar. In particular, when the width of the ridge is large compared to the spot size, the spot perceives each slope almost independently from the other, thus the profile of the on-axis far-field intensity signal resembles more the one in Fig. 4.4. Conversely, when the width is comparable to the spot size, the focused field will be influenced by both slopes at once, therefore the profile will approach the one of Fig. 4.5.

In Fig. 4.8 we plot the split detector signal G_α^{norm} given by Eq. (4.30), for the case of a ridge with a width $w = 2\,\mu m$ (defined at the bottom of the ridge, i.e. when $z = 0$), height $h = \lambda/4$ and with identical left and right side-wall angles and equal to $87°$. The profile of the split detector signal has now changed considerably compared to the cliff case. When the structured is centered, the detected signal is close to zero as the spot is simply reflected from the surface at $y = h$. Moreover, when $\mathrm{SWA}_L = \mathrm{SWA}_R$ the sample is completely symmetric with respect to the y-axis and therefore the difference between the left and right half should be zero. Furthermore, the signal presents two full positive/negative oscillations, since two side-wall angles are scanned.

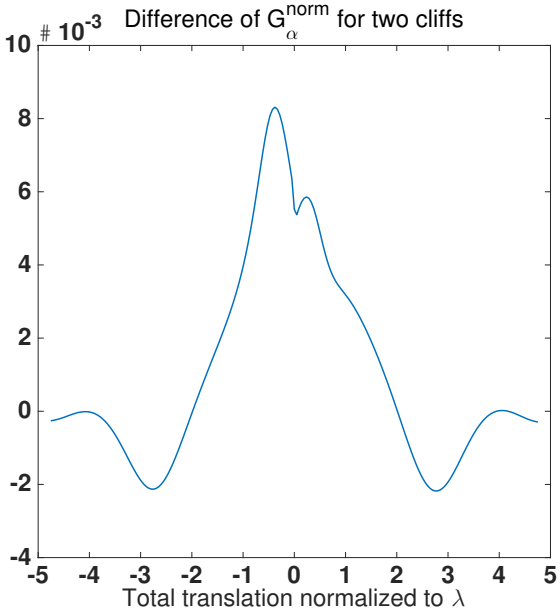

Figure 4.6: Difference between normalized split-detector signals G_α^{norm} generated by two cliff structures with $h = \lambda/4$, $\mathrm{SWA} = 87°$ and $\mathrm{SWA} = 89°$ respectively, for a numerical aperture of 0.6.

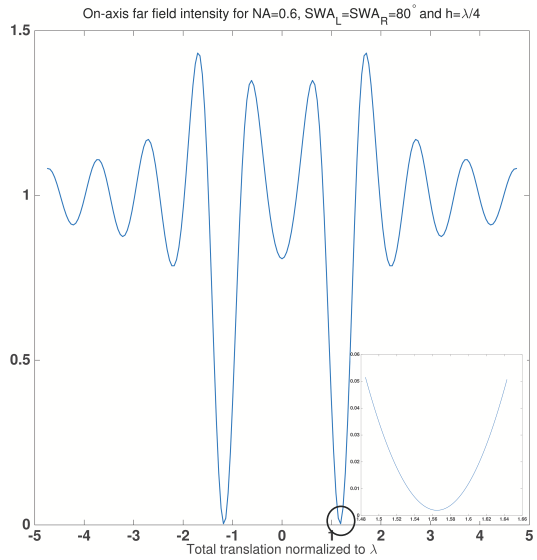

Figure 4.7: On-axis intensity $I_\alpha^{\mathrm{out}}(\xi)$, normalized by $I_0(\xi)$ (Eq. 4.28), for a ridge-like sample with $\mathrm{SWA}_L = \mathrm{SWA}_R = 80°$, width $\mathrm{w} = 2\mu m$ and a numerical aperture of 0.6. Inset: zoomed plot for $d \simeq 0$. Note that because the SWA is not 90 degrees, the signal does not go to zero.

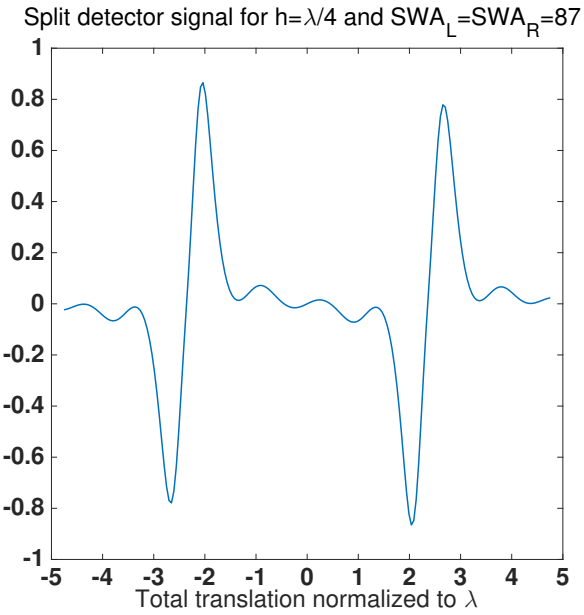

Figure 4.8: Split detector signal G_α^{norm} of a ridge with width $\text{w} = 2\mu m$, height $h = \lambda/4$ and identical left and right side wall angles of $87°$. The numerical aperture is 0.6.

Figure 4.9 shows the difference in split detector signal for two ridge-like samples characterized by a width of $\text{w} = 2\mu m$ and a height height $h = \lambda/4$ with different side-wall angles between them. One is characterized by $\text{SWA}_L = \text{SWA}_R = 89°$ and the other one by $\text{SWA}_L = \text{SWA}_R = 87°$. The largest difference appears, as expected, in the location of the two edges.

In the case of a cliff structure, the simulated profiles plotted so far are not symmetric with respect to the y-axis. More precisely, when the shape parameters of the structure under study differ from, for instance, $\alpha = 90°$ and $h = \lambda/4$, the maximum and minimum values of the split detector signal G_α^{norm} are not symmetric. It is then convenient to define a visibility $\mathcal{V}$ given by:

$$\mathcal{V} = \frac{|\max(G_\alpha^{\text{norm}})| - |\min(G_\alpha^{\text{norm}})|}{|\max(G_\alpha^{\text{norm}})| + |\min(G_\alpha^{\text{norm}})|}, \tag{4.31}$$

where $\max(\cdot)$ and $\min(\cdot)$ represent the global maximum and minimum of the signal G_α^{norm}, thus making the visibility $\mathcal{V}$ a scalar-valued quantity for a given SWA α and height h of the slope. This is nothing but the "contrast" of the extrema values. Particularly, Fig. 4.10 shows a plot of $\mathcal{V}$ for a cliff as a function of the side-wall angle in the range $70° < \alpha < 90°$ and height in the range $148\,nm < h < 168\,nm$. It is clear that both the height and side-wall angle of the sample have a strong influence in the profile of the differential signal. If the height is known with good accuracy (determined for example using other known methods such as profilometry), then the small difference in the visibility will reveal the side wall angle with

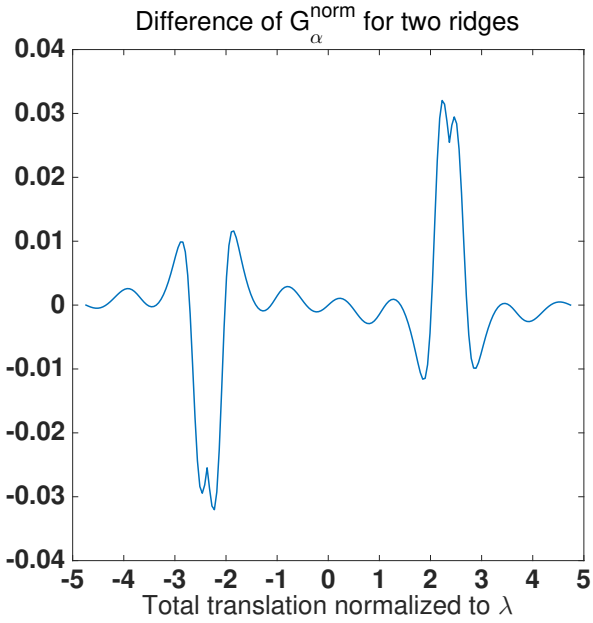

Figure 4.9: Difference in the normalized split detector signals G_α^{norm} from two ridge structures: one with $\mathrm{SWA}_L = \mathrm{SWA}_R = 87°$ and and the other with $\mathrm{SWA}_L = \mathrm{SWA}_R = 89°$ when both are characterized by a width of $\mathrm{w} = 2\mu m$ and a height $h = \lambda/4$. The numerical aperture is 0.6.

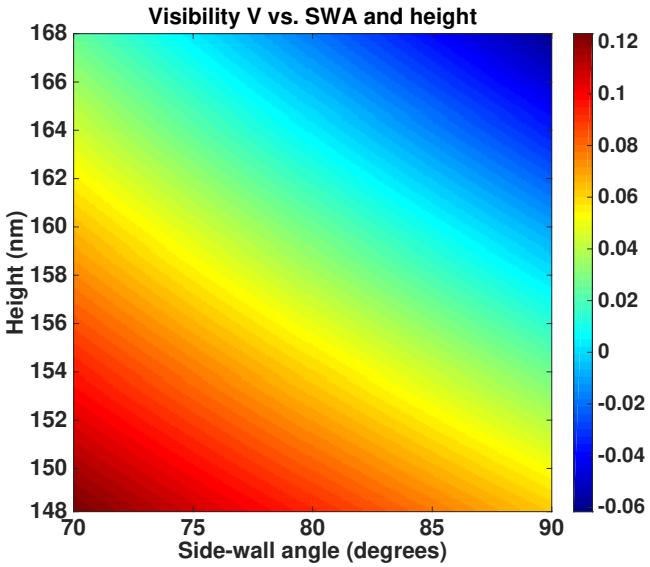

Figure 4.10: Plot of the visibility $\mathcal{V}$ as a function of the side-wall angle α and height h of the slope. The numerical aperture is $\mathrm{NA} = 0.6$.

precision. The height of the cliff or ridge structure can be determined, for example, using other known methods such as atomic force microscopy (AFM), which reaches measurements sensitivity up to a couple of nanometers. Figure 4.10 shows that there are many curves along which the values of the visibility are comparable. As a consequence, it is impossible to uniquely determine both height and SWA from these plots. This is also confirmed by Fig. 4.11, where we plot the contour lines of $\max\left(G_{\alpha}^{\mathrm{norm}}\right)$ (continuous lines) and $|\min\left(G_{\alpha}^{\mathrm{norm}}\right)|$ (dash-dot lines). As one can see, there are multiple points in which the contour lines intersects, making it impossible to unambiguously determine side-wall angle and height. Figure 4.11 also shows that an uncertainty of few nanometers in the height determination will impact the side wall angle estimation by roughly 2°. Nevertheless, if the height of the structure under study is known - for example from independent measurements performed on an atomic force microscope - it is possible to accurately estimate the side-wall angle.

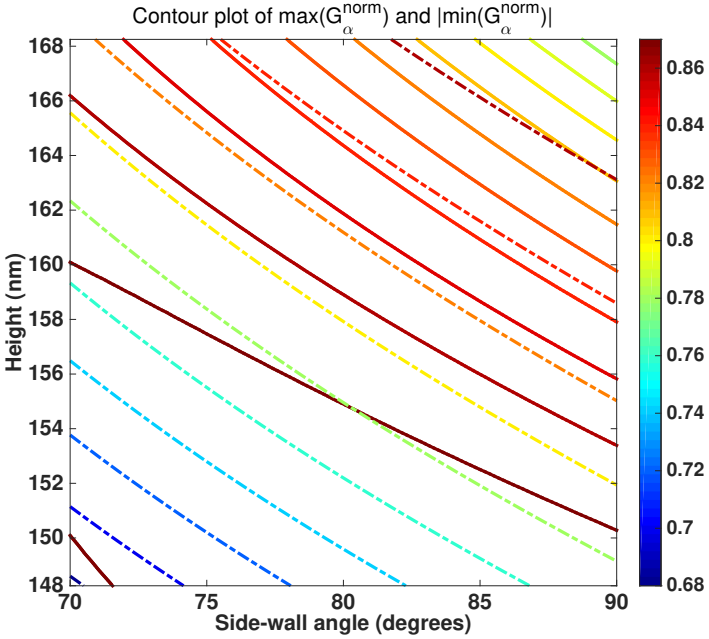

Figure 4.11: Contour plot of $\max\left(G_{\alpha}^{\mathrm{norm}}\right)$ (continuous lines) and $|\min\left(G_{\alpha}^{\mathrm{norm}}\right)|$ (dash-dot lines). Side-wall angle and height cannot be uniquely determined from this plot.

Lastly, we look at how the theoretical model presented in this manuscript can be extended to the case of a ridge characterized by non-identical left and right side wall angles. As we have already mentioned previously, we assume the height of the ridge to have been determined by independent methods such as AFM or SEM.

The possibility to retrieve the values of the side wall angles strictly depends on the relative dimensions between the diameter of the illuminating spot and the width of the ridge. Particularly, as shown in Figure 4.12, we look at how the split

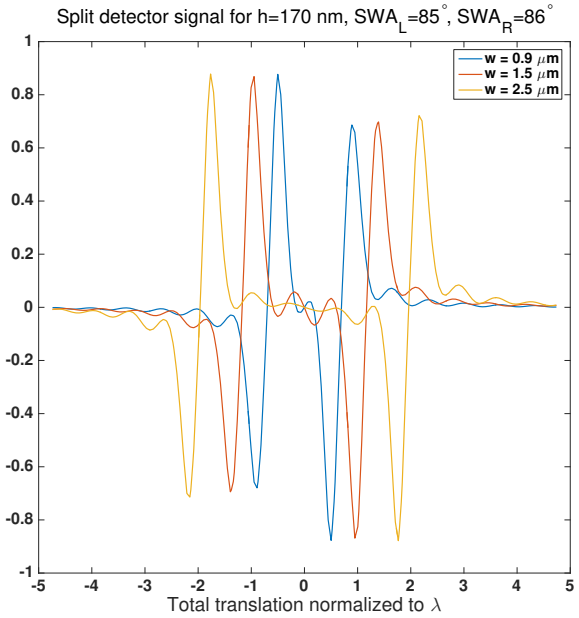

Figure 4.12: Split detector signal $G_{\alpha}^{\mathrm{norm}}$ of a ridge with height $h = 170\,nm$, $\mathrm{SWA}_L = 85°$ and $\mathrm{SWA}_R = 86°$ for different values of width $\mathrm{w} = 0.9\mu m, 1.5\mu m, 2.5\mu m$. The numerical aperture is 0.6.

detector signal $G_{\alpha}^{\mathrm{norm}}$ varies for different ridge width values. More specifically, we consider a ridge with height $h = 170\,nm$, $\mathrm{SWA}_L = 85°$ and $\mathrm{SWA}_R = 86°$ for different values of width $w = 0.9\,\mu m, 1.5\,\mu m, 2.5\,\mu m$. The focusing NA is 0.6, which creates a focused spot with a diameter of roughly $840\,nm$. In the case in which the ridge width is larger than the diameter of the illuminating spot, represented by the case $w = 2.5\,\mu m$ in Figure 4.12, the two side wall angles can be treated as two independent slopes; hence, we can compute the visibility $\mathcal{V}$ using Equation (4.31) for each of the two edges separately and find the respective values of the side-wall angles. Therefore, if the values of the left and right SWA are different, they can still be retrieved with the analytical method presented in this paper. When the ridge width begins to be comparable to the diameter of the illuminating spot, as for the cases $w = 0.9\,\mu m$ and $w = 1.5\,\mu m$ in Figure 4.12, and the left and right SWA are not identical, the visibility plot alone cannot be used to retrieve their values. It is not possible to independently treat the two edges because there will be interaction between their scattered fields. In this case, we believe the theoretical model described and presented in this manuscript can be used to fit the measured signal $G_{\alpha}^{\mathrm{norm}}$ with the values of the two SWAs as free parameters. If, instead, the width is much smaller compared to the diameter of the illuminating spot, the structure cannot be described with the scalar theory, making the model not accurate anymore. In this case, a vectorial treatment of the problem becomes necessary. The detection system can still be based on a split detection configuration, but the SWA reconstruction will be much more elaborated.

4.5. Conclusion

In this chapter we have studied a method to determine the side-wall angle of two distinct structures: a cliff- and a ridge-like shape, modeled as phase objects. This is not a restrictive assumption as our findings can be extended to multilayer geometries as well. If, for instance, the substrates consists of a stack of various flat layers, we can include its complex reflection coefficient in the reflection function. Thus, in Eqs. (4.3) and (4.4), we can consider a value of the complex reflection coefficient r different from 1. Nevertheless, we stress that due to the way the differential detection is defined and implemented, the substrate contribution is eliminated.

We describe mathematically the interaction of these structures with a focused field obtained by a cylindrical lens, under the assumption of scalar theory. We assume the scattered field to be collected by the same lens and we calculate the far-field intensity profile. More precisely, we derive an analytical expression for the scattered field in the exit pupil of a $4f$ configuration. Furthermore, we model a split detection system by dividing the intensity profile in two halves, integrating them and the subtracting one from the other. Our findings show that the proposed method can be a good and sensitive alternative to estimate the side-wall angle and height of the sample. We believe that these structures can constitute an alternative to gratings and other kind of test objects, to tune the lithographic machines and characterize their performance.

References

[1] L. Cisotto, S. F. Pereira, and H. P. Urbach, *Analytical calculation on the determination of steep side wall angles from far field measurements,* Journal of Optics **20**, 065601 (2018).

[2] C. Edwards, A. Arbabi, G. Popescu, and L. L. Goddard, *Optically monitoring and controlling nanoscale topography during semiconductor etching,* Light Sci Appl **1**, e30 (2012).

[3] E. Vogel, *Technology and metrology of new electronic materials and devices,* Nat Nano **2**, 25 (2007).

[4] K. Murayama, S. Gonda, H. Koyanagi, T. Terasawa, and S. Hosaka, *Side-wall measurement using tilt-scanning method in atomic force microscope,* Japanese Journal of Applied Physics **45**, 5423 (2006).

[5] G. Dai, K. Hahm, F. Scholze, M.-A. Henn, H. Gross, J. Fluegge, and H. Bosse, *Measurements of cd and sidewall profile of euv photomask structures using cd-afm and tilting-afm,* Measurement Science and Technology **25**, 044002 (2014).

[6] J. Garnaes, P.-E. Hansen, N. Agersnap, J. Holm, F. Borsetto, and A. Kühle, *Profiles of a high-aspect-ratio grating determined by spectroscopic scatterometry and atomic-force microscopy,* Appl. Opt. **45**, 3201 (2006).

[7] P. R. Bingham, J. R. Price, K. W. Tobin, Jr., T. P. Karnowski, M. H. Bennett, E. H. Bogardus, and M. Bishop, *Sidewall structure estimation from cd-sem for lithographic process control,* in *Process and Materials Characterization and Diagnostics in IC Manufacturing*, Vol. 5041 (2003) pp. 115–126.

[8] A. Faridian, V. F. Paz, K. Frenner, G. Pedrini, A. D. Boef, and W. Osten, *Phase-sensitive structured illumination to detect nanosized asymmetries in silicon trenches,* Journal of Micro/Nanolithography, MEMS, and MOEMS **14**, 021104 (2015).

[9] M. Wurm, F. Pilarski, and B. Bodermann, *A new flexible scatterometer for critical dimension metrology,* Review of Scientific Instruments **81** (2010), http://dx.doi.org/10.1063/1.3280160.

[10] M. Wurm, S. Bonifer, B. Bodermann, and M. Gerhard, *Comparison of far field characterisation of does with a goniometric duv-scatterometer and a ccd-based system,* Journal of the European Optical Society - Rapid publications **6** (2011).

[11] B. Den, A. Bleeker, D. Van, M. Dusa, A. Kiers, P. Luehrmann, H. Pellemans, D. Van, C. Grouwstra, and K. Van, *Method and apparatus for angular-resolved spectroscopic lithography characterisation,* (2006), eP Patent App. EP20,050,254,994.

[12] T. G. Brown, M. A. Alonso, A. Vella, M. J. Theisen, S. T. Head, S. R. Gillmer, and J. D. Ellis, *Focused beam scatterometry for deep subwavelength metrology,* in *Three-Dimensional and Multidimensional Microscopy: Image Acquisition and Processing XXI*, Vol. 8949 (2014) pp. 89490Y–89490Y–7.

[13] O. El Gawhary, N. Kumar, S. F. Pereira, W. M. J. Coene, and H. P. Urbach, *Performance analysis of coherent optical scatterometry,* Applied Physics B **105**, 775 (2011).

[14] N. Kumar, O. el Gawhary, S. Roy, S. F. Pereira, and H. P. Urbach, *Phase retrieval between overlapping orders in coherent fourier scatterometry using scanning,* Journal of the European Optical Society - Rapid publications **8** (2013).

[15] S. Roy, N. Kumar, S. F. Pereira, and H. P. Urbach, *Interferometric coherent fourier scatterometry: a method for obtaining high sensitivity in the optical inverse-grating problem,* Journal of Optics **15**, 075707 (2013).

[16] M. L. Gödecke, S. Peterhänsel, K. Frenner, and W. Osten, *Measurement of asymmetric side wall angles by coherent scanning fourier scatterometry,* (2016) pp. 97780G–97780G–7.

[17] M. L. Gödecke, S. Peterhänsel, K. Frenner, and W. Osten, *Robust determination of asymmetric side wall angles by means of coherent scanning fourier scatterometry,* (2016) pp. 98900M–98900M–8.

[18] N. Hermosa, C. Rosales-Guzmán, S. F. Pereira, and J. P. Torres, *Nanostep height measurement via spatial mode projection,* Opt. Lett. **39**, 299 (2014).

[19] C. W. Freudiger, W. Min, B. G. Saar, S. Lu, G. R. Holtom, C. He, J. C. Tsai, J. X. Kang, and X. S. Xie, *Label-free biomedical imaging with high sensitivity by stimulated raman scattering microscopy,* Science **322**, 1857 (2008), http://science.sciencemag.org/content/322/5909/1857.full.pdf .

[20] B. G. Saar, C. W. Freudiger, J. Reichman, C. M. Stanley, G. R. Holtom, and X. S. Xie, *Video-rate molecular imaging in vivo with stimulated raman scattering,* Science **330**, 1368 (2010), http://science.sciencemag.org/content/330/6009/1368.full.pdf .

5

Side-wall angle detection enhancement through illumination optimisation

The good thing about science is that it's true whether or not you believe in it.

Neil deGrasse Tyson

In the previous chapter we have investigated how a detection system based on a split detection scheme can be used to improve the sensitivity to the SWA. In this chapter, we aim at further improving the sensitivity to a small SWA change, by theoretically calculating the optimum probing beam for a given structure. Using scalar diffraction theory and a cliff-like structure modeled as a phase object, we find the optimum amplitude and phase profile of the input beam which delivers the highest sensitivity to the side-wall angle.

Parts of this chapter have been published in in J. Opt. Soc. Am. A **34**, 1 (2017) [1].

5.1. Introduction

In the previous chapters we have followed a rather simple approach to be able to measure the side-wall angle of a cliff-like object. In this chapter we formulate a purely theoretical description of the same problem to find the most sensitive beam to a small change in the side-wall angle (SWA).

In fact, as we have seen previously, the SWA is a quite elusive parameter and it is rather challenging to measure its value with high precision (for example tenth or hundredth of a degree). In the past years, different techniques, such as atomic force microscopy (AFM) [2–4] and scanning electron microscopy (SEM) [5] have been employed to the study of this problem. These tools are limited by several drawbacks, namely difficulties to measure steep side-walls for AFM and sample damage for electron microscopy. Therefore, optical techniques using light, which are non-destructive and fast, are usually preferred. Optical scatterometry is a known technique for this purpose [6–10] and it has been successfully used in semiconductor industry. The core of this technique is to be able to describe a test structure with a number of shape parameters, such as middle critical dimension (MidCD) and side-wall angle (SWA), that are retrieved by solving an inverse problem using measured scattered light intensities as data, in combination with a priori knowledge of the manufactoring process and the experimental system in use. Recently Coherent Fourier Scatterometry (CFS), in which a coherent focused spot is used to scan the sample, was introduced to use phase information of the scattered light [11–13]. As we seen in Chapter 2, this technique allows us to exploit the phase of the scattered beam, which yields a complete reconstruction of the scattering matrix of the structure under investigation [14]. Because of the possibility to use the whole information carried by the outgoing beam, CFS has higher sensitivity than traditional incoherent scatterometry. But also for CFS, the SWA is the parameter that is most difficult to retrieve.

A possible way to tackle this probem is to properly shape the input beam to maximize its interaction with the structure under study and therefore maximize the sensitivity to small deviation of the side-wall angle from the nominal value. Hence, the topic addressed in this chapter is the optimization of the complex amplitude of the incident spot to maximize the sensitivity of the side-wall detection. In fact, phase and amplitude control of light opens many new applications in the field of optics and it is almost becoming a requirement to be able to fullfill the more and more demanding precision requisites. In astronomy, for example, it is important to modulate light to remove aberrations introduced by very different optical systems such as telescopes or the atmosphere [15, 16]. In biology, particles are studied by trapping them with a properly modulated beam [17–19]. Another innovative application of beam shaping is the focusing of light onto strongly scattering materials [20–22]. Furthermore, recent developments aim at simultaneosly controlling all states of light, namely amplitude, phase and polarization. The increasing adoption and capabilities of Spatial Light Modulators (SLMs) are the main driving force of this branch of optics; in fact, it has been claimed that beams with position dependent amplitude, phase and polarization can be realized with only one SLM [23, 24].

As we have already pointed out earlier, the approach followed in this chapter

differs from the previous one. Rather than solely rely on a detection configuration which can be more sensitive to a SWA change, we concentrate on the illumination properties of the incident light beam on the structure. Therefore, the aim of the work detailed in this chapter is to study the optimization of a focused illumination to maximize the sensitivity of SWA detection in the case of a cliff-like structure, which acts as a phase object. To do so, we consider a cylindrical lens with low numerical aperture (NA) so that scalar diffraction theory can be used to compute the cylindrical focused field and we detect the total reflected intensity. The illumination is optimized such that the change of reflected total intensity, with change of SWA, is maximum. The assumptions made allow a rather straightforward mathematical approach to find the optimum illumination in almost closed form. The optimum solutions are as such of interest but can also be used as initial guess in a more rigorous optimization problem based on Maxwell's equations.

The chapter is organized as follows. In Section 5.2 we formalize the optimization problem used to calculate the optimum field for a given side-wall angle. In Section 5.3 we introduce and formalize a possible solution to the optimization problem in which we compute the total reflected intensity from the structure we are interested in analyzing. This Section is further divided into five subsections where we formalized the optimization problem as a Lagrange multiplier problem (SubSec. 5.3.1), we compute the kernel $\mathcal{K}$ of the integral operator (SubSec. 5.3.2) and we present a mathematical derivation to reach a close formula for the kernel $\mathcal{K}$ in the limit NA $\to 0$ (SubSec. 5.3.3). Subsection 5.3.4 deals with the discretization techniques we employ to solve the optimization problem numerically, whereas subsection 5.3.5 contains the main results provided by the optimization algorithm, which are compared to the case of a plane wave illumination.
In Section 5.4 we propose an alternative method to solve the optimization problem, based on a split detection configuration. We decided to follow the same structure as done for the previous method, to ease the understanding of the two techniques and the similarities/differences of the mathematical derivation. Therefore subsection 5.4.1 introduces the optimization problem as a Lagrange multiplier problem whereas subsection 5.4.3 explains the computation of the kernel $\mathcal{K}$ in the case split detector configuration. In subsection 5.4.4 we explain the retrieval of the side-wall angle using the optimized incident field calculated from the most sensitive method among the two different solutions we have analyzed. Section 5.5 contains the conclusions of the main findings for the two configurations. Mathematical derivations regarding the Fourier transform of the reflection function of the object we considered are presented in Appendix D.

5.2. The optimization problem

The structure we consider is identical to the one that has been detailed out in the preceding chapters. Nevertheless, it is useful to recall its definition and key quantities.

The object under study has a cliff-like shape and it is characterized by a SWA α and height h. We center it in a (x, y, z) reference system as shown in Figure 5.1, such that the structure is invariant with respect to the y-coordinate and the slope

is given by the function $g_\alpha(x)$:

$$z = g_\alpha(x) := \begin{cases} 0, & \text{if} \quad x \leqslant -\frac{a}{2} \\ x\tan(\alpha) + \frac{h}{2}, & \text{if} \quad -\frac{a}{2} < x < \frac{a}{2} \\ h, & \text{if} \quad x \geqslant \frac{a}{2} \end{cases} \tag{5.1}$$

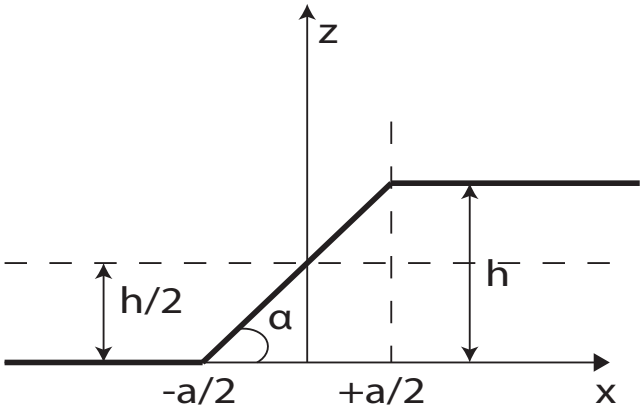

Figure 5.1: The height h and side-wall angle α are the parameters that can vary. The quantity a is automatically derived from the other two variables with Eq. (5.2).

We decided, without loss of generality, to use α and h as variables to describe the cliff. Hence, the projection of the slope over the x axis, namely the horizontal length a, can be directly obtained from the formula:

$$a = \frac{h}{\tan(\alpha)} \qquad 0 < \alpha < \frac{\pi}{2}. \tag{5.2}$$

Furthermore, we will vary the SWA α for a fixed value of h. This implies that a changes with α as shown in Eq. (5.2). We intentionally extended the definition of the structure to $-\infty$ and $+\infty$; this assumption complicates the mathematical derivation, forcing us to invoke distribution theory, but simplifies the problem by removing an additional constraint. The structure given by the function $g_\alpha(x)$ represents a pure phase object, hence the reflection function of the structure becomes:

$$r_\alpha(x) = r\begin{cases} \exp(2ikh), & \text{if} \quad x \leqslant -\frac{a}{2} \\ \exp\left[2ik\left(\frac{h}{2} - x\tan(\alpha)\right)\right], & \text{if} \quad -\frac{a}{2} < x < \frac{a}{2} \\ 1, & \text{if} \quad x \geqslant \frac{a}{2} \end{cases} \tag{5.3}$$

where $k = 2\pi/\lambda$ is the wave number and r is the reflection coefficient of the surface. This coefficient can be a complex number with $|r| \leq 1$ but we shall subsequently simply take $r = 1$.

Let $U^i(x)$ be a cylindrical focused field incident on the sample. The reflected field $U^r_\alpha(x)$, under the assumption of scalar theory, is assumed to be given by:

$$U^r_\alpha(x) = U^i(x)\, r_\alpha(x). \tag{5.4}$$

Suppose that the focused field $U^i(x)$ is generated by a cylindrical microscope objective of numerical aperture NA. With the term "cylindrical microscope", or lens, we mean an objective which is independent of the y-coordinate; such a system transforms a plane wave in a field that is focused along the x-direction, but is independent of the y-coordinate. If we think of an experimental configuration in which the reflected light is collected by the same objective, the total intensity captured by the detector is simply the absolute square of the Fourier transform $\mathcal{F}$ of the reflected field $U^r_\alpha(x)$:

$$I^{\text{out}}_\alpha(\xi) = |\mathcal{F}(U^r_\alpha)(\xi)|^2 = |\mathcal{F}(U^i r_\alpha)(\xi)|^2 \qquad |\xi| \leq \frac{\text{NA}}{\lambda}, \tag{5.5}$$

where ξ is the spatial frequency. We can write:

$$\mathcal{F}(U^i r_\alpha)(\xi) = \left[\mathcal{F}(U^i) * \mathcal{F}(r_\alpha)\right](\xi) = \left[A^i * \mathcal{F}(r_\alpha)\right](\xi), \tag{5.6}$$

where the convolution operation is expressed by the symbol $*$ and, in the last step of Eq. (5.6), we have written $A^i(\xi)$ for $\mathcal{F}(U^i)(\xi)$, i.e. for the complex amplitudes of the expansion of plane waves of the incident field. Throughout the mathematical derivation, $A^i(\xi)$ represents the incident pupil field corresponding to the spatial frequency ξ.

There are several possibilities to optimize the input illumination. One of the most immediate relies on the total detected reflected intensity, more specifically one could maximize the absolute value of the derivative of this quantity as function of the SWA. Mathematically this suggests we have to look for a maximum of the functional:

$$Q(A^i) = \left| \frac{d}{d\alpha} \int_{-\frac{\text{NA}}{\lambda}}^{+\frac{\text{NA}}{\lambda}} \left|A^i * \mathcal{F}(r_\alpha)\right|^2 d\xi \right|. \tag{5.7}$$

Details regarding the theoretical derivation and the results obtained for this configuration are discussed in the Section 5.3. However, it is important to mention at this stage that the total reflected intensity turns out to be not very sensitive to change of SWA, even in the optimized case. Therefore we looked for alternative techniques, and hence functionals, that could enhance the SWA sensitivity even further. As we have seen in Chapter 4, a split detector configuration proves to be a sensitive approach to detect small side-wall angle deviations. This measurement scheme gives much higher maximum sensitivity while it is still very fast, which is important in applications. We hence maximize the change of this difference when the SWA changes. In mathematical terms, we define the functional:

$$\begin{aligned} G(A^i) &= \int_0^{+\frac{\text{NA}}{\lambda}} \frac{d}{d\alpha} I^{\text{out}}_\alpha(\xi)\, d\xi - \int_{-\frac{\text{NA}}{\lambda}}^{0} \frac{d}{d\alpha} I^{\text{out}}_\alpha(\xi)\, d\xi \\ &= \left(\int_0^{+\frac{\text{NA}}{\lambda}} - \int_{-\frac{\text{NA}}{\lambda}}^{0} \right) \frac{d}{d\alpha} |A^i * \mathcal{F}(r_\alpha)|^2\, d\xi \\ &= 2\Re\left(\int_0^{+\frac{\text{NA}}{\lambda}} - \int_{-\frac{\text{NA}}{\lambda}}^{0} \right) A^i * \frac{d\mathcal{F}(r_\alpha)}{d\alpha} \overline{A^i * \mathcal{F}(r_\alpha)}\, d\xi, \end{aligned} \tag{5.8}$$

and try to find the pupil field A^i for which the absolute value $|G(A^i)|$ is maximum under the constraint that the focused power is given (normalized):

$$P(A^i) = \int_{-\frac{\mathrm{NA}}{\lambda}}^{+\frac{\mathrm{NA}}{\lambda}} A^i(\xi)\,\overline{A^i(\xi)}\,d\xi = 1. \tag{5.9}$$

The complex conjugate is indicated with an horizontal bar on top of a mathematical symbol. Note that when the SWA is changed, the function $G(A^i)$ can decrease or increase. It does not matter for our purpose which is the case because we simply want to maximize the change with SWA.

5.3. Total reflected intensity

We begin by considering the functional expressed by Eq. (5.7). As we have already mention in Section 5.2, this is probably the most straightforward choice to begin with. In this section and in the subsections to follow, we present the main mathematical derivation and the results obtained in this configuration. It is important to rewrite Eq. (5.7), as it is the starting point of our derivation:

$$Q(A^i) = \left| \frac{d}{d\alpha} \int_{-\frac{\mathrm{NA}}{\lambda}}^{+\frac{\mathrm{NA}}{\lambda}} \left| A^i * \mathcal{F}(r_\alpha) \right|^2 d\xi \right|, \tag{5.10}$$

where the symbol $*$ expresses the convolution operation. Thus, the convolution between A^i and $\mathcal{F}(r_\alpha)$ can be written as:

$$A^i * \mathcal{F}(r_\alpha)(\xi) = \int_{-\frac{\mathrm{NA}}{\lambda}}^{+\frac{\mathrm{NA}}{\lambda}} A^i(\xi')\,\mathcal{F}(r_\alpha)(\xi - \xi')\,d\xi'. \tag{5.11}$$

Moreover, because the integration region does not depend on the SWA α, we can write:

$$Q(A^i) = \left| \int_{-\frac{\mathrm{NA}}{\lambda}}^{+\frac{\mathrm{NA}}{\lambda}} \frac{d}{d\alpha} |A^i * \mathcal{F}(r_\alpha)|^2(\xi)\,d\xi \right| \tag{5.12a}$$

$$= \left| 2\Re \int_{-\frac{\mathrm{NA}}{\lambda}}^{+\frac{\mathrm{NA}}{\lambda}} \overline{\left(A^i * \frac{d\mathcal{F}(r_\alpha)}{d\alpha} \right)} \left(A^i * \mathcal{F}(r_\alpha) \right) d\xi \right|. \tag{5.12b}$$

We remind the reader that the complex conjugate is indicated with an horizontal bar on top of a mathematical symbol.

5.3.1. The Lagrange mutliplier rule

A useful tool to find a solution to the optimization problem is provided by the Lagrange multiplier rule for inequality constraints [25] (also known as Kuhn-Tucker's theorem). If A^i are the plane wave amplitudes of the optimum incident field, then

according to this theorem there is a Lagrange multiplier Λ such that the following equation is satisfied for all complex B^i:

$$\delta Q(A^i)(B^i) - \Lambda \delta P(A^i)(B^i) = 0 \tag{5.13}$$

where $\delta Q(A^i)(B^i)$ and $\delta P(A^i)(B^i)$ are the Gateaux derivatives of the functionals $Q(A^i)$ and $P(A^i)$ in the direction of B^i. We have:

$$\delta Q(A^i)(B^i) = 2\Re \int_{-\frac{\mathrm{NA}}{\lambda}}^{+\frac{\mathrm{NA}}{\lambda}} \left[A^i * \mathcal{F}(r_\alpha)\, \overline{B^i * \frac{d\mathcal{F}(r_\alpha)}{d\alpha}} + A^i * \frac{d\mathcal{F}(r_\alpha)}{d\alpha}\, \overline{B^i * \mathcal{F}(r_\alpha)} \right] d\xi \tag{5.14}$$

given that we have to compute the real part of the integral in the right hand side of Eq. (5.14), we took the complex conjugate of the second addendum. It is possible to simplify Eq. (5.14) by writing explicitly the convolution terms, hence:

$$\begin{aligned}
\delta Q(A^i)(B^i) &= 2\Re\Bigg\{ \int_{-\frac{\mathrm{NA}}{\lambda}}^{+\frac{\mathrm{NA}}{\lambda}} \left[A^i * \mathcal{F}(r_\alpha)\right](\xi) \int_{-\frac{\mathrm{NA}}{\lambda}}^{+\frac{\mathrm{NA}}{\lambda}} \overline{\frac{d\mathcal{F}(r_\alpha)(\xi-\xi')}{d\alpha}}\, \overline{B^i(\xi')}\, d\xi'\, d\xi \\
&\quad + \int_{-\frac{\mathrm{NA}}{\lambda}}^{+\frac{\mathrm{NA}}{\lambda}} \left[A^i * \frac{d\mathcal{F}(r_\alpha)}{d\alpha} \right](\xi) \int_{-\frac{\mathrm{NA}}{\lambda}}^{+\frac{\mathrm{NA}}{\lambda}} \overline{\mathcal{F}(r_\alpha)(\xi-\xi')}\, \overline{B^i(\xi')}\, d\xi'\, d\xi \Bigg\} \\
&= 2\Re\Bigg\{ \int_{-\frac{\mathrm{NA}}{\lambda}}^{+\frac{\mathrm{NA}}{\lambda}} \Bigg[\int_{-\frac{\mathrm{NA}}{\lambda}}^{+\frac{\mathrm{NA}}{\lambda}} \overline{\frac{d\mathcal{F}(r_\alpha)(\xi'-\xi)}{d\alpha}} \left[A^i * \mathcal{F}(r_\alpha)\right](\xi')\, d\xi' \\
&\quad + \int_{-\frac{\mathrm{NA}}{\lambda}}^{+\frac{\mathrm{NA}}{\lambda}} \overline{\mathcal{F}(r_\alpha)(\xi'-\xi)} \left[A^i * \frac{d\mathcal{F}(r_\alpha)}{d\alpha} \right](\xi')\, d\xi' \Bigg] \overline{B^i(\xi)}\, d\xi \Bigg\} \\
&= 2\Re\Bigg\{ \int_{-\frac{\mathrm{NA}}{\lambda}}^{+\frac{\mathrm{NA}}{\lambda}} \Bigg[\int_{-\frac{\mathrm{NA}}{\lambda}}^{+\frac{\mathrm{NA}}{\lambda}} \overline{\frac{d\mathcal{F}(r_\alpha)(\xi'-\xi)}{d\alpha}} \int_{-\frac{\mathrm{NA}}{\lambda}}^{+\frac{\mathrm{NA}}{\lambda}} A^i(\xi'')\, \mathcal{F}(r_\alpha)(\xi'-\xi'')\, d\xi''\, d\xi' \\
&\quad + \int_{-\frac{\mathrm{NA}}{\lambda}}^{+\frac{\mathrm{NA}}{\lambda}} \overline{\mathcal{F}(r_\alpha)(\xi'-\xi)} \int_{-\frac{\mathrm{NA}}{\lambda}}^{+\frac{\mathrm{NA}}{\lambda}} A^i(\xi'')\, \frac{d\mathcal{F}(r_\alpha)(\xi'-\xi'')}{d\alpha}\, d\xi''\, d\xi' \Bigg] \\
&\quad \cdot \overline{B^i(\xi)}\, d\xi \Bigg\} \\
&= 2\Re\Bigg\{ \int_{-\frac{\mathrm{NA}}{\lambda}}^{+\frac{\mathrm{NA}}{\lambda}} \int_{-\frac{\mathrm{NA}}{\lambda}}^{+\frac{\mathrm{NA}}{\lambda}} \Bigg[\int_{-\frac{\mathrm{NA}}{\lambda}}^{+\frac{\mathrm{NA}}{\lambda}} \overline{\frac{d\mathcal{F}(r_\alpha)(\xi''-\xi)}{d\alpha}}\, \mathcal{F}(r_\alpha)(\xi''-\xi')\, d\xi'' \\
&\quad + \int_{-\frac{\mathrm{NA}}{\lambda}}^{+\frac{\mathrm{NA}}{\lambda}} \overline{\mathcal{F}(r_\alpha)(\xi''-\xi)}\, \frac{d\mathcal{F}(r_\alpha)(\xi''-\xi')}{d\alpha}\, d\xi'' \Bigg] A^i(\xi')\, d\xi'\, \overline{B^i(\xi)}\, d\xi \Bigg\} \\
&= 2\Re \int_{-\frac{\mathrm{NA}}{\lambda}}^{+\frac{\mathrm{NA}}{\lambda}} \int_{-\frac{\mathrm{NA}}{\lambda}}^{+\frac{\mathrm{NA}}{\lambda}} \mathcal{K}(\xi,\xi')\, A^i(\xi')\, d\xi'\, \overline{B^i(\xi)}\, d\xi,
\end{aligned} \tag{5.15}$$

where the kernel $\mathcal{K}$ has been written as the sum of two main contributions in which one is the complex conjugate of the other:

$$\mathcal{K}(\xi,\xi') = \mathcal{H}(\xi,\xi') + \overline{\mathcal{H}(\xi',\xi)}, \tag{5.16}$$

with:

$$\mathcal{H}(\xi,\xi') = \int_{-\frac{\mathrm{NA}}{\lambda}}^{+\frac{\mathrm{NA}}{\lambda}} \overline{\frac{d\mathcal{F}(r_\alpha)(\xi''-\xi)}{d\alpha}}\, \mathcal{F}(r_\alpha)(\xi''-\xi')\, d\xi''. \tag{5.17}$$

The Gateaux derivative of the power P is much easier to calculate and it is given by the following formula:

$$\delta P(A^i)(B^i) = 2\Re \int_{-\frac{\mathrm{NA}}{\lambda}}^{+\frac{\mathrm{NA}}{\lambda}} A^i(\xi)\, \overline{B^i(\xi)}\, d\xi. \tag{5.18}$$

Equation (5.13) can now be written as:

$$2\Re \int_{-\frac{\mathrm{NA}}{\lambda}}^{+\frac{\mathrm{NA}}{\lambda}} \left[\int_{-\frac{\mathrm{NA}}{\lambda}}^{+\frac{\mathrm{NA}}{\lambda}} \mathcal{K}(\xi,\xi')\, A^i(\xi')\, d\xi' - \Lambda A^i(\xi) \right] \overline{B^i(\xi)}\, d\xi = 0 \qquad \forall\, B^i \in \mathbb{C}, \tag{5.19}$$

as we mention at the beginning of this Section, Eq. (5.19) has to be satisfied for all complex B^i, which allows us to write it as an in-homogeneous Fredholm equation of the first kind:

$$\int_{-\frac{\mathrm{NA}}{\lambda}}^{+\frac{\mathrm{NA}}{\lambda}} \mathcal{K}(\xi,\xi')\, A^i(\xi') d\xi' = \Lambda A^i(\xi) \tag{5.20}$$

Note that:

$$\delta Q(A^i)(A^i) = 2Q(A^i), \qquad \delta P(A^i)(A^i) = 2P(A^i) \tag{5.21}$$

thus Eq. (5.13) gives, with $B^i = A^i$ and for a unit power:

$$Q(A^i) = \Lambda. \tag{5.22}$$

We therefore conclude that the solution of our optimization problem is the eigenfunction A^i corresponding to the eigenvalue for which $|\Lambda|$ is maximum.

5.3.2. Computation of the kernel $\mathcal{K}$

As discussed in Section 5.2, we want to find the optimized field which entails the highest sensitivity to the SWA change in the case of a cliff-like geometrical object, that acts as a phase object. Moreover, we found that the optimized field can be obtained by solving an integral equation with kernel $\mathcal{K}$, Eqs. (5.16) and (5.17), that includes the Fourier transform of the reflection function r_α and its derivative with respect to the side-wall angle. In this section, we reach a more explicit form for the kernel $\mathcal{K}$ which will help us to retrieve, under certain assumptions, an analytic solution of Eq. (5.20).

As shown in Appendix D, the Fourier transform of the reflection function defined by Eq. (5.3) is given by the distribution:

$$\mathcal{F}(r_\alpha)(\xi) = \exp(ikh)\left[-\frac{\sin\left(kh+\pi h\frac{\xi}{\tan\alpha}\right)}{\pi}\mathrm{PV}\left(\frac{1}{\xi}\right) + \delta(\xi)\cos(kh) + \frac{\sin\left(kh+\pi h\frac{\xi}{\tan\alpha}\right)}{k\tan\alpha+\pi\xi}\right], \tag{5.23}$$

where $\delta(\xi)$ is the Dirac's delta function and PV indicates the distribution given by the Cauchy Principal Value, i.e. for any smooth test function $\phi(\xi)$ we have:

$$\mathrm{PV}\left(\frac{1}{\xi}\right)\phi(\xi) = \lim_{\epsilon\to 0^+}\int_{\Re\setminus[-\epsilon,+\epsilon]}\frac{\phi(\xi)}{\xi}d\xi \tag{5.24a}$$

$$= \int_0^{+\infty}\frac{\phi(\xi)-\phi(-\xi)}{\xi}d\xi. \tag{5.24b}$$

The δ distribution and the Cauchy Principal Value integral correspond to the specular reflected part of the total reflected field. The specular reflected part is relatively large due to the fact that in our model the structure extends from $-\infty < x < \infty$. The derivative with respect to α of the just calculated Fourier transform is given by:

$$\frac{d\mathcal{F}(r_\alpha)(\xi)}{d\alpha} = \exp(ikh)\left[\frac{kh\cos\left(kh+\pi h\frac{\xi}{\tan\alpha}\right)}{k\sin^2\alpha+\frac{\pi\xi}{2}\sin(2\alpha)} - \frac{k\sin\left(kh+\pi h\frac{\xi}{\tan\alpha}\right)}{k^2\sin^2\alpha+\pi^2\xi^2\cos^2\alpha+k\pi\xi\sin(2\alpha)}\right]. \tag{5.25}$$

Note that both the right-hand sides of Eqs. (5.23) and (5.25) are real except for the factor $\exp(ikh)$ which multiplies all terms, but it can be factor out of the integral in Eq. (5.20) since it does not depend on the variable ξ. Therefore $\mathcal{K}$ is a real valued function. Moreover, from the definition of $\mathcal{K}$ we can infer that $\mathcal{K}(\xi,\xi') = \mathcal{K}(\xi',\xi)$. Thus the integral operator is self-adjoint and therefore there exist an orthogonal basis of $L^2(\mathbb{R})$ of eigenfunctions and all eigenvalues are real.

When calculating a close expression for Eq. (5.17), we need to pay particular attention to the Cauchy Principal value integral in the Fourier transform of the target reflection function. Using the Eqs. (5.23), (5.24b) and (5.25), we can write

Eq. (5.17) as:

$$\begin{aligned}\mathcal{H}(\xi,\xi') = &-\frac{\exp(ikh)}{\pi}\mathrm{PV}\int_{-\frac{\mathrm{NA}}{\lambda}}^{+\frac{\mathrm{NA}}{\lambda}} \frac{\sin\left(kh+\pi h\frac{(\xi''-\xi')}{\tan\alpha}\right)}{\xi''-\xi'}\,\overline{\frac{d\mathcal{F}(r_\alpha)(\xi''-\xi)}{d\alpha}}\,d\xi'' \\ &+\exp(ikh)\,\cos(kh)\int_{-\frac{\mathrm{NA}}{\lambda}}^{+\frac{\mathrm{NA}}{\lambda}}\overline{\frac{d\mathcal{F}(r_\alpha)(\xi''-\xi)}{d\alpha}}\,\delta(\xi''-\xi')\,d\xi'' \\ &+\exp(ikh)\int_{-\frac{\mathrm{NA}}{\lambda}}^{+\frac{\mathrm{NA}}{\lambda}}\overline{\frac{d\mathcal{F}(r_\alpha)(\xi''-\xi)}{d\alpha}}\,\frac{\sin\left(kh+\pi h\frac{(\xi''-\xi')}{\tan\alpha}\right)}{k\tan\alpha+\pi(\xi''-\xi')}\,d\xi'' \\ = &-\frac{\exp(ikh)}{\pi}\mathrm{PV}\int_{-\frac{\mathrm{NA}}{\lambda}}^{+\frac{\mathrm{NA}}{\lambda}} \frac{\sin\left(kh+\pi h\frac{(\xi''-\xi')}{\tan\alpha}\right)}{\xi''-\xi'}\,\overline{\frac{d\mathcal{F}(r_\alpha)(\xi''-\xi)}{d\alpha}}\,d\xi'' \\ &+\exp(ikh)\,\cos(kh)\overline{\frac{d\mathcal{F}(r_\alpha)(\xi'-\xi)}{d\alpha}} \\ &+\exp(ikh)\int_{-\frac{\mathrm{NA}}{\lambda}}^{+\frac{\mathrm{NA}}{\lambda}}\overline{\frac{d\mathcal{F}(r_\alpha)(\xi''-\xi)}{d\alpha}}\,\frac{\sin\left(kh+\pi h\frac{(\xi''-\xi')}{\tan\alpha}\right)}{k\tan\alpha+\pi(\xi''-\xi')}\,d\xi''\end{aligned} \tag{5.26}$$

As mentioned before, the Cauchy Principal Value integral requires particular care. It is therefore convenient to introduce a function $w(\xi'')$ defined as:

$$w(\xi'') := \sin\left[kh+\pi h\frac{(\xi''-\xi')}{\tan\alpha}\right]\overline{\frac{d\mathcal{F}(r_\alpha)(\xi''-\xi)}{d\alpha}} \tag{5.27}$$

The PV integral ca now be written as:

$$
\begin{aligned}
I_{\mathrm{PV}} &= -\frac{\exp(ikh)}{\pi}\mathrm{PV}\int_{-\frac{\mathrm{NA}}{\lambda}}^{+\frac{\mathrm{NA}}{\lambda}} \frac{w(\xi'')}{\xi''-\xi'}d\xi'' \\
&= -\frac{\exp(ikh)}{\pi}\left[\int_{-\frac{\mathrm{NA}}{\lambda}}^{+\frac{\mathrm{NA}}{\lambda}} \frac{w(\xi'')-w(\xi')}{\xi''-\xi'}\,d\xi'' + w(\xi')\mathrm{PV}\int_{-\frac{\mathrm{NA}}{\lambda}}^{+\frac{\mathrm{NA}}{\lambda}} \frac{1}{\xi''-\xi'}\,d\xi''\right] \\
&= -\frac{\exp(ikh)}{\pi}\left[\int_{-\frac{\mathrm{NA}}{\lambda}}^{+\frac{\mathrm{NA}}{\lambda}} \frac{w(\xi'')-w(\xi')}{\xi''-\xi'}\,d\xi''\right. \\
&\qquad \left. + w(\xi')\lim_{\epsilon\to 0}\left(\int_{-\frac{\mathrm{NA}}{\lambda}}^{\xi'-\epsilon} + \int_{\xi'+\epsilon}^{+\frac{\mathrm{NA}}{\lambda}}\right)\frac{1}{\xi''-\xi'}\,d\xi''\right] \\
&= -\frac{\exp(ikh)}{\pi}\left[\int_{-\frac{\mathrm{NA}}{\lambda}}^{+\frac{\mathrm{NA}}{\lambda}} \frac{w(\xi'')-w(\xi')}{\xi''-\xi'}\,d\xi''\right. \\
&\qquad \left. + w(\xi')\lim_{\epsilon\to 0}\left\{\left[\ln|\xi''-\xi'|\right]_{\xi''=-\frac{\mathrm{NA}}{\lambda}}^{\xi''=\xi'-\epsilon} + \left[\ln|\xi''-\xi'|\right]_{\xi''=\xi'+\epsilon}^{\xi''=\frac{\mathrm{NA}}{\lambda}}\right\}\right] \\
&= -\frac{\exp(ikh)}{\pi}\left[\int_{-\frac{\mathrm{NA}}{\lambda}}^{+\frac{\mathrm{NA}}{\lambda}} \frac{w(\xi'')-w(\xi')}{\xi''-\xi'}\,d\xi'' + w(\xi')\ln\left|\frac{\frac{\mathrm{NA}}{\lambda}-\xi'}{\frac{\mathrm{NA}}{\lambda}+\xi'}\right|\right].
\end{aligned}
\tag{5.28}
$$

Note that for $\xi'' = \xi'$:

$$
w(\xi'')\Big|_{\xi''=\xi'} = \sin(kh)\,\overline{\frac{d\mathcal{F}(r_\alpha)(\xi'-\xi)}{d\alpha}}. \tag{5.29}
$$

The final form for the term $\mathcal{H}(\xi,\xi')$ can be written as:

$$
\begin{aligned}
\mathcal{H}(\xi,\xi') = &-\frac{\exp(ikh)}{\pi}\int_{-\frac{\mathrm{NA}}{\lambda}}^{+\frac{\mathrm{NA}}{\lambda}} \frac{w(\xi'')-w(\xi')}{\xi''-\xi'}\,d\xi'' \\
&+ \exp(ikh)\,\cos(kh)\overline{\frac{d\mathcal{F}(r_\alpha)(\xi'-\xi)}{d\alpha}} \\
&- \frac{\exp(ikh)}{\pi}\ln\left|\frac{\frac{\mathrm{NA}}{\lambda}-\xi'}{\frac{\mathrm{NA}}{\lambda}+\xi'}\right|\sin(kh)\,\overline{\frac{d\mathcal{F}(r_\alpha)(\xi'-\xi)}{d\alpha}} \\
&+ \exp(ikh)\int_{-\frac{\mathrm{NA}}{\lambda}}^{+\frac{\mathrm{NA}}{\lambda}} \overline{\frac{d\mathcal{F}(r_\alpha)(\xi''-\xi)}{d\alpha}}\,\frac{\sin\left(kh+\pi h\frac{(\xi''-\xi')}{\tan\alpha}\right)}{k\tan\alpha+\pi(\xi''-\xi')}\,d\xi''.
\end{aligned}
\tag{5.30}
$$

In the next section we will see that, by substituting for Eq. (5.30) into Eqs. (5.17) and thus (5.16), it is possible to calculate an analytic form of the optimum field $A^i(\xi)$ for the limit case $\mathrm{NA}\to 0$.

5.3.3. Limit NA → 0

In this Section we calculate an analytic solution for the optimum field $A^i(\xi)$ by considering the limit case NA $\to 0$. This is important because it constitutes the reference data to verify the computational model we need to build in order to solve Eq. (5.20). In fact, for very small values of the numerical aperture of the system, the computational model needs to converge to the analytic one. The first integrand in the right hand-side of Eq. (5.30) is $\mathcal{O}(|\xi'' - \xi'|) \leq \max|\xi'|, |\xi''|$. Since $|\xi'|, |\xi''| < \frac{\text{NA}}{\lambda}$ the integrand is $\mathcal{O}\left(\frac{\text{NA}}{\lambda}\right)$ and hence the integral is $\mathcal{O}\left(\left(\frac{\text{NA}}{\lambda}\right)^2\right)$. The last term of Eq. (5.30) is instead $\mathcal{O}\left(\frac{\text{NA}}{\lambda}\right)$, therefore the dominant terms of $\mathcal{H}(\xi, \xi')$ are:

$$\mathcal{H}(\xi,\xi') \approx \exp(ikh)\,\cos(kh)\overline{\frac{d\mathcal{F}(r_\alpha)(\xi'-\xi)}{d\alpha}} - \frac{\exp(ikh)}{\pi}\ln\left|\frac{\frac{\text{NA}}{\lambda}-\xi'}{\frac{\text{NA}}{\lambda}+\xi'}\right| \times \sin(kh)\,\overline{\frac{d\mathcal{F}(r_\alpha)(\xi'-\xi)}{d\alpha}} \tag{5.31}$$

Hence the kernel $\mathcal{K}$ can be approximated with the expression:

$$\begin{aligned}\mathcal{K}(\xi,\xi') &= \mathcal{H}(\xi,\xi') + \overline{\mathcal{H}(\xi',\xi)} \\ &\approx \cos(kh)\left[\exp(ikh)\overline{\frac{d\mathcal{F}(r_\alpha)(\xi'-\xi)}{d\alpha}} + \exp(-ikh)\frac{d\mathcal{F}(r_\alpha)(\xi-\xi')}{d\alpha}\right] \\ &\quad - \frac{\exp(ikh)}{\pi}\ln\left|\frac{\frac{\text{NA}}{\lambda}-\xi'}{\frac{\text{NA}}{\lambda}+\xi'}\right|\sin(kh)\,\overline{\frac{d\mathcal{F}(r_\alpha)(\xi'-\xi)}{d\alpha}} \\ &\quad - \frac{\exp(-ikh)}{\pi}\ln\left|\frac{\frac{\text{NA}}{\lambda}-\xi}{\frac{\text{NA}}{\lambda}+\xi}\right|\sin(kh)\,\frac{d\mathcal{F}(r_\alpha)(\xi-\xi')}{d\alpha}.\end{aligned} \tag{5.32}$$

Substituting Eq. (5.32) into the left hand side integral of Eq. (5.20) yields:

$$
\begin{aligned}
I_{\mathcal{K}} &= \int_{-\frac{\mathrm{NA}}{\lambda}}^{+\frac{\mathrm{NA}}{\lambda}} \mathcal{K}(\xi,\xi')\, A^i(\xi')d\xi' \\
&\approx -\frac{\exp(ikh)}{\pi}\sin(kh)\int_{-\frac{\mathrm{NA}}{\lambda}}^{+\frac{\mathrm{NA}}{\lambda}} \ln\left|\frac{\frac{\mathrm{NA}}{\lambda}-\xi'}{\frac{\mathrm{NA}}{\lambda}+\xi'}\right| \overline{\frac{d\mathcal{F}(r_\alpha)(\xi'-\xi)}{d\alpha}}\, A^i(\xi')d\xi' \\
&\quad -\frac{\exp(-ikh)}{\pi}\ln\left|\frac{\frac{\mathrm{NA}}{\lambda}-\xi}{\frac{\mathrm{NA}}{\lambda}+\xi}\right|\sin(kh)\int_{-\frac{\mathrm{NA}}{\lambda}}^{+\frac{\mathrm{NA}}{\lambda}} \frac{d\mathcal{F}(r_\alpha)(\xi-\xi')}{d\alpha}\, A^i(\xi')d\xi' \\
&\quad +\cos(kh)\int_{-\frac{\mathrm{NA}}{\lambda}}^{+\frac{\mathrm{NA}}{\lambda}}\left[\exp(ikh)\overline{\frac{d\mathcal{F}(r_\alpha)(\xi'-\xi)}{d\alpha}}\right. \\
&\quad \left. +\exp(-ikh)\frac{d\mathcal{F}(r_\alpha)(\xi-\xi')}{d\alpha}\right]A^i(\xi')d\xi'
\end{aligned}
\tag{5.33}
$$

At this point, we take the limit $\mathrm{NA}\to 0$:

$$
I_{\mathcal{K}} \approx -\frac{\exp(-ikh)}{\pi}\ln\left|\frac{\frac{\mathrm{NA}}{\lambda}-\xi}{\frac{\mathrm{NA}}{\lambda}+\xi}\right|\sin(kh)\,\frac{2\,\mathrm{NA}}{\lambda}\,\frac{d\mathcal{F}(r_\alpha)(\xi)}{d\alpha}\,A^i(0) \tag{5.34a}
$$

$$
\frac{\exp(ikh)}{\pi}\sin(kh)\int_{-\frac{\mathrm{NA}}{\lambda}}^{+\frac{\mathrm{NA}}{\lambda}}\ln\left|\frac{\frac{\mathrm{NA}}{\lambda}-\xi'}{\frac{\mathrm{NA}}{\lambda}+\xi'}\right|\overline{\frac{d\mathcal{F}(r_\alpha)(-\xi)}{d\alpha}}\,A^i(0)\,d\xi' \tag{5.34b}
$$

$$
+\frac{2\,\mathrm{NA}\cos(kh)}{\lambda}\left[\exp(ikh)\overline{\frac{d\mathcal{F}(r_\alpha)(-\xi)}{d\alpha}}+\exp(-ikh)\frac{d\mathcal{F}(r_\alpha)(\xi)}{d\alpha}\right]A^i(0) \tag{5.34c}
$$

we notice that the integral in Eq. (5.34b) vanishes given that the integrand is an odd function of ξ', the other integrals can instead be evaluated analytically. It is thus possible to write the integral $I_{\mathcal{K}}$ as:

$$
\begin{aligned}
I_{\mathcal{K}} &\approx -\frac{\exp(-ikh)}{\pi}\frac{2\,\mathrm{NA}}{\lambda}\ln\left|\frac{\frac{\mathrm{NA}}{\lambda}-\xi}{\frac{\mathrm{NA}}{\lambda}+\xi}\right|\sin(kh)\,\frac{d\mathcal{F}(r_\alpha)(\xi)}{d\alpha}\,A^i(0) \\
&\quad +\frac{2\,\mathrm{NA}\cos(kh)}{\lambda}\left[\exp(ikh)\overline{\frac{d\mathcal{F}(r_\alpha)(-\xi)}{d\alpha}}+\exp(-ikh)\frac{d\mathcal{F}(r_\alpha)(\xi)}{d\alpha}\right]A^i(0)
\end{aligned}
\tag{5.35}
$$

This result can be substituted into Eq. (5.20) to reach an approximate expression for the Lagrange multiplier problem when $\mathrm{NA} \to 0$:

$$2\frac{\mathrm{NA}}{\lambda}A^i(0)\left\{\cos(kh)\left[\exp(ikh)\overline{\frac{d\mathcal{F}(r_\alpha)(-\xi)}{d\alpha}}+\exp(-ikh)\frac{d\mathcal{F}(r_\alpha)(\xi)}{d\alpha}\right]\right.$$
$$\left.-\frac{\exp(-ikh)}{\pi}\ln\left|\frac{\frac{\mathrm{NA}}{\lambda}-\xi}{\frac{\mathrm{NA}}{\lambda}+\xi}\right|\sin(kh)\frac{d\mathcal{F}(r_\alpha)(\xi)}{d\alpha}\right\}=\Lambda A^i(\xi) \quad (5.36)$$

The eigenvalue Λ of the optimization problem can be analytically computed if we take $\xi = 0$ in Eq. (5.36) and substituting the expression for the derivative with respect to α of the reflection function (Eq. (5.25)):

$$\begin{aligned}\Lambda &= 2\frac{\mathrm{NA}}{\lambda}\cos(kh)\left[\exp(ikh)\overline{\frac{d\mathcal{F}(r_\alpha)(0)}{d\alpha}}+\exp(-ikh)\frac{d\mathcal{F}(r_\alpha)(0)}{d\alpha}\right]\\ &= 4\frac{\mathrm{NA}}{\lambda}\cos(kh)\left[\frac{h\cos(hk)}{\sin^2\alpha}-\frac{\sin(hk)}{k\sin^2\alpha}\right]\\ &= 4\frac{\mathrm{NA}}{\lambda}\frac{hk\cos^2(hk)-\cos(kh)\sin(hk)}{k\sin^2\alpha}\end{aligned} \quad (5.37a)$$

The formula for the eigenvalue Λ can be substituted into Eq. (5.36) to find a close expression of the eigenfunction $A^i(\xi)$:

$$A^i(\xi)=2\frac{\mathrm{NA}}{\lambda}\frac{A^i(0)}{\Lambda}\left\{\cos(kh)\left[\exp(ikh)\overline{\frac{d\mathcal{F}(r_\alpha)(-\xi)}{d\alpha}}+\exp(-ikh)\frac{d\mathcal{F}(r_\alpha)(\xi)}{d\alpha}\right]+\right.$$
$$\left.-\frac{\exp(-ikh)}{\pi}\ln\left|\frac{\frac{\mathrm{NA}}{\lambda}-\xi}{\frac{\mathrm{NA}}{\lambda}+\xi}\right|\sin(kh)\frac{d\mathcal{F}(r_\alpha)(\xi)}{d\alpha}\right\} \quad (5.38)$$

At last, the expression for $A^i(0)$ can be found from the constraint imposed to the total available power:

$$\int_{-\frac{\mathrm{NA}}{\lambda}}^{+\frac{\mathrm{NA}}{\lambda}}|A^i(\xi)|^2\,d\xi=1 \quad (5.39)$$

which gives us:

$$A^i(0)=\frac{\lambda}{2\mathrm{NA}}\frac{\Lambda}{\sqrt{\int_{-\frac{\mathrm{NA}}{\lambda}}^{+\frac{\mathrm{NA}}{\lambda}}\left|T(\xi)\right|^2\,d\xi}} \quad (5.40)$$

where:

$$T(\xi)=\cos(kh)\left[\exp(ikh)\overline{\frac{d\mathcal{F}(r_\alpha)(-\xi)}{d\alpha}}+\exp(-ikh)\frac{d\mathcal{F}(r_\alpha)(\xi)}{d\alpha}\right]$$
$$-\frac{\exp(-ikh)}{\pi}\ln\left|\frac{\frac{\mathrm{NA}}{\lambda}-\xi}{\frac{\mathrm{NA}}{\lambda}+\xi}\right|\sin(kh)\frac{d\mathcal{F}(r_\alpha)(\xi)}{d\alpha} \quad (5.41)$$

NOTE: Looking at the expressions we have just obtained, we notice that in the case NA $\to$ 0, $A^i(\xi)$ is independent of α. The maximum sensitivity that can be achieved for a given α is given by:

$$\Lambda = \frac{\delta Q(A^i)(A^i)}{\delta P(A^i)(A^i)} = \frac{Q(A^i)}{P(A^i)} = Q(A^i) = \max Q(A^i) \tag{5.42}$$

Hence:

$$\max Q(A^i) = \Lambda = 4\,\frac{\mathrm{NA}}{\lambda}\,\frac{hk\cos^2(hk) - \cos(kh)\sin(hk)}{k\sin^2\alpha} \tag{5.43}$$

this implies that the optimum sensitivity is a monotonically decreasing function of the slope angle α.

5.3.4. Discretization

In this subsection we briefly discuss the discretization technique used to compute the kernel $\mathcal{K}$ and Eq. (5.20). This is based on the Nyström method, which means that we will transform the integral equation we need to solve into a matrix eigenvalue equation. Setting $\xi' = \frac{\mathrm{NA}}{\lambda}\xi'' = \beta\xi''$ we get:

$$\beta\int_{-1}^{1}\mathcal{K}(\xi,\beta\xi'')\,A^i(\beta\xi'')d\xi'' = \Lambda A^i(\xi) \tag{5.44}$$

which is still an inhomogeneous Fredholm equation of the first kind, with eigenvalue $\Lambda' = \Lambda/\beta$. Since the integration interval runs from -1 to 1, we can apply the Gaussian quadrature rule; hence we discretize the variable ξ'' into N points $-1 < \xi_1'' < \xi_2'' < \ldots < \xi_N'' = 1$ with Gaussian weight w_i corresponding to ξ_i'' to obtain:

$$\sum_{n=1}^{N} w_n\,\mathcal{K}(\xi,\beta\xi_n'')\,A^i(\beta\xi_n'') = \Lambda'\,A^i(\xi) \tag{5.45}$$

To proceed, we discretize the variable ξ into N points as well, therefore:

$$\sum_{n=1}^{N} w_n\,\mathcal{K}(\xi_m,\beta\xi_n'')\,A^i(\beta\xi_n'') = \Lambda'\,A^i(\xi_m) \qquad m = 1,2,\ldots,N \tag{5.46}$$

The system given by Eq. (5.46) can be written in matrix form by setting $\mathbf{K} = \mathcal{K}(\xi_m,\beta\xi_n'')$, $\mathbf{w} = \mathrm{diag}(w_1,\ldots,w_N)$ and $\mathbf{A^i} = [A^i(\xi_1), A^i(\xi_2),\ldots,A^i(\xi_N)]^T$. Hence we need to solve the matrix eigenvalue problem

$$\mathbf{K}\mathbf{w}\,\mathbf{A^i} = \Lambda'\,\mathbf{A^i} \tag{5.47}$$

which, when solved, yields N eigenvalues Λ_m', $m = 1,2,\ldots,N$, and the associated eigenfunctions A_m^i.

5.3.5. Computation of the optimized field

In this section we look at the behavior of the optimized field $A^i(\xi)$ for some values of the slope angle α, the height h and the numerical aperture NA of the system. Furthermore, we compare the sensitivity of the optimized field with that of a plane wave. In this way we can analyze the performance of a properly shaped beam with the most used and general type of illumination. For the optimum input field, the sensitivity is simply given by the strongest positive (or strongest negative) eigenvalue Λ, whereas for a plane wave illumination we need to calculate the sensitivity $Q(A^i)$ from Eq. (5.8), by substituting for $A^i(\xi)$ the expression of a plane wave. We have:

$$\begin{aligned} Q(A^i_{\text{PW}}) &= \frac{1}{2}\,\delta Q(A^i_{\text{PW}})(A^i_{\text{PW}}) \\ &= |A^i_0|^2 \Re \int_{-\frac{\text{NA}}{\lambda}}^{+\frac{\text{NA}}{\lambda}} \int_{-\frac{\text{NA}}{\lambda}}^{+\frac{\text{NA}}{\lambda}} \mathcal{K}(\xi,\xi')\,d\xi\,d\xi' \end{aligned} \tag{5.48}$$

5

where A^i_0 represents the amplitude of the plane wave. Hence, it is possible to calculate the sensitivity of the plane wave case by simply integrating the kernel $\mathcal{K}(\xi,\xi')$. The amplitude A^i_0 of the plane wave has to be normalized to 1 using Eq. (5.9), which gives $|A^i_0|^2 = \lambda/(2\,\text{NA})$. All the plots we present have been obtained by considering the input illumination in the visible part of the spectrum ($\lambda = 633nm$).

Figure 5.2 shows the profiles of the optimized input field as a function of the coordinate ξ (normalized to 1), for $\alpha = 22°, 44°, 66°, 88°$, $h = \lambda/3$ and $\text{NA} = 0.3$. As we already pointed out in Section 5.3.2, the kernel $\mathcal{K}(\xi,\xi')$ of the eigenvalue equation we need to solve is real valued and symmetric, therefore the eigenfunctions are real valued and the phase of the optimized beam is thus 0 or π. The profile of the eigenvector $A^i(\xi)$ differs strongly from a plane wave illumination, with most of the energy concentrated into the high order components. In Figure 5.3 the optimum solution is plotted for $\alpha = 85°$, $h = \lambda/5$ and $\text{NA} = 0.01, 0.1, 0.5$. In this case, changing the numerical aperture of the system does not influence much the profile of the solution.

In Figure 5.4, we plot the ratio between the sensitivity corresponding to the optimum field and the one related to a plane wave illumination is plotted against the variation of the slope angle $13° \leq \alpha \leq 89°$, for $\text{NA} = 0.4$ and $h = \lambda/3$. In this configuration, using the optimized solution provides only a small gain compared to the more standard plane wave incidence.

It is important to point out that it is critical to find both the strongest positive and most negative eigenvalues of the system; in fact, we are interested in calculating the input field which gives the steepest change in the reflected intensity. Hence its value could also diminish, thus the eigenvector associated to the strongest minimum could also be an acceptable solution of our system. This hypothesis is confirmed by Figure 5.5. Without any loss of generality, we chose to plot the values of the minimum and maximum eigenvalues for $\text{NA} = 0.3$ and $h = \lambda/5$, in this case we observe that the best solution is actually given by the strongest minimum eigenvalue. Therefore it is important to calculate and find both solutions.

Figure 5.6 compares the calculated value of the optimum field obtained from the numerical calculations with the analytic formula given by Eq. (5.38). For small values of the numerical aperture of the system, i.e. NA $\to 0$, the eigenvalue of the optimum solution is given by Eq. (5.38), and the sensitivity for the plane wave case can be computed by taking the limit NA $\to 0$ in Eq. (5.48). We have:

$$\begin{aligned} Q(A^i_{\text{PW}}) &= |A^i_0|^2 \Re \int_{-\frac{\text{NA}}{\lambda}}^{+\frac{\text{NA}}{\lambda}} \int_{-\frac{\text{NA}}{\lambda}}^{+\frac{\text{NA}}{\lambda}} \mathcal{K}(\xi, \xi')\, d\xi\, d\xi' \\ &= \frac{\lambda}{2\text{NA}} 4 \left(\frac{\text{NA}}{\lambda}\right)^2 \mathcal{K}(0,0) \\ &= 4\frac{\text{NA}}{\lambda} \frac{hk\cos(hk) - \sin(hk)}{k\sin^2\alpha} \cos(kh) \end{aligned} \tag{5.49}$$

that is exactly the same expression reported in Eq. (5.43) and, as we can notice, the output of the two methods agrees perfectly.

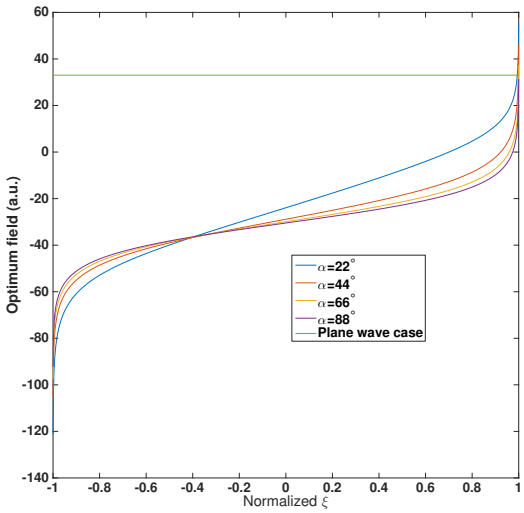

Figure 5.2: Plot of the optimum field A^i as a function of ξ for different side-wall angles. The numerical aperture NA $= 0.3$ and height $h = \lambda/3$ of the cliff are fixed. The optimum field changes when the slope angle changes.

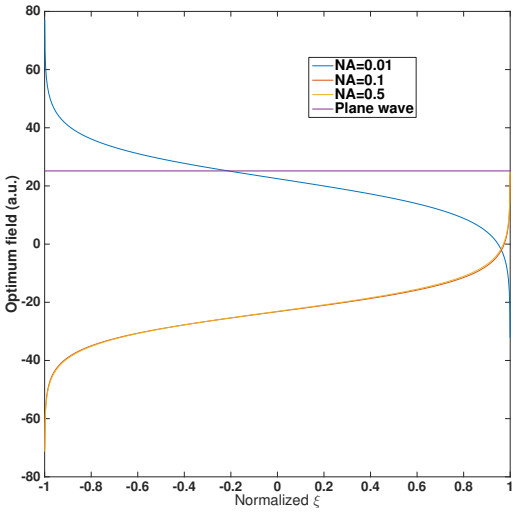

Figure 5.3: Plot of the optimum field A^i as a function of ξ for different numerical apertures. The side-wall angle $\alpha = 85$ and height $h = \lambda/3$ of the cliff are fixed. Changing the value of the numerical aperture of the system influences the behavior of the optimum field, nevertheless the difference between the NA = 0.1 case and NA = 0.5 is barely noticeable.

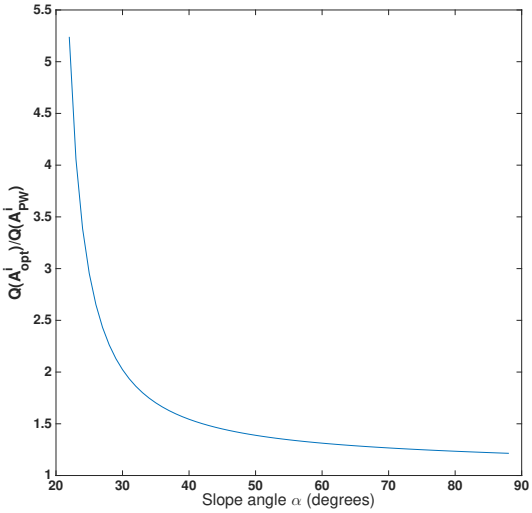

Figure 5.4: Plot of the sensitivity ratio as a function of SWA α. The numerical aperture NA = 0.3 and height $h = \lambda/3$ of the cliff are fixed. An optimized field (compare to a plane wave illumination) is much more sensitive to the side-wall angle of a cliff-like structure, given a fixed numerical aperture of the input pupil.

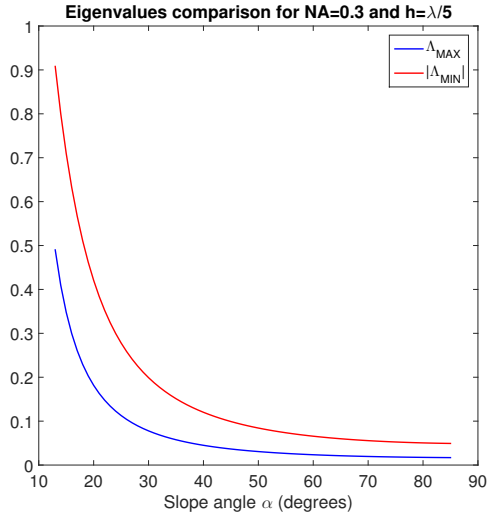

Figure 5.5: Plot of the eigenvalues as a function of SWA α. The numerical aperture NA = 0.3 and height $h = \lambda/5$ of the cliff are fixed. It is important to compute both the maximum eigenvalue and the minimum one, because the latter can also represent the best solution to the problem.

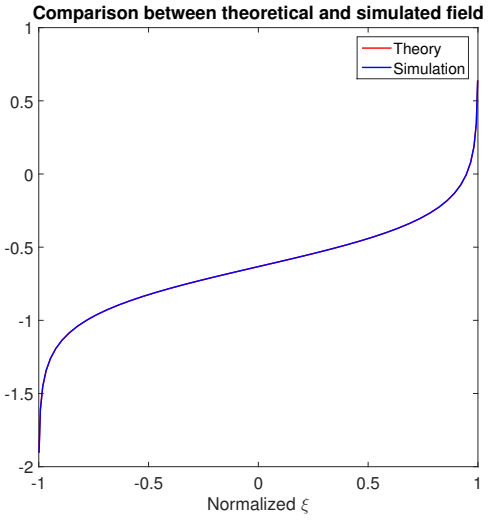

Figure 5.6: Comparison between theoretical and simulated field as a function of SWA α. The numerical aperture NA = 0.3 and height $h = \lambda/5$ of the cliff are fixed. When we consider the case NA $\to 0$, there is a perfect agreement between simulation and theory.

5.4. Split detector case

In the previous section we saw that, if the optimize field is calculate though the function given by Eq. (5.7), the gain in sensitivity is not as high as expected. Therefore, we looked into other methods that might be more beneficial for the side-wall estimation. In particular, the sensitivity to the side-wall angle variation is greatly enhanced if we consider a split detector configuration. In this type of detection scheme, the sensor area is divided into two identical halves which are separately integrated and whose difference is monitored over several sample positions perpendicular to the beam propagation direction. In the following subsections, we will detail the mathematical derivation and the main results concerning this method.

5.4.1. The Lagrange mutliplier rule

In Section 5.3.1 we have introduced the Lagrange multiplier rule for inequality constraints [25] to solve the optimization problem; once again, we make use of this rule in this case as well. We remind the reader that, if A^i are the plane wave amplitudes of the optimum incident field, then according to this theorem there is a Lagrange multiplier Λ such that the following equation is satisfied for all complex B^i:

$$\delta G(A^i)(B^i) - \Lambda \delta P(A^i)(B^i) = 0, \tag{5.50}$$

where $\delta G(A^i)(B^i)$ and $\delta P(A^i)(B^i)$ are the Gateaux derivatives of the functionals $G(A^i)$ and $P(A^i)$ in the direction of B^i. We have:

$$\begin{aligned}\delta G(A^i)(B^i) = 2\Re\Bigg\{ & \int_0^{+\frac{\mathrm{NA}}{\lambda}} \left[A^i * \frac{d\mathcal{F}(r_\alpha)}{d\alpha} \overline{B^i} * \overline{\mathcal{F}(r_\alpha)} \right. \\ & \left. + A^i * \mathcal{F}(r_\alpha) \overline{B^i} * \overline{\frac{d\mathcal{F}(r_\alpha)}{d\alpha}} \right] d\xi \\ & - \int_{-\frac{\mathrm{NA}}{\lambda}}^0 \left[A^i * \frac{d\mathcal{F}(r_\alpha)}{d\alpha} \overline{B^i} * \overline{\mathcal{F}(r_\alpha)} \right. \\ & \left. + A^i * \mathcal{F}(r_\alpha) \overline{B^i} * \overline{\frac{d\mathcal{F}(r_\alpha)}{d\alpha}} \right] d\xi \Bigg\}.\end{aligned} \tag{5.51}$$

Let us focus on the first integral in the right-hand side of Eq. (5.51):

$$\begin{aligned}T_+(A^i)(B^i) = 2\Re \int_0^{+\frac{\mathrm{NA}}{\lambda}} & \left[A^i * \frac{d\mathcal{F}(r_\alpha)}{d\alpha} \overline{B^i} * \overline{\mathcal{F}(r_\alpha)} \right. \\ & \left. + A^i * \mathcal{F}(r_\alpha) \overline{B^i} * \overline{\frac{d\mathcal{F}(r_\alpha)}{d\alpha}} \right] d\xi\end{aligned} \tag{5.52}$$

We have:

$$T_+(A^i)(B^i) = 2\Re\Bigg\{\int_0^{+\frac{\mathrm{NA}}{\lambda}} A^i * \frac{d\mathcal{F}(r_\alpha)}{d\alpha}(\xi) \int_{-\frac{\mathrm{NA}}{\lambda}}^{+\frac{\mathrm{NA}}{\lambda}} \overline{B^i(\xi')} \times \overline{\mathcal{F}(r_\alpha)(\xi-\xi')}\, d\xi\, d\xi' + \int_0^{+\frac{\mathrm{NA}}{\lambda}} A^i * \mathcal{F}(r_\alpha)(\xi) \times \int_{-\frac{\mathrm{NA}}{\lambda}}^{+\frac{\mathrm{NA}}{\lambda}} \overline{\frac{d\mathcal{F}(r_\alpha)(\xi-\xi')}{d\alpha}}\, \overline{B^i(\xi')}\, d\xi' d\xi \Bigg\} \tag{5.53}$$

after some algebra we find:

$$T_+(A^i)(B^i) = \int_{-\frac{\mathrm{NA}}{\lambda}}^{+\frac{\mathrm{NA}}{\lambda}} \int_{-\frac{\mathrm{NA}}{\lambda}}^{+\frac{\mathrm{NA}}{\lambda}} \mathcal{K}_+(\xi,\xi')\, A^i(\xi')\, d\xi'\, \overline{B^i(\xi)}\, d\xi \tag{5.54}$$

where the Kernel $\mathcal{K}_+(\xi,\xi')$ is given by:

$$\mathcal{K}_+(\xi,\xi') = \int_0^{+\frac{\mathrm{NA}}{\lambda}} \Bigg[\frac{d\mathcal{F}(r_\alpha)(\xi''-\xi')}{d\alpha}\, \overline{\mathcal{F}(r_\alpha)(\xi''-\xi)} + \overline{\frac{d\mathcal{F}(r_\alpha)(\xi''-\xi)}{d\alpha}}\, \mathcal{F}(r_\alpha)(\xi''-\xi')\Bigg] d\xi''. \tag{5.55}$$

We apply a similar computation to the second integral in the right-hand side of Eq. (5.51):

$$T_-(A^i)(B^i) = 2\Re \int_{-\frac{\mathrm{NA}}{\lambda}}^{0} \Bigg[A^i * \frac{d\mathcal{F}(r_\alpha)}{d\alpha}\, \overline{B^i} * \overline{\mathcal{F}(r_\alpha)} + A^i * \mathcal{F}(r_\alpha)\, \overline{B^i} * \overline{\frac{d\mathcal{F}(r_\alpha)}{d\alpha}}\Bigg] d\xi \tag{5.56}$$

and obtain:

$$T_-(A^i)(B^i) = 2\Re \int_{-\frac{\mathrm{NA}}{\lambda}}^{+\frac{\mathrm{NA}}{\lambda}} \int_{-\frac{\mathrm{NA}}{\lambda}}^{+\frac{\mathrm{NA}}{\lambda}} \mathcal{K}_-(\xi,\xi')\, A^i(\xi')\, d\xi'\, \overline{B^i(\xi)}\, d\xi \tag{5.57}$$

where:

$$\mathcal{K}_-(\xi',\xi'') = \int_{-\frac{\mathrm{NA}}{\lambda}}^{0} \Bigg[\frac{d\mathcal{F}(r_\alpha)(\xi''-\xi')}{d\alpha}\, \overline{\mathcal{F}(r_\alpha)(\xi''-\xi)} + \overline{\frac{d\mathcal{F}(r_\alpha)(\xi''-\xi)}{d\alpha}}\, \mathcal{F}(r_\alpha)(\xi''-\xi')\Bigg] d\xi''. \tag{5.58}$$

Note that $\mathcal{K}_-$ is formally identical to $\mathcal{K}_+$ in Eq. (5.55), provided we change the integration limits. Hence the functional $\delta G(A^i)(B^i)$ can be written as:

$$\begin{aligned}\delta G(A^i)(B^i) &= T_+(A^i)(B^i) - T_-(A^i)(B^i) \\ &= 2\Re \int_{-\frac{\mathrm{NA}}{\lambda}}^{+\frac{\mathrm{NA}}{\lambda}} \int_{-\frac{\mathrm{NA}}{\lambda}}^{+\frac{\mathrm{NA}}{\lambda}} \mathcal{K}(\xi,\xi')\, A^i(\xi')\, d\xi'\, \overline{B^i(\xi)}\, d\xi \end{aligned} \tag{5.59}$$

with:

$$\mathcal{K}(\xi,\xi') = \mathcal{K}_+(\xi,\xi') - \mathcal{K}_-(\xi,\xi'), \tag{5.60}$$

Note that since $G(A^i) = 1/2\, \delta G(A^i)(A^i)$, Eq. (5.59) implies:

$$G(A^i) = \Re \int_{-\frac{\mathrm{NA}}{\lambda}}^{+\frac{\mathrm{NA}}{\lambda}} \int_{-\frac{\mathrm{NA}}{\lambda}}^{+\frac{\mathrm{NA}}{\lambda}} \mathcal{K}(\xi,\xi')\, A^i(\xi) \overline{A^i(\xi')}\, d\xi\, d\xi' \tag{5.61}$$

and this holds for any pupil field A^i (not only the optimum one).

The Gateaux derivative of the power $P(A^i)$ in the direction of B^i is given by:

$$\delta P(A^i)(B^i) = 2\Re \int_{-\frac{\mathrm{NA}}{\lambda}}^{+\frac{\mathrm{NA}}{\lambda}} A^i(\xi)\, \overline{B^i(\xi)}\, d\xi. \tag{5.62}$$

Since B^i is an arbitrary complex valued pupil field, Eqs. (5.50), (5.59) and (5.62) imply:

$$\int_{-\frac{\mathrm{NA}}{\lambda}}^{+\frac{\mathrm{NA}}{\lambda}} \mathcal{K}(\xi,\xi')\, A^i(\xi')\, d\xi' - \Lambda A^i(\xi) = 0. \tag{5.63}$$

Hence the optimum field $A^i(\xi)$ is eigenfunction, with eigenvalue Λ, of the integral operator with kernel $\mathcal{K}$. As we did in Section 5.3.1, we can conclude that the solution of our optimization problem is the eigenfunction A^i corresponding to the eigenvalue for which $|\Lambda|$ is maximum, based on the following equations.

$$\delta G(A^i)(A^i) = 2G(A^i), \qquad \delta P(A^i)(A^i) = 2P(A^i) \tag{5.64}$$

thus Eq. (5.50) gives, with $B^i = A^i$ and for a unit power:

$$G(A^i) = \Lambda. \tag{5.65}$$

5.4.2. Computation of the kernel $\mathcal{K}$

The derivation of the optimum filed for the split detection case is quite similar to what we have already done when we have considered the optimization problem based on the total reflected intensity. This means that we need to substitute the expressions of the Fourier transform of the reflection function and its derivative with

respect to the side wall angel α into the definitions of $\mathcal{K}_+$ and $\mathcal{K}_-$:

$$\mathcal{F}(r_\alpha)(\xi) = \exp(ikh)\left[-\frac{\sin\left(kh+\pi h\frac{\xi}{\tan\alpha}\right)}{\pi}\mathrm{PV}\left(\frac{1}{\xi}\right) + \delta(\xi)\cos(kh) + \frac{\sin\left(kh+\pi h\frac{\xi}{\tan\alpha}\right)}{k\tan\alpha+\pi\xi}\right] \tag{5.66}$$

$$\frac{d\mathcal{F}(r_\alpha)(\xi)}{d\alpha} = \exp(ikh)\left[\frac{kh\cos\left(kh+\pi h\frac{\xi}{\tan\alpha}\right)}{k\sin^2\alpha+\frac{\pi\xi}{2}\sin(2\alpha)} - \frac{k\sin\left(kh+\pi h\frac{\xi}{\tan\alpha}\right)}{k^2\sin^2\alpha+\pi^2\xi^2\cos^2\alpha+k\pi\xi\sin(2\alpha)}\right] \tag{5.67}$$

We would like to emphasize once again that both the right-hand sides of Eqs. (5.66) and (5.67) are real except for the factor $\exp(ikh)$ which multiplies all terms. Therefore, $\mathcal{K}_+$ and $\mathcal{K}_-$ are real valued functions and hence the kernel $\mathcal{K}$ is also real. Hence all the eigenvalues must be real. Furthermore, we can write $\mathcal{K}_+(\xi,\xi')$ (and so $\mathcal{K}_-(\xi,\xi')$) as:

$$\mathcal{K}_+(\xi,\xi') = \mathcal{H}(\xi,\xi') + \overline{\mathcal{H}(\xi',\xi)} \tag{5.68}$$

with:

$$\mathcal{H}(\xi,\xi') = \int_0^{+\frac{\mathrm{NA}}{\lambda}} \overline{\frac{d\mathcal{F}(r_\alpha)(\xi''-\xi)}{d\alpha}}\,\mathcal{F}(r_\alpha)(\xi''-\xi')\,d\xi'' \tag{5.69}$$

We can calculate $\mathcal{H}(\xi,\xi')$ by substituting the expressions for $\mathcal{F}(r_\alpha)$ and $d\mathcal{F}(r_\alpha)/d\alpha$ given by Eqs. (5.66) and (5.67):

$$\begin{aligned}\mathcal{H}(\xi,\xi') = &-\frac{\exp(ikh)}{\pi}\,\mathrm{PV}\int_0^{+\frac{\mathrm{NA}}{\lambda}}\frac{1}{\xi''-\xi'}\sin\left[kh+\pi h\frac{(\xi''-\xi')}{\tan\alpha}\right]\overline{\frac{d\mathcal{F}(r_\alpha)(\xi''-\xi)}{d\alpha}}\,d\xi'' \\ &+\exp(ikh)\cos(kh)\,\overline{\frac{d\mathcal{F}(r_\alpha)(\xi'-\xi)}{d\alpha}} \\ &+\exp(ikh)\int_0^{+\frac{\mathrm{NA}}{\lambda}}\overline{\frac{d\mathcal{F}(r_\alpha)(\xi''-\xi)}{d\alpha}}\,\frac{\sin\left[kh+\pi h\frac{(\xi''-\xi')}{\tan\alpha}\right]}{k\tan\alpha+\pi(\xi''-\xi')}\,d\xi''.\end{aligned} \tag{5.70}$$

The Cauchy Principal Value integral in the right-hand side of Eq. (5.70) requires careful examination. To calculate it, we define a new function $w(\xi'')$ containing part of the integrand:

$$w(\xi'') = \sin\left[kh+\pi h\frac{(\xi''-\xi')}{\tan\alpha}\right]\overline{\frac{d\mathcal{F}(r_\alpha)(\xi''-\xi)}{d\alpha}} \tag{5.71}$$

The Cauchy Principal Value integral can now be written as:

$$
\begin{aligned}
I_{PV}(\xi') &= -\frac{\exp(ikh)}{\pi}\,\mathrm{PV}\int_0^{+\frac{\mathrm{NA}}{\lambda}} \frac{w(\xi'')}{\xi''-\xi'}d\xi'' \\
&= -\frac{\exp(ikh)}{\pi}\lim_{\epsilon\to 0}\left[\left(\int_0^{\xi'-\epsilon}+\int_{\xi'+\epsilon}^{+\frac{\mathrm{NA}}{\lambda}}\right)\frac{w(\xi'')-w(\xi')}{\xi''-\xi'}d\xi''\right. \\
&\quad \left. + w(\xi')\left(\int_0^{\xi'-\epsilon}+\int_{\xi'+\epsilon}^{+\frac{\mathrm{NA}}{\lambda}}\right)\frac{1}{\xi''-\xi'}\,d\xi''\right] \\
&= -\frac{\exp(ikh)}{\pi}\left[\int_0^{+\frac{\mathrm{NA}}{\lambda}}\frac{w(\xi'')-w(\xi')}{\xi''-\xi'}\,d\xi''\right. \\
&\quad \left. + w(\xi')\lim_{\epsilon\to 0}\left(\int_0^{\xi'-\epsilon}+\int_{\xi'+\epsilon}^{+\frac{\mathrm{NA}}{\lambda}}\right)\frac{1}{\xi''-\xi'}\,d\xi''\right] \\
&= -\frac{\exp(ikh)}{\pi}\left[\int_0^{+\frac{\mathrm{NA}}{\lambda}}\frac{w(\xi'')-w(\xi')}{\xi''-\xi'}\,d\xi'' + w(\xi')\ln\left|\frac{\frac{\mathrm{NA}}{\lambda}-\xi'}{\xi'}\right|\right]. \qquad (5.72)
\end{aligned}
$$

Note that, in the last step of Eq. (5.72), the first integral is a regular integral because w is a smooth function. Finally, we get for $\mathcal{H}(\xi,\xi')$:

$$
\begin{aligned}
\mathcal{H}(\xi,\xi') &= -\frac{\exp(ikh)}{\pi}\int_0^{+\frac{\mathrm{NA}}{\lambda}}\frac{w(\xi'')-w(\xi')}{\xi''-\xi'}\,d\xi'' \\
&\quad -\frac{\exp(ikh)}{\pi}\ln\left|\frac{\frac{\mathrm{NA}}{\lambda}-\xi'}{\xi'}\right|\sin(kh)\,\overline{\frac{d\mathcal{F}(r_\alpha)(\xi'-\xi)}{d\alpha}} \\
&\quad +\exp(ikh)\,\cos(kh)\overline{\frac{d\mathcal{F}(r_\alpha)(\xi'-\xi)}{d\alpha}} \\
&\quad +\exp(ikh)\int_0^{+\frac{\mathrm{NA}}{\lambda}}\overline{\frac{d\mathcal{F}(r_\alpha)(\xi''-\xi)}{d\alpha}}\,\frac{\sin\left[kh+\pi h\frac{(\xi''-\xi')}{\tan\alpha}\right]}{k\tan\alpha+\pi(\xi''-\xi')}\,d\xi'', \qquad (5.73)
\end{aligned}
$$

Note that for $\xi''=\xi'$:

$$
w(\xi'')\Big|_{\xi''=\xi'} = \sin(kh)\,\overline{\frac{d\mathcal{F}(r_\alpha)(\xi'-\xi)}{d\alpha}}. \qquad (5.74)
$$

It follows from Eq. (5.73) that $\mathcal{H}$, and also $\mathcal{K}_+$, is a smooth real function. The Kernel $\mathcal{K}$ is numerically computed using Gauss-Lagrange quadrature integration method as discussed in Section 5.3.4.

5.4.3. Computation of the optimized field

In this section, we will study the optimized pupil field $A^i(\xi)$ for some values of the slope angle α, the height h, the numerical aperture NA of the system and for unit

power in the beam. Furthermore, we will compare the sensitivity for a change of SWA for the optimum pupil field with that of a plane wave. In the optimized case, the maximum sensitivity is given by the maximum of the absolute value of the eigenvalues, whereas for a plane wave A^i_{PW}, using the same split detector configuration, the sensitivity follows from Eq. (5.61) as:

$$G(A^i_{\mathrm{PW}}) = |A^i_0|^2 \Re \int_{-\frac{\mathrm{NA}}{\lambda}}^{+\frac{\mathrm{NA}}{\lambda}} \int_{-\frac{\mathrm{NA}}{\lambda}}^{+\frac{\mathrm{NA}}{\lambda}} \mathcal{K}(\xi, \xi')\, d\xi\, d\xi' \tag{5.75}$$

where the amplitude A^i_0 of the plane wave must be chosen such that the power is unity, i.e. $|A^i_0|^2 = \lambda/(2\,\mathrm{NA})$. The sensitivity for the plane wave case is then simply proportional to the double integral of the kernel $\mathcal{K}(\xi, \xi')$. It is important to point out that it is critical to find both the strongest positive and most negative eigenvalues because we are interested in finding the input field which gives the steepest change in the reflected intensity. Hence its most negative eigenvalue could also diminish when the SWA increases, thus the associated eigenvector could yield the optimum pupil field. Decisive is what eigenvalue has maximum absolute value.

All the plots have been obtained by considering the input illumination in the visible part of the spectrum ($\lambda = 633nm$), but other optical regimes can be investigated. Since the kernel $\mathcal{K}$ and the eigenvalues are real, it follows from Eq. (5.63) that the optimum pupil field can be taken to be real and its phase is thus 0 or π in all pupil points.

Figure 5.7 shows the profiles of the absolute value of the optimized pupil field, along with a plane wave of amplitude A^i_0, as a function of the coordinate ξ (normalized to 1 by the factor λ/NA), for SWA $= 10°, 20°, 40°, 60°, 89°$, $h = \lambda/3$ and NA $= 0.4$. We can readily see that the profile of the optimum $A^i(\xi)$ differs strongly from a plane wave, with most of the energy concentrated in the center of the pupil. In the case $\alpha = 10°$, the optimum solution undergoes a phase change, indicated with the labels "(0)" and "(π)", near $\xi = 0.65$. This is also the only case in which the phase changes sign within the pupil. The profile becomes less and less asymmetric around zero when the slope angle increases, but still little asymmetries arise for positive values of ξ. We also notice that the solutions for $\alpha = 60°$ and $\alpha = 89°$ are basically overlapping each other, thereby suggesting a decrease in the sensitivity when the side-wall angle is very steep. Furthermore, the absolute value of the amplitude of the optimize field tends to strong positive values when $x = 0$; this result is a consequence of our detection scheme, where we divide the detector in two halves and we subtract one from the other. In Figure 5.8, the absolute value of the optimum solution is plotted for $\alpha = 85°$, $h = \lambda/3$ and NA $= 0.25$ and 0.4. Changing the numerical aperture of the system has a stronger impact on the solution than changing the SWA, particularly when the angle gets very steep, when the NA is fixed (Figure 5.7). The overall trend of the absolute value of the optimum field is the same for each numerical aperture but the rate at which each solution approaches strong positive values is different.

In Figure 5.9, the ratio of the optimum sensitivity $G(A^i)$ over the corresponding value $G(A^i_{\mathrm{PW}})$ for the plane wave case, is plotted for different values of the SWA

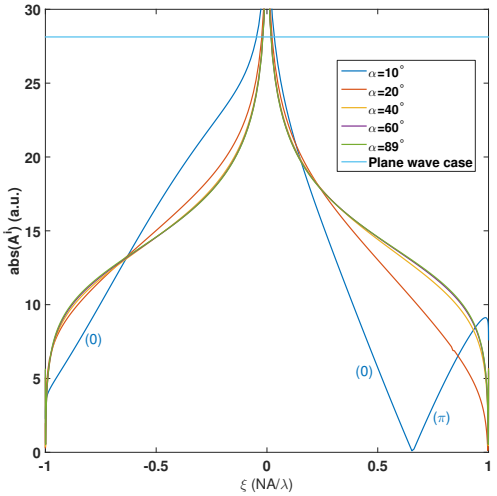

Figure 5.7: The absolute value of the optimized pupil field is plotted for several values of the slope angle α, when NA = 0.4 and $h = \lambda/3$. For the case $\alpha = 10°$, we emphasize the phase change along the pupil. As a comparison, the amplitude of a plane wave normalized by $\sqrt{\lambda/(2\,\mathrm{NA})}$ is also plotted.

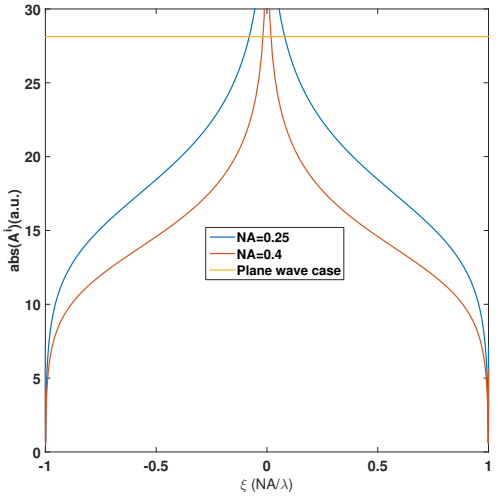

Figure 5.8: The absolute value of the optimized pupil field is plotted for two different values of the numerical aperture NA, when $\alpha = 85°$ and $h = \lambda/3$. As a comparison, the amplitude of a plane wave normalized by $\sqrt{\lambda/(2\,\mathrm{NA})}$, when NA = 0.4, is also plotted.

in a range from $20°$ to $90°$ and for a fixed NA $= 0.4$, $h = \lambda/3$ and $\lambda/4$. The gain in sensitivity decreases with increasing angles, nevertheless, by shaping the input pupil field, sensitivity of the SWA detection can be increased by more than 150% compared to the plane wave illumination case. Furthermore, we notice that when the side-wall angle gets very steep, changing the height of the sample, i.e. the phase retardation, does not influence the gain in sensitivity.

We have verified how this amplitude profile could be implemented in a commercial Spatial Light Modulator (SLM) characterized by a fill factor of 90%, a pixel size of $8.1\mu m$ and a dynamic range of 256 gray levels coded in a 8 bit signal. We did this by comparing the sensitivity to the SWA obtained from the optimum field A^i with the one calculated from the approximated field generated by a SLM, for the same values of numerical aperture and height, i.e. NA $= 0.4$ and $h = \lambda/3$. The difference between the sensitivities of the theoretical optimum field and the approximated field that can be realized by a SLM is less than 2%. Therefore the optimum solution we calculated can be implemented experimentally with commercially available liquid crystal on silicon (LCOS) devices, with a good approximation.

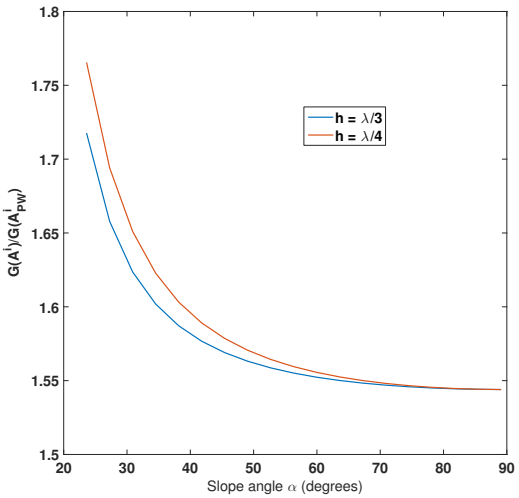

Figure 5.9: Ratio of the optimum sensitivity $G(A^i)$ and the one associated to a plane wave illumination $G(A^i_{\text{PW}})$ as a function of the SWA α, when NA $= 0.4$, $h = \lambda/3$ and $h = \lambda/4$. For high slope angles the increase in sensitivity is more than 150%.

Figure 5.10 shows the absolute value of the optimized focused spot, along with the profile of a focused plane wave, for a cliff structure with $h = \lambda/3$ and an objective with numerical aperture NA $= 0.4$, with different slope angles $\alpha = 10°, 20°, 40°, 60°, 89°$. In this case, each curve has been normalized such that the power is unity. The focused spot obtained by the optimum pupil field A^i contains much more energy into the external lobes, compare to the focused plane wave case, as expected from the profile of the pupil field itself. In Figure 5.11, another example of the absolute value of the optimized focused spot is shown, but in this

case $h = \lambda/4$.

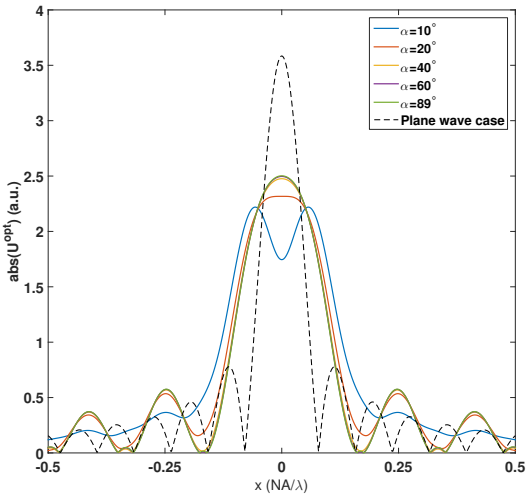

Figure 5.10: Comparison between the absolute values of a focused plane wave and the focused optimum pupil field $U^{\text{opt}} = \mathcal{F}(A^i)$ when NA = 0.4 and $h = \lambda/3$.

5.4.4. Determination of the SWA using the optimized input field

In this section we describe how the side-wall angle can be determined starting from the optimum field profile. First of all, it is important to remind that it is possible to have prior knowledge on the side-wall angle, for example in the case of test patterns, the SWA that is to be realized is known. Moreover, Fig. 5.9 shows that, when dealing with steep values of side-wall angle, which are common in the semiconductor industry and lithographic applications, the profile of the sensitivity is flat. The consequence of this trend is that it is less important to know the exact value of the slope angle for the optimization process.

Let $A^i_{\tilde{\alpha}}$ be the optimized incident field corresponding to the assumed angle $\tilde{\alpha}$. For a SWA α close to $\tilde{\alpha}$, the reflected intensity when the incident field is $A^i_{\tilde{\alpha}}$:

$$I^{\text{out}}_{\alpha}(\xi) = \left|\left[A^i_{\tilde{\alpha}} * \mathcal{F}(r_\alpha)\right](\xi)\right|^2. \tag{5.76}$$

The measured signal is the difference of the total intensities measured by the two halves of the detector and by comparing this measured signal to the theoretical one, we determine the slope angle α. The error σ_α in the determination of the angle is:

$$\sigma_\alpha = \frac{\text{Error in the measured signal}}{G_\alpha\left(A^i_{\tilde{\alpha}}\right)} \tag{5.77}$$

where $G_\alpha(A^i_{\tilde{\alpha}})$ is the sensitivity for detecting α while using the illumination that is

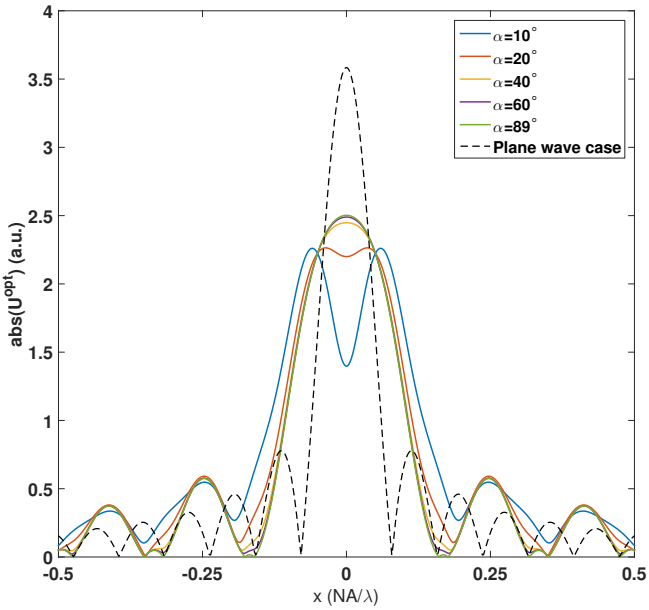

Figure 5.11: Comparison between the absolute values of a focused plane wave and the focused optimum pupil field $U^{\text{opt}} = \mathcal{F}(A^i)$ when NA = 0.4 and $h = \lambda/4$.

optimum for $\tilde{\alpha}$:

$$\begin{aligned} G_\alpha\left(A^i_{\tilde{\alpha}}\right) &= \int_0^{+\frac{\text{NA}}{\lambda}} \frac{d}{d\alpha}\left|\left[A^i_{\tilde{\alpha}} * \mathcal{F}(r_\alpha)\right](\xi)\right|^2 d\xi \\ &\quad - \int_{-\frac{\text{NA}}{\lambda}}^{0} \frac{d}{d\alpha}\left|\left[A^i_{\tilde{\alpha}} * \mathcal{F}(r_\alpha)\right](\xi)\right|^2 d\xi \\ &= 2\Re\left(\int_0^{+\frac{\text{NA}}{\lambda}} - \int_{-\frac{\text{NA}}{\lambda}}^{0}\right) A^i_{\tilde{\alpha}} * \frac{d\mathcal{F}(r_\alpha)}{d\alpha}\,\overline{A^i_{\tilde{\alpha}} * \mathcal{F}(r_\alpha)}\, d\xi \end{aligned} \tag{5.78}$$

where the Fourier transform of the reflection function, along with its derivative, are given by Eqs. (5.66) and (5.67). Let $\alpha_{\min}(\tilde{\alpha}) < \tilde{\alpha} < \alpha_{\max}(\tilde{\alpha})$ be such that for all $\alpha_{\min}(\tilde{\alpha}) \leq \alpha \leq \alpha_{\max}(\tilde{\alpha})$:

$$\frac{\left|G_\alpha\left(A^i_{\tilde{\alpha}}\right) - G_\alpha\left(A^i_{\alpha}\right)\right|}{G_\alpha\left(A^i_{\alpha}\right)} < 0.1. \tag{5.79}$$

In Fig. 5.12 we plot $\alpha_{\min}(\tilde{\alpha})$, $\alpha_{\max}(\tilde{\alpha})$ for $40° \leq \tilde{\alpha} \leq 90°$, for $h = \lambda/4$ and $h = \lambda/3$, when NA $= 0.4$. When the optimum field $A^i_{\tilde{\alpha}}$ is used as input beam to investigate a cliff with SWA $\alpha \neq \tilde{\alpha}$, the length of the interval in which the sensitivity differs less than 10% from the optimum one, increases for higher slope angles. In fact, as mentioned earlier in this section, the profile of the optimum sensitivity (Fig. 5.9)

is flat when the slope angle is very steep, therefore it is not necessary to use the optimum illumination of the exact slope angle. To achieve high sensitivity it suffices to be able to guess the side wall angle with sufficient accuracy and use the optimum illumination of that guess. Furthermore, we can notice that if we illuminate a cliff-like sample with the optimum beam calculated for $\tilde{\alpha}$, it is possible to determine a side-wall angle of $72°$ for both the different heights considered. The value of α_{max} reaches a maximum when $\tilde{\alpha} = 72°$ for $h = \lambda/4$ and $\tilde{\alpha} = 70°$ in the case of $h = \lambda/3$, after this point the sensitivity of the detection differs always less than 10% of that of the optimum, when the optimum illumination is used.

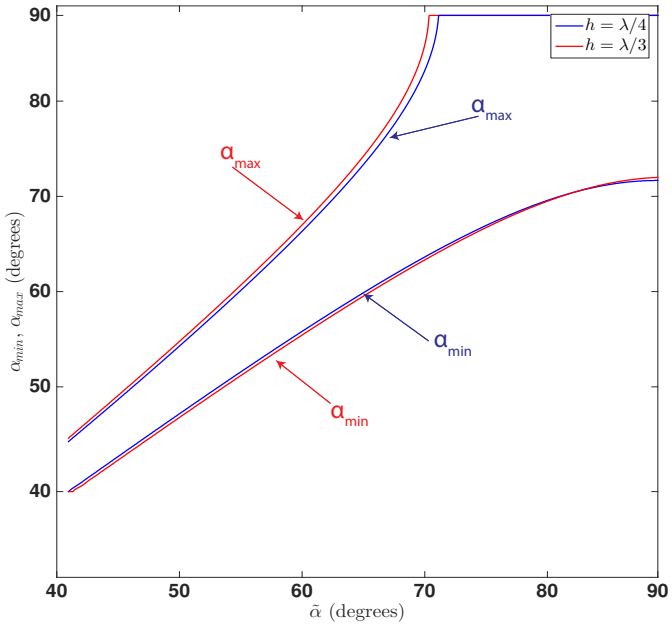

Figure 5.12: For every $\tilde{\alpha}$ on the horizontal axis, the lower and upper bound of the interval of slope angles are shown for which the sensitivity of the detection differs less than 10% of that of the optimum one when the optimum illumination of $\tilde{\alpha}$ is used.

5.5. Conclusion

In this chapter we determine, for a cliff-like structure modeled as a phase object and using scalar theory, the amplitude and phase of a focused beam which gives the highest sensitivity to the change of the side-wall angle when using a split detector. The problem is formulated mathematically as an optimization problem for the field in the pupil of a cylindrical lens. We investigated two different functionals that are to be maximized. On the one hand we maximize the derivative with respect to the side-wall angle α of the total reflected intensity of the object under study. On the other hand, we maximize the derivative with respect to the SWA α of the difference in scattered light intensities as measured by a split detector. In

both cases, the constraint on the pupil field is that the power in the incident beam is fixed. The optimum pupil field is shown to be the eigenfunction of an integral operator corresponding to the eigenvalue with largest absolute value. This problem is solved by standard numerical methods. Our results show that only in the latter case - maximize the derivative with respect to the SWA α of the difference in scattered light intensities as measured by a split detector - the optimum sensitivity is substantially higher compared to when a plane wave focused by a cylindrical lens is used as illumination. The split detector configuration, where we consider the difference between the intensities measured by the two halves of the detector, entails a much higher optimum sensitivity than by detecting the total reflected light, without sacrificing acquisition speed. Although our results are based on rather restrictive assumptions of scalar theory and phase object, the optimum fields derived may be used as starting values in more rigorous optimization problems which use Maxwell's equations to describe the interaction of the illumination with the structure.

References

[1] L. Cisotto and H. P. Urbach, *Amplitude and phase beam shaping for highest sensitivity in sidewall angle detection,* J. Opt. Soc. Am. A **34**, 52 (2017).

[2] K. Murayama, S. Gonda, H. Koyanagi, T. Terasawa, and S. Hosaka, *Sidewall measurement using tilt-scanning method in atomic force microscope,* Japanese Journal of Applied Physics **45**, 5423 (2006).

[3] G. Dai, K. Hahm, F. Scholze, M.-A. Henn, H. Gross, J. Fluegge, and H. Bosse, *Measurements of cd and sidewall profile of euv photomask structures using cd-afm and tilting-afm,* Measurement Science and Technology **25**, 044002 (2014).

[4] J. Garnaes, P.-E. Hansen, N. Agersnap, J. Holm, F. Borsetto, and A. Kühle, *Profiles of a high-aspect-ratio grating determined by spectroscopic scatterometry and atomic-force microscopy,* Appl. Opt. **45**, 3201 (2006).

[5] P. R. Bingham, J. R. Price, K. W. Tobin, Jr., T. P. Karnowski, M. H. Bennett, E. H. Bogardus, and M. Bishop, *Sidewall structure estimation from cd-sem for lithographic process control,* in *Process and Materials Characterization and Diagnostics in IC Manufacturing*, Vol. 5041 (2003) pp. 115–126.

[6] A. Faridian, V. F. Paz, K. Frenner, G. Pedrini, A. D. Boef, and W. Osten, *Phase-sensitive structured illumination to detect nanosized asymmetries in silicon trenches,* Journal of Micro/Nanolithography, MEMS, and MOEMS **14**, 021104 (2015).

[7] M. Wurm, F. Pilarski, and B. Bodermann, *A new flexible scatterometer for critical dimension metrology,* Review of Scientific Instruments **81** (2010), http://dx.doi.org/10.1063/1.3280160.

[8] M. Wurm, S. Bonifer, B. Bodermann, and M. Gerhard, *Comparison of far field characterisation of does with a goniometric duv-scatterometer and a ccd-based system,* Journal of the European Optical Society - Rapid publications **6** (2011).

[9] B. Den, A. Bleeker, D. Van, M. Dusa, A. Kiers, P. Luehrmann, H. Pellemans, D. Van, C. Grouwstra, and K. Van, *Method and apparatus for angular-resolved spectroscopic lithography characterisation,* (2006), eP Patent App. EP20,050,254,994.

[10] T. G. Brown, M. A. Alonso, A. Vella, M. J. Theisen, S. T. Head, S. R. Gillmer, and J. D. Ellis, *Focused beam scatterometry for deep subwavelength metrology,* in *Three-Dimensional and Multidimensional Microscopy: Image Acquisition and Processing XXI*, Vol. 8949 (2014) pp. 89490Y–89490Y–7.

[11] O. El Gawhary, N. Kumar, S. F. Pereira, W. M. J. Coene, and H. P. Urbach, *Performance analysis of coherent optical scatterometry,* Applied Physics B **105**, 775 (2011).

[12] N. Kumar, O. E. Gawhary, S. Roy, S. F. Pereira, and H. P. Urbach, *Phase retrieval between overlapping orders in coherent fourier scatterometry using scanning,* J. Europ. Opt. Soc. Rap. Public. **8**, 13048 (2013).

[13] S. Roy, N. Kumar, S. F. Pereira, and H. P. Urbach, *Interferometric coherent fourier scatterometry: a method for obtaining high sensitivity in the optical inverse-grating problem,* Journal of Optics **15**, 075707 (2013).

[14] N. Kumar, L. Cisotto, S. Roy, G. K. P. Ramanandan, S. F. Pereira, and H. P. Urbach, *Determination of the full scattering matrix using coherent fourier scatterometry,* Appl. Opt. **55**, 4408 (2016).

[15] R. W. Tyson, *Principles of Adaptive Optics* (Academic Press, Boston, MA, 1998).

[16] P. Rai-Choudhury, *MEMS and MOES : Technology and Applications* (SPIE Press Monographies, Bellingham, Washington, 2000).

[17] J. Leach, G. Sinclair, P. Jordan, J. Courtial, M. J. Padgett, J. Cooper, and Z. J. Laczik, *3d manipulation of particles into crystal structures using holographic optical tweezers,* Opt. Express **1**, 220 (2004).

[18] D. G. Grier and Y. Roichman, *Holographic optical trapping,* Appl. Opt. **5**, 880 (2006).

[19] E. Eriksson, J. Scrimgeour, J. Enger, and M. Goksor, *Holographic optical tweezers combined with a microfluidic device for exposing cells to fast environmental changes,* Proc. SPIE **6592**, 65920P (2007).

[20] A. P. Mosk, *High-resolution imaging with scattered light,* in *2013 Conference on Lasers Electro-Optics Europe International Quantum Electronics Conference CLEO EUROPE/IQEC* (2013) pp. 1–1.

[21] J. Aulbach, B. Gjonaj, P. M. Johnson, A. P. Mosk, and A. Lagendijk, *Control of light transmission through opaque scattering media in space and time,* Phys. Rev. Lett. **106**, 103901 (2011).

[22] D. Akbulut, T. J. Huisman, E. G. van Putten, W. L. Vos, and A. P. Mosk, *Focusing light through random photonic media by binary amplitude modulation,* Opt. Express **19**, 4017 (2011).

[23] Z. Chen, T. Zeng, B. Qian, and J. Ding, *Complete shaping of optical vector beams,* Opt. Express **23**, 17701 (2015).

[24] W. Han, Y. Yang, W. Cheng, and Q. Zhan, *Vectorial optical field generator for the creation of arbitrarily complex fields,* Opt. Express **21**, 20692 (2013).

[25] D. G. Luenberger, *Optimization by vector space methods,* (John Wiley and Sons, 605 Third Avenue, New York, 1969) Chap. Local theory of constrained optimization, pp. 239–270.

6

Conclusion

In this dissertation we describe possible new ways to determine the side-wall angle of a cliff-like object with optical techniques. We address this problem both theoretically and experimentally. The methods we developed are all relying on the scatterometry principles under a coherent light source illumination. Coherent Fourier Scatterometry (CFS) is the common technique that connects all the chapters, whether it is explicitly use to retrieve the scattering properties of an object - as in Chapter 2 - or when its strong features and understanding apply to new targets, as in Chapters 3, 4 and 5.

In Chapter 2 we introduce the concept of CFS and use it to determine the scattering matrix of a periodic structure, i.e. a grating. More specifically we use a subwavelength grating - with period $p = 500\,nm$ and input wavelength $\lambda = 633\,nm$ - and detect the far field distribution for different input and output polarization states. These field distributions are obtained by modifying the standard CFS configuration with an interferometer, such that we could obtain the phase information content of the scattered field. The experimental far fields are then compared to the simulated ones obtained via the Rigorous Couple Waved Analysis (RCWA) method. It is important to emphasize that, in order to improve the matching between the experiment and simulation, we employ the measured beam profile as input for the rigorous electromagnetic simulations. Our finding proves that, with an interferometric CFS setup, we can retrieve the scattering matrix of any object under study, without being restricted to the periodicity assumption.

In Chapters 3 to 5 we concentrate on an aperiodic structure represented by a cliff-like object. This choice was primarily made to consider physical effects coming only from the side-wall angle (SWA) variation. This assumption helps us greatly in understanding how the scattered far field changes only due to angle differences and hollows us to keep the mathematical derivation of the scattering problem fully analytical if, in addition, we operate in the scalar optics regime. The reader might find these assumptions too stringent but we argue that it is often the case when beginning to study something new; the *bottom-up* approach guarantees a gradual

understanding of the details.

The concept of spiral mode detection is introduced in Chapter 3 as a mean to enhance the SWA measurement. This method relies on the scattered field expansion into spiral modes and, by applying the same technique on the input beam, we can detect which mode has changed the most due to a non-perfect (smaller than $90°$) SWA. We prove that, in the presence of a Gaussian input beam, detecting the scattered 0^{th} order delivers the highest sensitivity to the side-wall angle change. Furthermore, we briefly explore how the sample acts on different input beams and, in each case, we provide the spiral mode expansion to highlight how every single mode is modified. From an experimental point of view, the scattered field can be decomposed into individual modes with the use of a fork hologram; for this reason we also provide the analytical description of the interaction of such an object with a Gaussian beam, which is surely among the most common beam configurations.

In Chapter 4 we tackle the problem with a different approach. Starting from the usual CFS configuration in which a focused coherent beam is incident on a sample and the scattered far field is detected, we modify the detection branch introducing a split detection configuration. In this case, we monitor the signal given by the difference of the left and right halves of the spot versus the scanning direction of the structure under consideration. The signal given by a cliff-like object with a perfect $90°$ SWA can be compared with a sample characterized by a smaller angle, their differential response can give us indications on the SWA value.

The idea of shaping the input beam (as explored in Chapter 3) and the split detector (introduced in Chapter 5) are combined in a theoretical analysis on the optimization of the input beam. Here we employ the Lagrange multiplier rule to find the input field distribution (amplitude and phase) that delivers the highest sensitivity in the side-wall angle detection. More specifically, we maximize the change of the differential signal coming from the difference of the left and right halves of the spot, due to a small change in side-wall angle. Furthermore, we also investigate the possibility of monitoring the change of the full scattered field caused by a small change in SWA. The former method proves to be much more sensitive to small angle changes, with an increased sensitivity of 150% compared to the standard case of a plane wave illumination. The results show that for the type of structure that was chosen, only the amplitude of the incoming field is largely modified, while the phase is simply jumping between 0 and 2π. Despite the initial assumption of scalar optics, this algorithm can also be extended to the vectorial theory. In that case, the solution provided in this chapter can act as initial guess for the input field, to be inserted into a Maxwell solver, with the aim of reducing the computational time and reaching an optimum solution.

6.1. Future work

As it was already highlighted throughout this dissertation, a big improvement can still be achieved in the field of side-wall angle metrology. This thesis aims at being the first step towards a complete understanding on how this geometrical parameter influences the far field distribution of the scattered field, but much is still to be covered. In this section, we discuss possible research topics that could be of great

interest in this field.

6.1.1. Extension of the presented techniques

The techniques presented in this thesis are all applied to a cliff-like structure, but they should be extended to periodic objects as well. The semiconductor industry relies deeply on gratings for target quality assessment, hence any method that aims at being adopted by industrial partners should be able to cope with periodic structures as well. Furthermore, it is necessary to avoid the assumption of scalar optics in favor of the more general vector theory. The reason behind this statement is that, in recent years, the characteristic dimensions of chip components have shrunk considerably, reaching values well below the common wavelength employed in metrology. Hence, scalar optics will not be able to provide the correct physical answer when sub-wavelenght structures are present.

6.1.2. Pupil Engineering in SWA metrology

Semiconductors manufacturers are always optimizing devices to increase their performance and lifetime. This poses several challenges to metrology since hardware tools need to be flexible to adapt seemlessly to the continuous and rapid change of the target under study. Furthermore, metrologists have often very little knowledge about the materials that are part of a microchip, thereby making techniques like reconstruction very difficult to operate. We introduce a very general way to treat the problem, which requires no knowledge of the structure under study. By considering an approach similar to what has been implemented by Mosk and coworkers [1, 2], we aim at calculating the optimum illumination (amplitude and phase) that is most sensitive towards a side-wall angle change of a grating. We solve the light-grating interaction rigorously with the help of a Maxwell solver, which allows us to take different input/output polarization combinations into account.

- We first compute, with RCWA, the scattered field generated by a grating illuminated perpendicularly by a coherent source. We do that for two grating configurations that differ, for example, by 0.1° on the left side-wall angle.
- We subsequently compute the sensitivity coefficient [3] owing to these two different configuration.
- We then modify the phase of a 3×3 group of pixels in the input phase and compute again the sensitivity coefficient.
- The ratio between the newly obtained sensitivity coefficient is then compared to the previous one. If the ratio is bigger than one, we obtain an improved sensitivity and the value of the 3×3 pixels is stored. Otherwise, the current value is discarded in favor of the initial value.

By repeating this operation for all the pixels in the input field, a new phase map, optimized for high sensitivity in the SWA response, is achieved. Despite the apparent simplicity of the procedure, many questions need to be addressed. We list a few:

1. What is the best numerical strategy for choosing the group of pixels that need to be modified?
2. Does the initial choice influence the result?
3. How different initial amplitude distributions and polarization states influence the scattered far field?
4. Can the algorithm be made fast enough to support a real time optimization?
5. What is the dependency of a given solution towards the parameter space?

These are just few of the important questions that such a research topic should address, but surely many more will raise during analysis and investigations.

References

[1] I. Vellekoop and A. Mosk, *Phase control algorithms for focusing light through turbid media,* Optics Communications **281**, 3071 (2008).

[2] I. M. Vellekoop and A. P. Mosk, *Focusing coherent light through opaque strongly scattering media,* Opt. Lett. **32**, 2309 (2007).

[3] O. El Gawhary, N. Kumar, S. F. Pereira, W. M. J. Coene, and H. P. Urbach, *Performance analysis of coherent optical scatterometry,* Applied Physics B **105**, 775 (2011).

Acknowledgements

Here we are, the last - and perhaps most enjoyable to write - section: the acknowledgments! Six years (sigh!) have already passed since I walked through the corridors of the Optics Research Group for the first time. I could never have made it to this point on my own, I was able to succeed only with the support of countless people.

First of all, I would like to thank my promotors Paul H. Urbach and Silvania F. Pereira for allowing me to become a PhD student in the Optics Group. Silvania, thank you for your constant help during these years, your confident attitude has been a great support for me; since I left the group to join ASML, your help to conclude this work has been indispensable, I am profoundly grateful to you for that. My gratitude goes to the committee members as well for reading and evaluating my dissertation.

Among the staff members of the group, I would like to profoundly thank many people: Thim, Roland, Rob, Yvonne, Nandini and Aurèle. Thim, Roland and Rob, I was always amused by how much you know about your respective fields of competence; even better, our discussions never failed to end with a good laugh. Roland, I still remember when, few days before your fly to Italy for a weekend in Monza, you asked me how to translate in Italian "Hema Braadworst"! Rob, hopefully we will soon see Valentino getting his tenth MotoGP title, although chances are getting less and less. Thim, you even came to my housewarming party! Without your support, the experimental work I performed during these years would have never been possible. Yvonne, thank you very much for being always supportive and helpful with any bureaucratic issue and for doing that promptly. Nandini and Aurèle, I did not have the chance to collaborate with you, but your passion for physics, and optics in particular, has helped me a lot in the four years I spent in the group. I enjoyed very much discussing with you about many different topics, from the scientific ones during the Journal Club meetings, to the mundane ones during lunch or coffee breaks. Another important member of the group is surely Prof. Joseph Braat. A regular member of the Journal Club, who fought with honor to win the prize reserved to the person attending most meetings (luckily I had a few more presences). In all seriousness, I am grateful I had the opportunity to meet you and I am really looking forward to getting a copy of your book. Lastly, I would like to thank Omar for his support. Talking to you is truly inspiring and a boost to my passion for physics and optics. Even though, when I joined, you were not formally part of the group, you never refused to help me clear my doubts.

To my fellow PhD's: I am truly happy I met so many different people in these years, thank you all for your help! I believe the group can be metaphorically compared to an harbor. Many people come and go, but they all leave something behind to enrich, and partly affect, the life of others. Thanking you all is not easy, as the

chance to forget someone is considerable given the great number of people who joined (and left) the team; nevertheless, here is my attempt: thank you Daniel, Katsiaryna, Matthias, Alberto, Sarathi, Gopakumar, Nishant, Mahsa, Hamed, Priya, Ying, Zhe, Hugo, Quincy, Yifeng, Fellipe, Wouter, Diego, Anna, Liesbeth, Gyllion, Jelle, Peter, Jeffrey, Nick, Nick, Luiz, George, Maxim. With some of you I have spent more time, with some less. Nevertheless, you all contributed to make this PhD unforgettable: from the SPIE student chapter, to the Lichtjesavond stand - which I hope will become a tradition for the Optics Group - from the PhD lunch seminars to the Journal Club meetings.

Special thanks go to the people who assisted me with the English to Dutch translation of the Summary and Propositions: Sander, Marco and Peter. Peter you never hesitate a second when someone asks for help and that is surely an admirable quality. Marco, we haven't have the chance to spend much time together but I was lucky enough to get to know you when you were a master student, I am sure the group will benefit from your smartness and humor. Sander, we have shared many long days in the lab, together with the good "old sport" Luiz. Do you remember when he was putting the Beach Boys' song "Sloop John B" as a hint to conclude the working day and go home? We really all had a good time together!

A few more words for other fellow PhD's who have played a big role in helping me becoming a *Doctor of Philosophy*. A big hug to Mr. Polo who, besides being a good friend always ready to support me, taught me how to make pizza and, more importantly, have been (twice!) able to recommend me for a job position; finally I was able to return the favor with your recent job shift. Edgar, you were so kind to gift me the football team jersey of Costa Rica and we even manage to have Fika together in Stockholm. You and Yasmín are a wonderful couple, you both definitely can achieve everything you want in life and I admire you for your courage to go after your dreams. Adonis and Tania, thank you for all the fun moments spent together! Thanks to you I made my first moves in a salsa party (with the same flexibility of a mannequin) and I have tasted grasshoppers, which were unexpectedly delicious. I am happy that, when you spent your summer holidays in Italy, I was able to show you the places where I grew up. Plus, you got to try my mother's cooking. Talking about cooking, the best Indian food I had in Delft was surely not in a restaurant, but at Nitish and Gopika's place! You guys have really been awesome friends over these years, and I hope things will stay this way for many more. Professionally I have learned a lot from both of you, Nitish has even been my daily supervisor for 7 months! I know I can always rely on you - for example when I came to your apartment at 23:30 because I had no keys and my smartphone battery was dead. I am very happy we still managed to live close by even in Eindhoven.

It went perhaps unnoticed but there is still someone that deserves my attention. I am talking about you, Dr. Hänsel. Sharing an apartment with you for three years was with no doubts a game changer for me. We had many many fun moments and only a few arguments. Thanks to you I have tried frozen pizza, karamalz - and few other things I kind of intentionally removed from memory - along with the indie music world and martial arts like Haikido, Ju Jitsu, Karate and Thai boxing. I surely would not have tried them without you. I truly believe you are among the

smartest people I have ever met and I wish you the best for your scientific career. I am convinced that, with your way of arguing and with your beliefs, you made me a far better person that I was when I left home, words are probably not enough to express my gratitude.

Outside the University I spent most of my time in a Futsal field. Playing for Tutor has been a mix of emotions, we lost many games but we also almost got promoted! I will never forget the Monday trainings from 22 to 24h, we were the only team starting a training session on Monday and ending it on Tuesday! After playing with you for three years, I know what true Futsal is. Coach Nuno, thank you for your huge patience with this Italian guy that was often complaining and swearing; I wish more people have your commitment to improve and get better everyday, I will surely bring your example with me. All the best to Sabrina for her career and to the little Laura. Radu, Djordy, Jibbe, Sam, Andre, José, Soufian, Sander (from the fire), Sander, Steven, Erik, Danny: I am honored I got to play with you, you all are good players and more importantly good people, you deserve the best in life and I am sure you will get it. Thanks to you I have learned a lot of the Dutch culture (with you I tried *kroketten* for the first time) and I guess you now all know how to pronounce "vaffanculo" quite well!

For the last part of these acknowledgments, I prefer to switch to Italian. I hope that my Italian friends, my family and my girlfriend will be able to get the main message, given that I cannot support my statements with gestures. *Infine, i ringraziamenti a delle persone davvero speciali. Un grazie a tutti i miei amici che sono volati in Olanda per condividere con me questo momento di gioia. Significa molto per me e sono felice che, nonostante ognuno di noi abbia intrapreso strade diverse, quando ci si ritrova il tempo sembra essersi fermato e si inizia a ridere e scherzare come qualche anno fa; mi auguro davvero che il futuro ci riavvicinerà un pò. Lorenzo e Skylar, la vostra maturità e caparbietà è un motivo di ispirazione, vi auguro davvero una vita piena di soddisfazioni e felicità, ovunque voi sarete. Sono davvero contento di essere entrato a far parte di ciascuna delle vostre famiglie.*
Ai miei genitori e mio fratello, un grazie dal profondo del cuore. So che per nessuno di voi dev'essere stato facile vedermi partire, ma sono grato siate riusciti a farmi fare questo passo. Sono sinceramente una persona migliore di quella che era partita: più matura, tollerante, amante delle diversità e del prossimo. Michele, non è stato semplice nemmeno per me non avere più il mio fratellino accanto, ma sono contento che abbiamo solo che rafforzato il nostro rapporto negli anni. Auguro anche a te di fare un'esperienza simile alla mia, penso sia una cosa che insegni molto! Mamma e papà, che dire, ammiro incredibilmente il vostro coraggio! Siete riusciti a mettere il mio bene prima dei vostri sentimenti, a mio parere non è una cosa così scontata. Vi sarò eternamente grato per questo.

Manchi solo tu, Ilaria. Grazie infinite per tutto. Mi hai sempre sostenuto, incoraggiato e spronato ad arrivare a questo traguardo. Delle volte hai creduto più te in me di quanto io stesso facessi, grazie! I quattro anni di questo PhD non sono stati semplici, le relazioni a distanza sono difficili, ma ci hanno rafforzato molto. Con quello che abbiamo passato, sono sicuro che abbiamo la forza e le motivazioni per raggiungere i nostri sogni, ed ho intenzione di essere sempre al tuo fianco perché

ciò accada. Ricordo ancora quando, in seconda superiore, Alberto mi aveva detto che, secondo lui, io e te avremmo potuto essere una bella coppia, ed eccoci qua! Abbiamo già realizzato uno dei nostri sogni di gioventù, ora sono davvero curioso di vedere cosa ci riserverà il futuro. Una cosa è certa, dovrà vedersela con entrambi!

A

Unwrapping algorithm and smoothing filter

In Chapter 2 we acquired interferometric data to be able to measure both the scattered amplitude and phase of a grating. Particularly, by substituting into Eq. (2.7) five interferometric images, taken at specific shifts, we can retrieve the phase information. The phase obtained in this way will be wrapped around 2π; hence, in order to retrieve the true scattered phase, a good unwrapping algorithm is necessary to get the continuous phase values out of the wrapped ones. In literature, it is possible to find a wide range of numerical techniques to be employed to solve this problem, with emphasis on different characteristics like accuracy, speed or computational effort. We decided to implement a solution developed at the General Research Institute (GERI) at Liverpool John Moores University (LJMU).

Experimental measurements are always affected by noise of any kind. In our case this strongly influences the quality and reliability of the phase unwrapping process. Well-defined and separated fringes will be the ideal situation to work with; therefore, data is often processed with a smoothing filter before the unwrapping algorithm is applied. In this work, we employed a technique known as windowed Fourier transform (WFT). Let us consider an input signal $f(x,y)$ where (x,y) are spatial coordinates, the windowed Fourier transform, and its inverse, are a pair of transforms as:

$$Sf(u,v,\xi,\eta) = \int_{-\infty}^{+\infty}\int_{-\infty}^{+\infty} f(x,y)\, g^{*}_{u,v,\xi,\eta}(x,y)\, dx\, dy, \tag{A.1}$$

$$f(x,y) = \frac{1}{4\pi^2}\int_{-\infty}^{+\infty}\int_{-\infty}^{+\infty}\int_{-\infty}^{+\infty}\int_{-\infty}^{+\infty} Sf(u,v,\xi,\eta)\, g_{u,v,\xi,\eta}(x,y)\, d\xi\, d\eta\, du\, dv, \tag{A.2}$$

where (u,v) are spatial coordinates, (ξ,η) are frequency coordinates, whereas the complex conjugation operator is represented by the symbol $*$. As we can see from Eq. (A.1), the input signal is decomposed onto a WFT basis resulting in a four

dimensional spectrum $Sf(u,v,\xi,\eta)$. Such a basis is formed by windowed Fourier elements of the form:

$$g_{u,v,\xi,\eta}(x,y) = g(x-u, y-v)\ \exp i(\xi x + \eta y), \tag{A.3}$$

where g is a windowed function such as:

$$g(x,y) = \frac{1}{\sqrt{\pi\sigma_x\sigma_y}}\ \exp\left[-\frac{1}{2}\left(\frac{x^2}{\sigma_x^2} + \frac{y^2}{\sigma_y^2}\right)\right]. \tag{A.4}$$

There exits a strong similarity between the actual Fourier transform and the WFT. In the former case, the spectrum has an infinite spatial extension whereas, in the latter case, the spectrum has a limited spatial extension due to the presence of a window function. In our analysis, a Gaussian function acts as a window; in such a configuration, WFT is also known as Gabor transform. The Windowed Fourier Transform is a very efficient technique to reduce the noise of fringe patterns. Specifically, we obtain the WFT spectrum of the signal we want to analyse; subsequently we can set a threshold to eliminate the coefficients of the transform that are characterized by a small amplitude, as they represent noise. By applying the inverse transform we can obtain a smooth image.

As we previously mentioned, the filtering operation is necessary to improve the quality of the unwrapping problem. The algorithm implemented falls in the category of the quality guided path algorithm; more precisely, it is based on sorting by reliability, following a non-continuous path. In this approach, the highest-quality pixels, with the highest reliability, are unwrapped first and the lowest-quality pixels, that have the lowest-reliability values, are unwrapped last to prevent error propagation. Hence, the choice of a good reliability function is a key component of the algorithm. In this case, a second order derivative is implemented. This is performed by considering a pixel (i,j) along with its orthogonal and diagonal neighbors in a 3×3 window:

$$D(i,j) = \sqrt{H^2(i,j) + V^2(i,j) + D_1^2(i,j) + D_2^2(i,j)} \tag{A.5}$$

where:

$$\begin{aligned}
H(i,j) &= \gamma\left[\phi(i-1,j) - \phi(i,j)\right] - \gamma\left[\phi(i,j) - \phi(i+1,j)\right] \\
V(i,j) &= \gamma\left[\phi(i,j-1) - \phi(i,j)\right] - \gamma\left[\phi(i,j) - \phi(i,j+1)\right] \\
D_1(i,j) &= \gamma\left[\phi(i-1,j-1) - \phi(i,j)\right] - \gamma\left[\phi(i,j) - \phi(i+1,j+1)\right] \\
D_2(i,j) &= \gamma\left[\phi(i-1,j+1) - \phi(i,j)\right] - \gamma\left[\phi(i,j) - \phi(i+1,j-1)\right]
\end{aligned} \tag{A.6}$$

where $\gamma(\cdot)$ represents an unwrapping operation to remove any 2π discontinuities between two consecutive pixels and $\phi(i,j)$ represents the phase function at a particular pixel. The value of the second derivative can be calculated for all the pixels in the image except the borders, where it is set to infinity to guarantee that those pixels are unwrapped last. The reliability function is defined as the inverse of the second derivative $D(i,j)$. Hence the lower the second derivative (lower degree of concavity/convexity) the more reliable a pixel is.

An unwrapping path algorithm is defined relative to the reliability of the edges, which can be divided into horizontal and vertical edges. The reliability of a particular edge is calculated by computing the difference between the reliability of adjacent pixels. After that, the edge with the highest reliability value is computed first; the algorithms proceeds then to unwrap all the pixels in a descending order.

To increase computational speed, the algorithm is implemented in C programming language and subsequently called from Matlab using the *mex* (Matlab executable) dynamically linked subroutine functionality.

B

A useful integral derivation

In this appendix we present a method that allows us to analytically compute an integral close to the one in 4.8. In what follows, c is arbitrary. From [1] we have that:

$$\int_0^z \frac{\sin t}{t} dt = \mathrm{Si}(z), \tag{B.1}$$

$$\int_0^z \frac{\cos(t) - 1}{t} dt = \mathrm{Ci}(z) - \gamma - \log|z|, \qquad z \geq 0. \tag{B.2}$$

Hence, for $z \geq 0$ it holds:

$$\int_0^z \frac{\exp(it) - 1}{t} dt = \int_0^z \frac{\cos(t) + i\sin(t) - 1}{t} dt = \mathrm{Ci}(z) - \gamma - \log|z| + i\,\mathrm{Si}(z), \tag{B.3}$$

$$\int_{-z}^0 \frac{\exp(it) - 1}{t} dt = -\int_0^z \frac{\exp(-it) - 1}{t} dt = -\mathrm{Ci}(z) + \gamma + \log|z| + i\,\mathrm{Si}(z). \tag{B.4}$$

Thus, for $c \geq 0$:

$$F_c(\xi) = \int_0^c \frac{\sin(kax/f)}{kax/f}\, e^{-ik\frac{\xi}{f}x}\, dx \tag{B.5}$$

$$= \frac{f}{2kai}\int_0^c \frac{\exp\left[ix\frac{k}{f}(a-\xi)\right] - \exp\left[-ix\frac{k}{f}(a+\xi)\right]}{x}\, dx \tag{B.6}$$

$$= \frac{f}{2kai}\int_0^c \frac{\exp\left[ix\frac{k}{f}(a-\xi)\right] - 1}{x}\, dx - \frac{f}{2kai}\int_0^c \frac{\exp\left[-ix\frac{k}{f}(a+\xi)\right] - 1}{x}\, dx \tag{B.7}$$

$$= \frac{f}{2kai}\int_0^{c\frac{k}{f}(a-\xi)} \frac{e^{is} - 1}{s}\, ds - \frac{f}{2kai}\int_0^{c\frac{k}{f}(a+\xi)} \frac{e^{-is'} - 1}{s'}\, ds' \tag{B.8}$$

$$= \frac{f}{2ka}\left\{ i\,\mathrm{Ci}\left[c\frac{k}{f}(a+\xi)\right] + \mathrm{Si}\left[c\frac{k}{f}(a-\xi)\right] - i\,\mathrm{Ci}\left[c\frac{k}{f}(a-\xi)\right] + \mathrm{Si}\left[c\frac{k}{f}(a+\xi)\right] + i\ln\left|\frac{a-\xi}{a+\xi}\right|\right\}. \tag{B.9}$$

Where $\mathrm{Ci}(x)$ and $\mathrm{Si}(x)$ are the cosine and sine integrals. With a similar procedure, it is possible to derive ($c \geq 0$):

$$G_c(\xi) = \int_{-c}^0 \frac{\sin(kax/f)}{kax/f}\, e^{-ik\frac{\xi}{f}x}\, dx = \int_0^c \frac{\sin(kax/f)}{kax/f}\, e^{ik\frac{\xi}{f}x}\, dx \tag{B.10}$$

$$= F_c(-\xi) = F_c^*(\xi)$$

$$= \frac{f}{2ka}\left\{ i\,\mathrm{Ci}\left[c\frac{k}{f}(a-\xi)\right] + \mathrm{Si}\left[c\frac{k}{f}(a-\xi)\right] - i\,\mathrm{Ci}\left[c\frac{k}{f}(a+\xi)\right] + \mathrm{Si}\left[c\frac{k}{f}(a+\xi)\right] - i\ln\left|\frac{a-\xi}{a+\xi}\right|\right\}. \tag{B.11}$$

where the symbol $*$ indicates the complex conjugate. Since:

$$\lim_{z\to+\infty} \mathrm{Si}(z) = \frac{\pi}{2}, \qquad \lim_{z\to+\infty} \mathrm{Ci}(z) = 0, \tag{B.12}$$

we have:

$$\lim_{z\to-\infty} \mathrm{Si}(z) = -\lim_{z\to+\infty} \mathrm{Si}(z) = -\frac{\pi}{2}, \qquad \lim_{z\to-\infty} \mathrm{Ci}(z) = 0, \tag{B.13}$$

therefore, for $|\xi| < a$, it holds:

$$\lim_{c\to\infty} F_c(\xi) = \frac{f}{2ka}\left(\pi + i\ln\left|\frac{a-\xi}{a+\xi}\right|\right), \tag{B.14}$$

$$\lim_{c\to\infty} G_c(\xi) = \lim_{c\to\infty} F_c^*(\xi) = \frac{f}{2ka}\left(\pi - i\ln\left|\frac{a-\xi}{a+\xi}\right|\right). \tag{B.15}$$

References

[1] M. Abramowitz and I. Stegun, *Handbook of mathematical functions,* (Dover Publications, 1965).

C

Rigorous far field calculation

In this appendix we compute the rigorous electromagnetic interaction of a ridge and a focused spot in order to validate the results generated with the scalar model presented in Chapter 4. In the vectorial simulation the scattered far field has been calculated using an in-house tool based on the Finite Element Method (FEM) [1]. Let us begin by mentioning the core equations of the FEM algorithm.

In the case of time harmonic electromagnetic fields, Maxwell's equations take the form:

$$\nabla \cdot \epsilon\epsilon_0 \mathbf{E} = \rho \tag{C.1}$$

$$\nabla \times \mathbf{E} = i\omega\mu\mu_0 \mathbf{H} \tag{C.2}$$

$$\nabla \cdot \mu\mu_0 \mathbf{H} = 0 \tag{C.3}$$

$$\nabla \times \mathbf{H} = \mathbf{J_S} + \sigma\mathbf{E} - i\omega\epsilon\epsilon_0 \mathbf{E}, \tag{C.4}$$

where ϵ_0 is the electric permittivity of vacuum, ϵ is the permittivity of the medium in which we seek a solution, ρ is the free electric charge density, $\mathbf{J_S}$ is the source current density, μ_0 is the magnetic permeability of vacuum, μ is the magnetic permeability of the medium and finally $\sigma\mathbf{E}$ represents the induced conduction current density, written in terms of the electric conductivity of the medium. By taking the curl of Eqs. (C.2) and (C.4), we can reduce the above equations to the following two:

$$\nabla \times \mu^{-1} (\nabla \times \mathbf{E}) - k_0^2 \epsilon \mathbf{E} = i\omega\mu_0 \mathbf{J_S} \tag{C.5}$$

$$\nabla \times \epsilon^{-1} (\nabla \times \mathbf{H}) - k_0^2 \mu \mathbf{H} = \nabla \times \epsilon^{-1} \mathbf{J}. \tag{C.6}$$

where we define $\mathbf{J} = \mathbf{J_S} + \sigma\mathbf{E}$. At an interface between two media, Eqs. (C.5) and (C.6) are solved subject to two boundary conditions:

1. Continuity of tangential components of the fields.
2. Discontinuity of normal components of the fields

Mathematically, these two boundary conditions can be written as:

$$\hat{n} \cdot (\mathbf{D}_2 - \mathbf{D}_1) = \rho_{\text{surf}} \tag{C.7}$$
$$\hat{n} \cdot (\mathbf{B}_2 - \mathbf{B}_1) = 0 \tag{C.8}$$
$$\hat{n} \times (\mathbf{E}_2 - \mathbf{E}_1) = 0 \tag{C.9}$$
$$\hat{n} \times (\mathbf{H}_2 - \mathbf{H}_1) = \mathbf{J}_{\text{surf}}, \tag{C.10}$$

where $\hat{n}$ is the outward normal at the interface from the two media (labeled as *1* and *2*), ρ_{surf} and $\mathbf{J}_{\text{surf}}$ are the charge and current densities of the surface. Furthermore, we introduce the electric displacement $\mathbf{D}$ and the magnetic induction $\mathbf{B}$, that can be expressed as $\mathbf{D} = \epsilon_0 \epsilon \mathbf{E}$ and $\mathbf{B} = \mu_0 \mu \mathbf{H}$. In a FEM algorithm, we assume an approximate solution of Eqs. (C.5) and (C.6), which obeys the boundary conditions given by Eqs (C.7) - (C.10). The accuracy of this solution is subsequently improved by minimizing the residuals obtained from the fit of the approximate solution.

In Chapter 4 we analytically compute the scattered far field by a ridge-like structure within the scalar regime. The ridge is centered in a (x, y, z) reference system as shown in Fig. C.1, it is invariant with respect to the y-coordinate and it is described by the function $p_{\alpha_L,\alpha_R}(x)$ defined as:

$$z = p_{\alpha_L,\alpha_R}(x) := \begin{cases} 0, & \text{if} \quad x \leqslant -w/2 \\ x \tan\alpha_L + \frac{h}{2}, & \text{if} \quad -w/2 < x < -b_L \\ h, & \text{if} \quad -b_L \leqslant x \leqslant +b_R \\ -x \tan\alpha_R + \frac{h}{2}, & \text{if} \quad +b_R < x < +w/2 \\ 0, & \text{if} \quad x \geqslant +w/2 \end{cases} . \tag{C.11}$$

In the scalar simulation we use the side wall angles α_L, α_R, the height h and the width w as variables to describe the ridge, hence mathematical expressions for b_L and b_R are given by the formulas:

$$b_L = \frac{h}{2\tan\alpha_L}, \quad b_R = \frac{h}{2\tan\alpha_R} \qquad \text{where} \quad 0 < \alpha_L, \alpha_R < \frac{\pi}{2}. \tag{C.12}$$

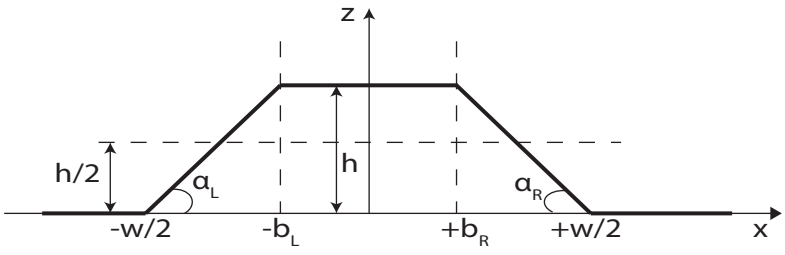

Figure C.1: Sketch of a cliff-like object.

Moreover, we assume that the structure described by the function $p_{\alpha_L,\alpha_R}(x)$ represents a pure phase object, which is characterized by the following reflection

function:

$$r^{R}_{\alpha_L,\alpha_R}(x) = r\begin{cases}\exp(2ikh), & \text{if} \quad x \leqslant -w/2 \\ \exp\{ik\,[2h-(2x+w)\tan\alpha_L]\}, & \text{if} \quad -w/2 < x < -b_L \\ 1, & \text{if} \quad -b_L \leqslant x \leqslant +b_R \\ \exp\{ik\,[2h+(2x-w)\tan\alpha_R]\}, & \text{if} \quad +b_R < x < +w/2 \\ \exp(2ikh), & \text{if} \quad x \geqslant +w/2\end{cases}, \tag{C.13}$$

where $k = 2\pi/\lambda$ is the wave number and r is the reflection coefficient of the surface. This coefficient can be a complex number with $|r| \leq 1$ but we shall subsequently simply take $r = 1$. For the comparison between scalar and vectorial theory we consider a ridge with perfectly straight side-wall angles, meaning that the left and right side wall angles are: $\alpha_L = \alpha_R = 90°$. The height of the ridge is $h = 170\,nm$ and the width is $w = 2\,\mu m$.

The structure interacts with a focused field generated by a cylindrical lens with numerical aperture NA $= 0.6$. With the term cylindrical lens we mean an objective which is independent of the y-coordinate; such a system transforms a plane wave in a field that is focused along the x-direction, but is independent of the y-coordinate. In the vectorial case, the focused field at the focal plane, for the case of TE polarization, can be computed using the following expression [2]:

$$E_y(x) = \int_{-\alpha}^{+\alpha} \cos^{1/2}\theta\, \exp[ikx\sin\theta]\, d\theta \tag{C.14}$$

where $\alpha = \arcsin(\text{NA})$ is the semi-aperture of the lens. The factor $\cos^{1/2}\theta$ is the aplanatic apodization factor for a slit system, where θ is the angle between a ray and the optical axis. A simple sketch of the computational domain used in the vectorial simulation, with the relative reference system, is given in Fig. C.2.

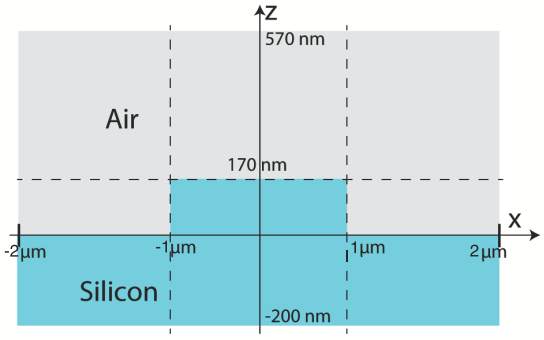

Figure C.2: The computational domain of the rigorous vectorial simulation extends from $-2\,\mu m$ to $+2\,\mu m$ in x and from $-200\,nm$ to $+570\,nm$ in z. The ridge has width $w = 2\,\mu m$ and height $h = 170\,nm$.

It is important to mention that in the rigorous calculations we consider a substrate, with the ridge on top of it, made of silicon (Si). For this material we

use a refractive index (at $\lambda = 632.8\,nm$) $n = 3.8827$ with extinction coefficient $k = 0.019626$ [3]. Furthermore, we note that when considering the TE polarization case, only the E_y component is non-zero; i.e., the depolarization effects normally found in tight focusing are not present in this case. The TM component, however, does present depolarization effects, i.e. a longitudinal component (E_z). Thus in order to compare with the scalar theory, we consider only the TE polarization.

In Fig. C.3 we show the absolute value of the scattered near field for the case of TE polarization, namely along the y-direction. Because the ridge width we considered is bigger than the diameter of the focal spot, the field is mostly reflected by the structure and it is only weakly influenced by the presence of the two abrupt edges. We note that, in the case of TE polarization, the spot generated by a cylindrical lens does not differ significantly from the x-profile of the spot generated by a spherical lens. Thus, in view of some computational problems affecting our in-house software tool regarding the generation and handling of the correct 2D focused spot, which could not be solved before the finalization of this dissertation, we decided to use the x-profile of a 3D focused spot to generate the data of Fig. C.3.

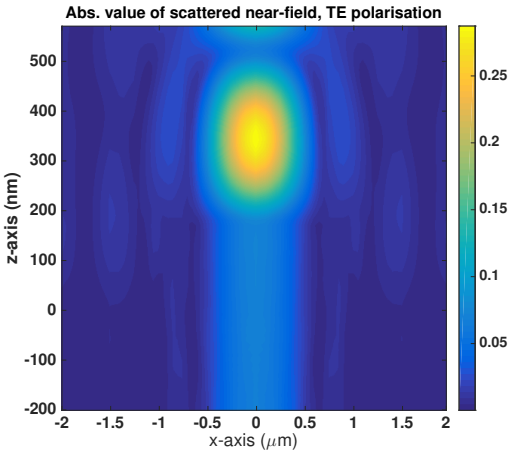

Figure C.3: Absolute value of the scattered near field E_x for TE polarisation, the ridge has width $w = 2\,\mu m$ and height $h = 170\,nm$.

After obtaining the near filed distribution in the TE polarization case, we also calculate the scattered far field by means of a Fourier Transform from the near-field distribution. This is internally calculated with the in-house, FEM-based, tool we introduced at the beginning of this appendix. In Fig. C.4, we plot a comparison of the scattered far field computed using the scalar approximation and the rigorous simulations. As we can see, there is good agreement between these two cases. This implies that, even within the scalar approximation and the description of the ridge as a phase object, the results presented in Chapter 4 are a good model to describe the interaction between the focused and the structure for the case of relatively low numerical aperture.

The results of Fig. C.4 are normalized to the total detected power carried by the

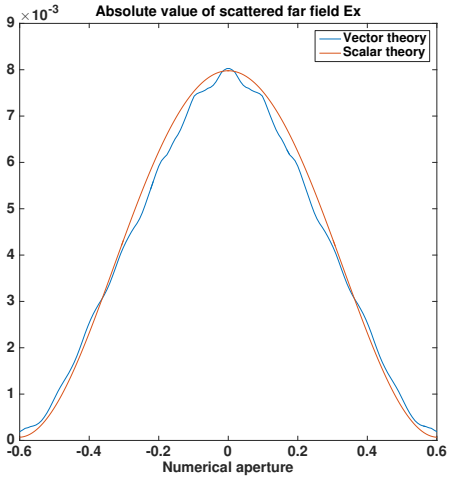

Figure C.4: Scattered far-field comparison between the rigorous and scalar simulations.

far field when there is no structure, i.e. the substrate is flat. For the vectorial case this implies running two simulations, with and without the presence of the ridge. In the latter case, we integrate the scattered far-field within the detection NA such that we obtain a single scalar number we will use as normalisation. In the scalar case, we can write the focused spot generated by a plane wave of unit power as:

$$U^i(x) = \sqrt{\frac{1}{\lambda f}}\, e^{ik2f}\, 2a\, \mathrm{sinc}\left(\frac{2ax}{\lambda f}\right), \tag{C.15}$$

hence, the power carried by the scattered far field when the substrate is flat can be expressed as:

$$I_0(\xi) = \left|\sqrt{\frac{1}{\lambda f}}\, e^{ik2f} \int_{-\infty}^{+\infty} U^i(x)\, e^{-2\pi i \frac{\xi}{\lambda f} x}\, dx\right|^2 = \left|e^{ik4f}\, \mathrm{rect}\left(\frac{\xi}{2a}\right)\right|^2. \tag{C.16}$$

Hence, given that in Chapter 4 we have considered an input field with unitary amplitude and the structure is supposed to act as a phase object, the scattered far-field in the case of a simple reflection from a flat profile is also unitary. The total detected power is the integral within the detection NA of the scattered far-field.

References

[1] X. Wei, A. J. Wachters, and H. P. Urbach, *Finite-element model for three-dimensional optical scattering problems,* J. Opt. Soc. Am. A **24**, 866 (2007).

[2] C. J. R. Sheppard, *Cylindrical lenses—focusing and imaging: a review [invited],* Appl. Opt. **52**, 538 (2013).

[3] D. E. Aspnes and A. A. Studna, *Dielectric functions and optical parameters of si, ge, gap, gaas, gasb, inp, inas, and insb from 1.5 to 6.0 ev,* Phys. Rev. B **27**, 985 (1983).

D

Fourier Transform of the object reflection function

In this appendix, we give more details about the derivation of Eq. (5.66), while Eq. (5.67) is readily obtained simply by differentiation with respect to the SWA α. Given that $r_\alpha(x)$ is a piece-wise defined function (Eq. (5.3)), we can write its Fourier transform as:

$$\begin{aligned}\mathcal{F}(r_\alpha)(\xi) = \exp(2ikh) &\int_{-\infty}^{-\frac{a}{2}} 1\, \exp(-2\pi i\xi x)\, dx \\ &+ \int_{-\frac{a}{2}}^{+\frac{a}{2}} \exp\left[2ik\left(\frac{h}{2} - x\tan(\alpha)\right)\right] \exp(-2\pi i\xi x)\, dx \\ &+ \int_{+\frac{a}{2}}^{+\infty} 1\, \exp(-2\pi i\xi x)\, dx,\end{aligned} \tag{D.1}$$

where the first integral should be interpreted as the Fourier transform of the function that is one in the interval $]-\infty, -a/2[$ and zero otherwise, with a similar interpretation for the third integral. The second integral in the right-hand side of Eq. (D.1) can be easily calculated:

$$\begin{aligned}\exp(ikh) &\int_{-a/2}^{+a/2} \exp[-2i(k\tan(\alpha) + \pi\xi)x]\, dx \\ &= a\, \exp(ikh)\, \operatorname{sinc}\left(a\frac{2}{\lambda}\tan\alpha + a\xi\right),\end{aligned} \tag{D.2}$$

where the sinc function is defined as $\operatorname{sinc}(x) = \sin(\pi x)/(\pi x)$. To be able to solve the first and the third integrals, we use distribution theory. Let us rewrite the third

integral as:

$$\int_{-\infty}^{+\infty} 1_{[+a/2,+\infty]}(x)\, \exp(-2\pi i\xi x)\, dx = \mathcal{F}\left(1_{[+a/2,+\infty]}\right)(\xi). \tag{D.3}$$

We have:

$$\begin{aligned}\mathcal{F}(1_{[+a/2,+\infty]}(x))(\xi) &= \mathcal{F}\left[1_{[0,+\infty]}\left(x-\frac{a}{2}\right)\right](\xi) \\ &= \exp(-\pi i\xi a)\, \mathcal{F}(1_{[0,+\infty]}(x))(\xi).\end{aligned} \tag{D.4}$$

Since :

$$\mathcal{F}\left(\frac{d}{dx}\, 1_{[0,+\infty]}\right)(\xi) = \mathcal{F}(\delta) = 1, \tag{D.5}$$

we have:

$$\mathcal{F}(1_{[0,+\infty]})(\xi) = \frac{1}{2\pi i\xi} + b\,\delta(\xi), \tag{D.6}$$

where b is a constant that still needs to be determined and where the first term is to be interpreted as a distribution defined in the sense of the Cauchy Principal Value. To determine b we use the following relations:

$$\mathcal{F}(1_{[-\infty,0]})(\xi) + \mathcal{F}(1_{[0,+\infty]})(\xi) = \delta(\xi), \tag{D.7}$$

$$\mathcal{F}(1_{[-\infty,0]})(\xi) + \mathcal{F}(1_{[-\infty,0]})(\xi)^* = 2\,\delta(\xi)\Re(b), \tag{D.8}$$

$$\mathcal{F}(1_{[-\infty,0]})(\xi)^* = \mathcal{F}(1_{[0,+\infty]})(\xi), \tag{D.9}$$

hence $b = 1/2$, which gives us:

$$\mathcal{F}(1_{[a/2,+\infty]})(\xi) = \exp(-\pi i\xi a)\left[\frac{1}{2\pi i\xi} + \frac{\delta(\xi)}{2}\right]. \tag{D.10}$$

Everything derived so far applies to the first integral of Eq. (D.1) as well, with the proper change of sign. Hence we have:

$$\mathcal{F}(1_{[-\infty,-a/2]})(\xi) = \exp(2ikh + \pi i\xi a)\left(\frac{i}{2\pi\xi} + \frac{\delta(\xi)}{2}\right). \tag{D.11}$$

Finally, the Fourier transform of the reflection function r_α, is given by:

$$\begin{aligned}\mathcal{F}(r_\alpha)(\xi) = \exp(ikh)\Bigg[&-\frac{\sin(kh + a\pi\xi)}{\pi}\mathrm{PV}\left(\frac{1}{\xi}\right) \\ &+ \delta(\xi)\cos(kh) + a\,\mathrm{sinc}\,(kh + a\xi\pi)\Bigg],\end{aligned} \tag{D.12}$$

in the last equation, the α dependence is hidden inside the variable a. To make the dependence on α more explicit we use Eq. (5.2) to rewrite (D.12) as:

$$\mathcal{F}(r_\alpha)(\xi) = \exp(ikh)\left[-\frac{\sin\left(kh + \pi h\frac{\xi}{\tan\alpha}\right)}{\pi}\mathrm{PV}\left(\frac{1}{\xi}\right)\right. \\ \left. + \delta(\xi)\cos(kh) + \frac{\sin\left(kh + \pi h\frac{\xi}{\tan\alpha}\right)}{k\tan\alpha + \pi\xi}\right]. \tag{D.13}$$

Taking the derivative with respect to α of Eq. (D.13) will lead us to expression we used in Eq. (5.67).

Curriculum Vitæ

Luca Cisotto

19-03-1988 Born in Rovigo, Italy.

Education

2007–2010 B.Sc. in Physics
University of Padova, Padova, Italy.

2010–2012 M.Sc. in Physics
University of Padova, Padova, Italy

2012–2018 PhD. Student in Applied Science
Optics Research Group, Dept. Imaging Physics,
Delft University of Technology, Delft, The Netherlands.
Thesis: Optimisation of Coherent Fourier Scatterometry for Side Wall Angle Estimation of Printed Structures
Promotor: Prof. Dr. H. P. Urbach and Dr. S. F. Pereira

2016– Design Engineer, ASML, Eindhoven, The Netherlands.

Awards

2012 Graduated with Honors: University of Padova.

List of Publications

Published:

5. **L. Cisotto, S. F. Pereira and H. P. Urbach**, *Analytical calculation on the determination of steep side wall angles from far field measurements*, Journal of Optics **20**, 065601 (2018).

4. **L. Cisotto and H. P. Urbach**, *Amplitude and phase beam shaping for highest sensitivity in sidewall angle detection*, Journal of Optical Society of America A **34**, 52 (2017).

3. **N. Kumar, L. Cisotto, S. Roy, G. Ramanandan, S. F. Pereira and H. P. Urbach**, *Determination of the full scattering matrix using coherent Fourier scatterometry*, Applied Optics **16**, 4408 (2016).

2. **L. Cisotto, Y. Zhu, S. F. Pereira and H. P. Urbach**, *Spatial mode projection for side-wall angle measurements*, Proc. SPIE **9526**, 952607 (2015).

1. **A. P. Konijnenberg, L. Wei, N. Kumar, L. Couto Correa Pinto Filho, L. Cisotto, S. F. Pereira and H. P. Urbach**, *Demnstration of an optimised focal field with long focal depth and high transmission obtained with the Extended Nijboer-Zernike theory*, Optics Express **22**, 311 (2014).

Conference contributions:

6. **Xiujie Dou, L. Cisotto, S. F. Pereira and H. P. Urbach**, *Study of determination of steep side wall angles determination based on far field measurements*, European Optical Society Biennial Meeting 2018. 08-12 October 2018, Delft, The Netherlands.

5. **L. Cisotto , S. F. Pereira and H. P. Urbach**, *Determination of steep side wall angles based on far field measurements*, Conference on Micro and Nano Engineering (MNE). 18-22 September 2017, Braga, Portugal.

4. **L. Cisotto, O. El Gawhary and H. P. Urbach**, *Phase Beam shaping for enhanced side-wall angle sensitivity*, European Optical Society Annual Meeting 2016. 26-30 September 2016, Berlin, Germany.

3. **L. Cisotto, Y. Zhu, S. F. Pereira and H. P. Urbach**, *Spatial mode projection for side-wall angle measurements*, International Summer School on Metrology 2015. 24-28 August 2015, Drübeck, Germany.

2. **N. Kumar, P. Petrik, L. Cisotto, S. Roy, S. F. Pereira and H. P. Urbach**, *Solving inverse problems in scatterometry for grating reconstruction in semiconductor industry*, European Optical Society Annual Meeting 2014. 26-30 September 2014, Berlin, Germany.

1. **J. Meisner and L. Cisotto**, *Two-wavelength method for measurement of relative optical phase shifts*, European Optical Society Annual Meeting 2014. 15-19 September 2014, Berlin, Germany.